On the hydrodynamics in gas phase polymerization reactors

On the hydrodynamics in gas phase polymerization reactors

Samenstelling promotiecommissie:

prof.dr. P.J. Lemstra, voorzitter	Technische Universiteit Eindhoven
prof.dr.ir. J.A.M. Kuipers, promotor	Technische Universiteit Eindhoven
prof.dr.ir. M. van Sint Annaland, promotor	Technische Universiteit Eindhoven
prof.dr. J.P.K. Seville	University of Warwick
Prof.Dr.-Ing.habil. S. Heinrich	Hamburg University of Technology
prof.dr. J.G.M. Kuerten	Technische Universiteit Eindhoven
prof.dr.ir. J.C. Schouten	Technische Universiteit Eindhoven
dr.ir. G.B. Meier	LyondellBasell

Publisher: *Ipskamp Drukkers B.V.,* P.O. box 333, 7500 AH, Enschede, the Netherlands

On the hydrodynamics in gas phase polymerization reactors / by Jan Albert Laverman. - Eindhoven: Eindhoven University of Technology, 2010. - Proefschrift.

A catalogue record is available from the Eindhoven University of Technology Library

ISBN: 978-90-386-2408-2

ON THE HYDRODYNAMICS IN GAS PHASE POLYMERIZATION REACTORS

PROEFSCHRIFT

ter verkrijging van de graad van doctor aan de
Technische Universiteit Eindhoven, op gezag van de
rector magnificus, prof.dr.ir. C.J. van Duijn, voor een
commissie aangewezen door het College voor
Promoties in het openbaar te verdedigen
op maandag 20 december 2010 om 14.00 uur

door

Jan Albert Laverman

geboren te Menaldumadeel

Dit proefschrift is goedgekeurd door de promotoren:

prof.dr.ir. J.A.M. Kuipers
en
prof.dr.ir. M. van Sint Annaland

The work described in this thesis was part of the research program of the Dutch Polymer Institute (DPI)

Aan Anouk en mijn ouders

Summary - On the hydrodynamics in gas phase polymerization reactors

Polyolefins are polymers produced from olefins such as ethylene and/or propylene. Although polyolefins can be produced via different production methods, the gas-phase polymerization process based on fluidized bed reactor technology is the most important method for the production of polyethylene since the 1980's and also polypropylene is increasingly produced via the gas-phase polymerization process. Although fluidized bed reactors have been employed for several decades in the chemical industry, quantitative information on solids motion and macroscopic circulation patterns is still incomplete.

To investigate the macroscopic circulation patterns in a freely bubbling, gas-solid fluidized bed, first the hydrodynamics in two pseudo-2D columns of different width filled with glass beads and Linear Low Density Polyethylene (LLDPE) particles have been investigated (both exhibiting Geldart B type behavior) experimentally with two optical non-invasive measuring techniques. Particle Image Velocimetry (PIV) combined with Digital Image Analysis (DIA) has been developed to determine simultaneously the emulsion phase circulation patterns, bubble hold-up, bubble size and velocity distributions and visual bubble flow rate profiles. The combination of DIA with PIV allows correcting for the influence of particle raining through the roof of the bubbles on the time-averaged emulsion phase velocity profiles. The number-averaged emulsion phase

circulation patterns have been measured as a function of fluidization velocity, bed aspect ratio, bed width and bed material. Moreover, with DIA the average bubble diameter and averaged bubble velocity as a function of height and fluidization velocity have been determined and found to correspond reasonably well with literature correlations. However, the difference in averaged bubble diameter as a function of the height in the fluidized bed for the two different particle types could not be explained by the currently available correlations for the bubble diameter. The difference in observed bubble properties is attributed to differences in the particle collisional properties (coefficients of restitution and the particle friction coefficient).

To verify this hypothesis, the influence of microscopic particle properties on the hydrodynamics in a bubbling fluidized bed have been investigated in detail using the Discrete Particle Model (DPM) and the Two-Fluid Model (TFM). It was concluded that, for the conditions investigated, indeed bubbles are formed due to collisional dissipation of mechanical energy. Furthermore, the nature (i.e. due to restitution or friction) of the energy dissipation is important for the shape of the bubbles. In addition it is shown that in a bubbling fluidized bed, the energy is mainly dissipated by friction between particles and particles and the wall. The influence of the normal restitution coefficient on the macroscopic circulation pattern was also investigated with the Two-Fluid Model. The observed influence of the coefficient of restitution in the normal direction agreed with the influence of the coefficient of restitution in the normal direction in the DPM. Also the experimental results obtained with the PIV combined with DIA measurements for the solids phase and DIA measurements for the bubble behavior were compared with simulations performed with the DPM and the TFM. It was shown that the trends for the emulsion phase and the bubble phase can be predicted with the DPM.

The solids and bubble behavior in a freely bubbling, three dimensional, gas-solid fluidized bed has been experimentally investigated using different bed materials, different bed aspect ratios at different superficial gas velocities by performing Positron Emission Particle Tracking

(PEPT) experiments. The fluidized bed was filled with either glass beads or with linear low density polyethylene (LLDPE). At lower superficial gas velocities two distinct vortices appear above each other for both types of bed material; when the superficial gas velocity is increased, the lower vortex disappears and the top vortex spans the entire length of the bed. Although qualitatively the same phenomena were observed, the time-averaged solids phase circulation rate in the fluidized bed filled with LLDPE particles was higher than the time-averaged solids phase velocity in the fluidized bed filled with glass beads. When the bed aspect ratio is increased from 1 to 1.5, the vortices become elongated without altering the solids circulation rate. Differences in the particle-particle collisional properties (coefficients of restitution and friction particle coefficients) are believed to be the cause of the observed quantitative differences in the bed hydrodynamics via their influence on the bubble properties.

Finally, the hydrodynamic behavior of industrial scale bubbling fluidized bed reactors, a 3D Discrete Bubble Model (DBM) has been used. In the DBM, an Euler-Lagrange model, the bubbles are treated as discrete elements and the bubble trajectories are tracked individually, while the emulsion phase is considered as a continuum and is described with the continuity and Navier-Stokes equations. The main advantage of the DBM is that it fully accounts for the two-way coupling, allowing computation of the prevailing macroscopic circulation patterns in large scale gas-fluidized beds. We have examined the effects of bubble-bubble interactions on the macro-scale velocity profiles using the DBM. It has been found that the extent of the macroscopic circulation is significantly increased by the bubble-bubble interaction forces.

Samenvatting - Over de hydrodynamica in gasfase polymerisatie reactoren

Polyolefinen zijn polymeren die worden geproduceerd met olefinen zoals ethyleen en propyleen als grondstof. Hoewel polyolefinen via verschillende productieprocessen kunnen worden vervaardigd, heeft sinds de jaren 80 het gasfase polymerisatie proces, die gebaseerd is op gas-vast wervelbed reactor technologie, het grootste marktaandeel voor de productie van polyethyleen. Eveneens wordt polypropyleen steeds vaker met wervelbed technologie geproduceerd. Alhoewel wervelbedden al meerdere decennia in de chemische industrie worden toegepast, is kwantitatieve informatie over het deeltjes gedrag in de gas-vast suspensie in deze reactoren nog steeds schaars.

Om de macroscopische circulatiepatronen in een gas-vast wervelbed nader te onderzoeken, is eerst de hydrodynamica in twee verschillende pseudo twee-dimensionale kolommen, gevuld met glas deeltjes of met lineaire lage dichtheid polyethyleen (LLDPE) deeltjes (beide deeltjes typen vertoonden Geldart B type gedrag), experimenteel onderzocht met twee optische niet-invasieve meettechnieken. Particle Image Velocimetry (PIV) gecombineerd met Digital Image Analysis (DIA) is ontwikkeld en gebruikt om simultaan de stromingsprofielen van de deeltjesfase en de belfractie, belgrootte, belsnelheidsverdeling en het visuele bellen debiet in het gas-vast wervelbed te bepalen als functie van de operatie condities en deeltjestype. De combinatie van PIV en DIA maakt het mogelijk om

de gemiddelde deeltjessnelheden te corrigeren voor de deeltjes die door het “dak” van de bellen naar beneden “regent”. De aantal gemiddelde deeltjessnelheidsprofielen zijn gemeten als functie van de superficiële gassnelheid, bed aspect ratio, bedbreedte en bedmateriaal. Eveneens is de gemiddelde belsnelheid en beldiameter bepaald met behulp van DIA, en is aangetoond dat de gevonden experimentele resultaten redelijk goed overeen komen met correlaties uit de literatuur. Het verschil in de gemiddelde beldiameter als functie van de hoogte voor de twee verschillende deeltjestypen kan niet worden verklaard met de correlaties die in de literatuur beschikbaar zijn. Het verschil in de geobserveerde beleigenschappen wordt toegeschreven aan verschillen in botseigenschappen van de deeltjes die het bed vullen (restitutiecoëfficiënten en de deeltjeswrijvingscoëfficiënt).

Om deze hypothese the verifiëren, is de invloed van de microscopische deeltjeseigenschappen op de hydrodynamica in een gas-vast wervelbed in detail onderzocht met behulp van het Discrete Particle Model (DPM) en het Two-Fluid Model (TFM). Uit simulatie resultaten met het DPM is geconcludeerd dat, voor de onderzochte omstandigheden, de bellen inderdaad worden gevormd door mechanische energie-dissipatie van de deeltjes tijdens botsingen met andere deeltjes of met de wand van de reactor. Daarnaast is de manier waarop de deeltjes hun energie verliezen belangrijk voor de vorm van de bellen (m.a.w. door botsing of wrijving met andere deeltjes of met de wand). Eveneens is aangetoond dat in een gas-vast wervelbed de energiedissipatie voornamelijk door wrijving tussen deeltjes en tussen deeltjes en de wand optreedt. De invloed van de restitutiecoëfficiënt in de normale richting is eveneens onderzocht met behulp van het TFM. De waargenomen invloed van de restitutiecoëfficiënt in de normale richting op de hydrodynamica komt overeen met de invloed van de restitutiecoëfficiënt in de normale richting die is waargenomen met het DPM. Tevens zijn de experimentele resultaten verkregen met PIV en DIA, vergeleken met de resultaten verkregen uit de DPM en TFM simulaties. Hieruit blijkt dat de trends voor de deeltjesfase en voor de bellenfase goed kan worden beschreven met het DPM.

Het deeltjes- en bellengedrag in een drie-dimensionale gas-vast wervelbed gevuld met verschillend bed materiaal (glas en LLDPE deeltjes), bij verschillende bedhoogtes en gassnelheden onderzocht met behulp van Positron Emission Particle Tracking experimenten. Bij lage superficiële gassnelheden ontstaan er voor de beide bed materialen twee duidelijke wervelingen boven elkaar. Wanneer de superficiële gassnelheid wordt verhoogd, verdwijnt de onderste werveling en reikt de bovenste over het gehele wervelbed. Hoewel kwalitatief dezelfde fenomenen zichtbaar zijn, zijn de tijdsgemiddelde deeltjesfase circulatiesnelheden voor het bed gevuld met LLDPE deeltjes hoger dan de tijdsgemiddelde deeltjesfase circulatiesnelheden voor het met glasdeeltjes gevulde wervelbed. Wanneer de bed aspect ratio wordt verhoogd van 1 naar 1.5, worden de wervelingen langwerpiger zonder dat de deeltjes circulatie snelheid verandert. Het verschil in de geobserveerde deeltjesfase hydrodynamica kan worden verklaard door de verschillen in botseigenschappen van de deeltjes in het bed (restitutiecoëfficiënten en de deeltjeswrijvingscoëfficiënt).

Tenslotte is de hydrodynamica van een industriële schaal wervelbed onderzocht met behulp van een drie-dimensionale Discrete Bubble Model (DBM). In het DBM, een Euler-Lagrange model, worden de bellen behandeld als discrete elementen en worden de beltrajecten voor elke bel individueel berekend, terwijl de deeltjesfase als continuüm wordt beschouwd, dat wordt beschreven met behulp van de continuïteits- en Navier-Stokes vergelijkingen. Het grote voordeel van het DBM is dat het volledig de zeer belangrijke twee-weg koppeling tussen de bellen- en de deeltjesfase meeneemt, wat noodzakelijk is om de macroscopische deeltjescirculatiepatronen in grote schaal gas-vast wervelbedden te kunnen berekenen. Met het DBM zijn de effecten van bel-bel interacties op de macroschaal snelheidsprofielen onderzocht. Vastgesteld is dat de macroscopische deeltjescirculatie significant wordt vergroot wanneer rekening wordt gehouden met bel-bel interactie krachten.

Contents

CHAPTER 1

General Introduction

Abstract

In this chapter a brief introduction to polyolefins and the production of polyolefins is given. Although the polyolefins are produced in fluidized beds since the 1960's, the behavior of the gas and particle phase in these gas-phase polymerization reactors is not yet fully understood. To study the gas-phase polymerization reactors, a multi-scale approach has been adopted. A brief overview of the production of polyolefins, the macroscopic circulation patterns in a industrial scale fluidized bed, microscopic particle properties and the multi-scale approach are presented, followed by the research objectives and the project goal. Finally the outline of the thesis is given.

1.1 Polyolefins

Polyolefins are polymers which are produced from olefins such as ethylene or propylene. The annual world wide production of polyolefin resins in 2005 was approximately 100 million metric tons (Kissin (2005)). This corresponds to more than 50% of the total plastic production. Polyethylene accounts for 60-65% of the total polyolefin production and polypropyle accounts for approximately 35%. Polyolefins can be produced via different production methods, however the gas-phase polymerization process is the most important method for the production of polyethylene since the 1980's and also polypropylene is increasingly produced via the gas-phase polymerization process (Burdett (2001)).

Burdett (2001) stated that the success of the gas-phase polymerization reactor derives from the advantages of the fluidized bed reactor and the specific requirements of the polymerization catalyst. Due to the good mass transfer in fluidized beds, the highly active catalyst can be optimally used. In addition the process is relatively simple and no solvents are used, which need to be removed later in the process, only dissolved vapors need to be removed.

The gas-phase polymerization was developed by Union Carbide in the 1960's to produce High Density Polyethylene (HDPE), the so-called UNIPOL^{TM} process. The UNIPOL^{TM} process was later on also used to produce other types of polyolefins. The shape of the reactor in the UNIPOL^{TM} process is cylindrical, where the top section is expanded. The reason that the top of the reactor is expanded is to recover elutrated particles in the dense zone of the reactor. The catalyst particles (Ziegler--Natta or metallocene catalyst) are introduced through the side wall of the reactor. The location of the catalysator feed is important, because if the catalyst are introduced at the wrong position it will lead to excessive losses of catalyst. To select the optimal position for the injection of the catalytical particles it is essential to know the extent of particle mixing e.g. the macroscopic circulation patterns inside the fluidized bed reactor. The monomer gas is fed through a distributor which is located at the bottom of the fluidized bed.

This process uses a highly active and selective catalyst (50-100 kg

per gram of catalyst), resulting in strong local production of heat, which needs to be removed from the reaction zone in the fluidized bed reactor. The temperature of the reactor is not allowed to exceed the melting temperature of the polymer, because the polymer particles will start to melt and stick together. The single pass conversion of the monomer gas is therefore restricted to only 5%. The unconverted monomer gas is collected at the top of the reactor, cooled, compressed and recycled to the bottom of the reactor. Despite the excellent heat transfer inside a fluidized bed, the heat removal rate is the limiting factor in the production process. In industry two different methods are used to remove the heat from reactor. The first method involves injection of the monomer as a liquid, where part of the heat of the reaction is removed by evaporating the monomer. The second method with which heat is removed from the reactor is via convective heat transfer through the emulsion phase. The convective heat transfer is mainly governed by the macroscopic circulation patterns of the emulsion phase induced by the rising gas bubbles. However, quantitative information on solids motion and the macroscopic circulation patterns is still incomplete.

1.2 Macroscopic circulation patterns

Baeyens and Geldart (1986) presented a comprehensive literature review of particle mixing in fluidized beds and indicated the wake transport and particle drift, both due to the rising bubbles, as important mechanisms for upward particle motion. Particles in the emulsion phase move downwards in areas where no bubbles are present. Therefore it is important to know the behavior of both phases to describe the hydrodynamics in the fluidized bed. In addition, Baeyens and Geldart (1986) indicated the importance of bubble through flow for gas-particle systems with a high Archimedes number.

Kunii and Levenspiel (1991) stated that at low superficial gas velocity and an aspect ratio (bed height divided by bed diameter) less than 1, the particles move upward near the wall and downward in the center of the fluidized bed. When the aspect ratio is higher, the particles move downward near the wall of the fluidized bed. This is caused by a second

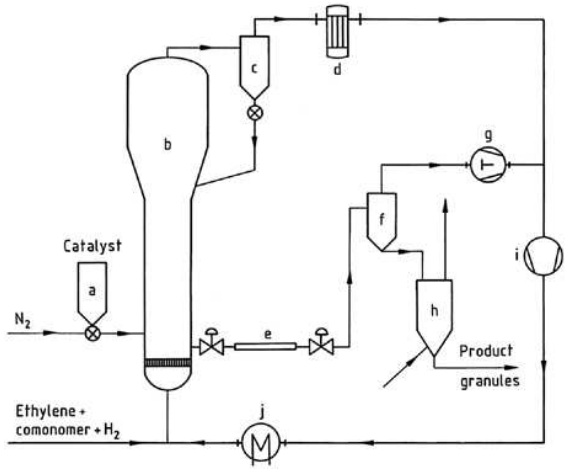

Figure 1.1: *UNIPOL*^{TM} process, (a) Catalyst hopper and feed valve; (b) Fluidized-bed reactor; (c) Cyclone; (d) Filter; (e) Polymer take-off system; (f) Product recovery cyclone; (g) Monomer recovery compressor; (h) Purge hopper; (i) Recycle compressor; (j) Recycle gas cooler, after Whiteley et al. (2000).

vortex which appears above the initial vortex. At higher superficial gas velocity the upper vortex starts to dominate the overall solids movement, the downward movement of the particles at the wall starts closer to the distributor.

It is known that the microscopic particle properties have a large influence on the fluidization behavior. Geldart (1973) showed that the type of gas-fluidization depends on the size and density of the particles. Furthermore it is known that the shape of the particles influences the fluidization behavior and additionally that the collisional properties of the particulate phase influence the bed hydrodynamic. All these particle properties will be discussed in the next paragraph.

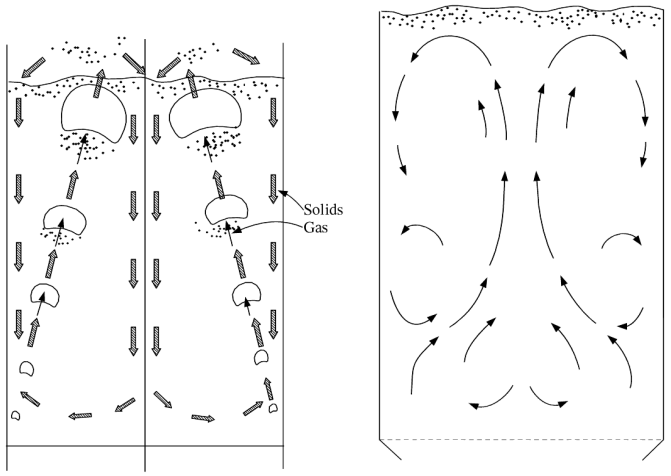

(a) (b)

Figure 1.2: (a) Bubble and particle movement through a fluidized bed at low superficial gas velocity and bed aspect ratio ≈ 1; (b) General emulsion phase movement in deep fluidized beds, both taken from Kunii and Levenspiel (1991).

1.3 Microscopic particle properties

Diameter and density

In 1973, Geldart published the article *'Types of gas fluidization'* in which he identified four different groups of particles with distinctively different fluidization characteristic, namely Geldart A, B, C and D. These four groups could be characterized by the density difference between the particle phase and the gas phase and the mean particle size. The experimental results on which Geldart based his conclusions were mainly conducted at ambient temperature and pressure. However, the Geldart classification has been very useful to the fluidization community. However, many industrial fluidized beds are operated at elevated pressure, for example, the particles inside a gas phase polymerization re-

actor, belong at ambient conditions to the Geldart B group, however there exist strong indications that the fluidization behavior at elevated pressure shift from Geldart B type to Geldart A type particles (Burdett (2001)). Therefore, the classification of Geldart has been extended by researchers to include the effect of pressure, see for example Yang (2007). Yang gives an overview of several modifications of the Geldart classification and in addition also proposed a new classification which takes the pressure into account. Instead of using the density difference between the particle and the gas phase, Yang divides the density difference of the particle and the gas phase by the density of the gas phase, and instead of using the mean particle size he uses the Archimedes number. With this approach Geldart B type fluidization at ambient conditions shifts to Geldart A type fluidization at elevated pressure. However more experimental data is required to determine the precise A/B transition.

Sphericity

The diameter of particles can be determined accurately when the particles are completely spherical. It becomes more difficult to characterize particles by size when they are not spherical. Therefore Kunii and Levenspiel (1991) adopted an effective diameter d_{eff}. The effective diameter is a function of the equivalent spherical particle diameter and the sphericity ϕ_s. The spherical particle diameter and the sphericity are given by:

$$d_{sph} = \sqrt[3]{\frac{V_p}{\frac{1}{6}\pi}} \tag{1.1}$$

and

$$\phi_s = \frac{\text{surface of sphere}}{\text{surface of particle}} \tag{1.2}$$

In addition Kunii and Levenspiel (1991) also give some guidelines to correlate the effective diameter as a function of the sphericity and the particle diameter. However, they advise the reader to measure the effective diameter by measuring the pressure drop over a fixed bed and to fit the effective diameter with the frictional pressure drop equation suggested by Ergun. In addition the void fraction of a packed bed is also

influenced by the sphericity of the particles, and therefore influences the minimum fluidization velocity of the fluidized bed. Liu et al. (2008) investigated the influence of the sphericity on the minimum fluidization velocity and they found that when the particles have the same volume-equivalent diameter, the non-spherical particles typically have a lower minimum fluidization velocity.

Collisional properties of the particle

The coefficient of restitution is an important micro-mechanical parameter which quantifies the loss of mechanical energy due to particle impact. Several authors have investigated the influence of the coefficient of restitution on the fluidization behavior. Goldschmidt et al. (2001) reported that when the collisions become less ideal (e.g. a lower coefficient of restitution) the particles are closer packed in the dense regions of the fluidized beds, and the bubbles are larger.

Goldschmidt et al. (2001) also observed an increase in pressure fluctuations when the coefficient of restitution decreased, which was caused by more vigorous bubbling in the fluidized bed. They state that the coefficient of restitution is one of the key parameters to governing gas bubbles behavior in dense beds.

Taghipour et al. (2005) found that when the coefficient of restitution was increased from 0.9 to 0.99, the bed expansion increased with a factor of 1.35 to 1.45.

Lu et al. (2005) used a two dimensional discrete element model where the collisions were described using the hard-sphere approach. Lu et al. found that when the coefficient of restitution was set to 1, no bubbles appeared in there simulations, however when the coefficient of restitution was decreased to 0.9, bubbles started to grow at the orifice and they slowly increased in size throughout the bed. They concluded that the motion of the particles and the bubbles in the fluidized bed were related to the momentum transfer and energy dissipation due to collisions. These findings are in complete agreement with the earlier findings of Hoomans et al. (1996) who also used a discrete particle model with the hard-sphere model.

Finally, Lindborg et al. (2007) investigated different types of powder using the Euler-Euler approach and reported that the coefficient of restitution is a critical parameter to describe the experiments conducted with Geldart B correctly. The influence of the coefficient of restitution on the bubble rise velocity was not as large as the influence on the bubble size.

1.3.1 Visual bubble flow

In the simple two phase theory it is assumed that all gas which is introduced into the fluidized bed above the gas which is needed to fluidize the bed, passes through the bed as bubbles. Hilligardt and Werther (1986) found that for Geldart B particles the superficial gas velocity through the emulsion phase u_e is significantly larger than the minimum fluidization velocity u_{mf} and that the emulsion phase velocity depends on the superficial gas velocity u_0,

$$\frac{u_e - u_{mf}}{u_0 - u_{mf}} = \begin{cases} 1/3 & \text{for three-dimensional beds} \\ 1/8 & \text{for two-dimensional beds} \end{cases} \tag{1.3}$$

Therefore, not all excess gas $\left(u_0 - u_{mf}\right)$ is available to form bubbles. Hilligardt and Werther (1986) found that the visual bubble flow (defined as the observed bubble flow divided by the excess flow, based on the two phase theory) for Geldart B particles is approximately 0.65 when the height divided by column diameter equals 2, higher in the bed, the visual bubble flow rate will linearly increase to 1.

1.4 Multi-level modeling

The macroscopic circulation patterns in fluidized beds are governed by particle-particle and particle-fluid interactions, which occur at the scale of the size of particles or smaller. With the current computational limitations it is not possible to account for these interactions in a single model. Therefore, a multi-level modeling approach has been adopted in our group. In this approach four different models can be distinguished, the Lattice-Boltzmann Model, the Discrete Particle Model, Continuum Model and the Discrete Bubble Model.

The most detailed model in the multi-level modeling approach involves Direct Numerical Simulation (DNS). The Lattice-Boltzmann Model (LBM) and alternatively the Immersed Boundary Method belong to this class. In these models the fluid flow is fully resolved, i.e. the flow is resolved on a scale which is at least one order of magnitude smaller than the diameter of the particles. Therefore the gas-particle interaction can be computed in a mono or multi disperse particle configuration, yielding closures for the drag force which are needed in the higher level models, see for example van der Hoef et al. (2005).

The Discrete Particle Model, (DPM) is the second model in the multi-level modeling approach. In this model small fluidized beds can be simulated involving up to 1 million particles. In the DPM, the fluid motion is computed by solving the volume-averaged Navier-Stokes equation. The grid size exceeds the particle size and as a consequence, the drag force needs to be prescribed. The particles are tracked individually by solving for all the particles Newton's second law. A detailed collision model is used to account for particle-particle or particle-wall collision, taking into account the energy dissipation during the collisions. With this model, the influence of particle-particle interaction during the fluidization can be investigated, through which the assumptions made in more coarse-grained (continuum) models can be validated.

The third model is the continuum model, i.e. the Two Fluid Model (TFM) or the Multi Fluid Model (MFM), based on the Kinetic Theory of Granular Flow (KTGF). In this model also referred to as the Euler-Euler model the concept of interpenetrating continua is adopted. Closures for particle-fluid and particle-particle interactions are required which can be obtained/tested respectively via DNS and the DPM.

Finally with the Discrete Bubble Model (DBM), industrial scale fluidized bed reactors can be simulated, to predict the macroscopic circulation patterns. The DBM model finds its origin in the modeling of dispersed gas-liquid two-phase flow. Bokkers et al. (2006) modified the model such that the model can be used to simulate industrial scale fluidized bed reactors. The DBM is similar to the DPM, however in the DBM, the emulsion phase is described by the volume-averaged Navier-

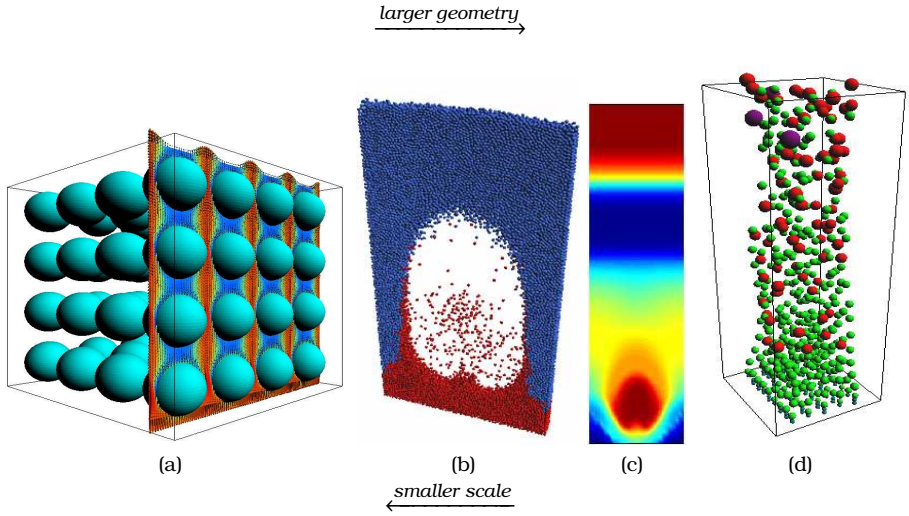

Figure 1.3: Multilevel modeling approach, (a) Direct Numerical Simulation, (b) Discrete Particle Model, (c) Continuum model, (d) Discrete Bubble Model.

Stokes equations whereas the bubbles the tracked individually by solving Newton's second law.

1.5 This thesis

The main objective of this research is to develop a profound and fundamental understanding of particle mixing and circulation patterns in gas-solid fluidized beds at ambient conditions.

To study the prevailing phenomena the research has been divided into two parts. First, the macroscopic circulation patterns and bubble behavior in pseudo-2D beds will be investigated. In chapter 2, Digital Image Analysis (DIA) and Particle Image Velocimetry (PIV) measurements will be performed on a pseudo-2D bed. The reason to perform these experiments in a pseudo-2D bed is that these experimental techniques require visual accessibility. Using DIA information about the bubble behavior in the fluidized bed can be obtained. To measure the macroscopic

circulation patterns, the PIV and DIA measurement technique has been combined. The coupling of the two non-invasive measuring techniques allows to correct for the influence of particle raining through the roof of the bubbles on the number-averaged emulsion phase velocities.

The results of the combined PIV-DIA measurements will be compared in chapter 3 to Discrete Particle Model (DPM) and Two-Fluid Model (TFM) simulations. Furthermore, using the DPM and TFM models, the influence of key parameters, such as the coefficient of restitution, to model a fluidized bed will be investigated.

The second part will focus on the hydrodynamics in a three-dimensional fluidized bed. To measure the macroscopic circulation patterns in a full three dimensional fluidized bed dedicated Positron Emission Particle Tracking experiments have been performed at the University of Birmingham and will be discussed in chapter 4.

In chapter 5, full 3D fluidized bed will be simulated using the Discrete Bubble Model (DBM). To investigate the influence of the bubble-wake acceleration on the hydrodynamics in the fluidized bed, a bubble-wake acceleration model has been implemented in the DBM.

Finally, in an epilogue the findings of this thesis will be discussed and an outlook on further extensions of the measuring techniques and CFD models will be suggested.

CHAPTER 2

Experimental study on the hydrodynamics in a pseudo 2D fluidized bed with PIV and DIA

ABSTRACT

The hydrodynamics of a freely bubbling, gas-solid fluidized bed has been investigated experimentally with two optical non-invasive measuring techniques in two pseudo-2D columns of different width (0.15 vs. 0.30 m) filled with glass beads (400-600 μm) and Linear Low Density Polyethylene (LLDPE) particles (1000-1300 μm), having the approximately the same ratio of Ar/Re_{mf}, ensuring dynamic similarity. Particle Image Velocimetry (PIV) combined with Digital Image Analysis (DIA) has been developed and used to determine simultaneously the emulsion phase circulation patterns, bubble hold-up, bubble size and velocity distributions and visual bubble flow rate profiles. The combination of DIA with PIV allows correcting for the influence of particle raining through the roof of the bubbles on the time-averaged emulsion phase velocity profiles. The number-averaged emulsion phase circulation patterns have been measured as a function of fluidization velocity, bed aspect ratio, bed width and bed material. More-

over, with DIA the average bubble diameter and averaged bubble velocity as a function of height and fluidization velocity have been determined and found to correspond reasonably well with literature correlations. However, the difference in averaged bubble diameter as a function of the height in the fluidized bed for the two different particle types could not be explained by the currently available correlations for the bubble diameter, since the two bed materials used in the experiments have similar ratio of Ar/Re_{mf}*. The difference in observed bubble properties is attributed to differences in the particle collisional properties (coefficients of restitution and the particle friction coefficient). The experimental data provides a basis for development and validation of CFD models to describe the solids-motion in gas-solid fluidized beds.*

2.1 Introduction

Most of the experimental research published in open literature on the hydrodynamics in fluidized beds, is focused on either the emulsion phase circulation patterns or on the bubble behavior, but rarely on both phases simultaneously despite their strong mutual interactions. Solids motion is induced by the bubble movement in the fluidized bed as described in chapter 1, while the bubble diameter and rise velocity (distribution) and local bubble fraction depend on the emulsion phase velocity profiles. In addition, the bubble properties strongly depend on the microscopic particle-particle interactions (a.o. Hoomans et al. (1996) and Goldschmidt et al. (2004)). The mutual interactions make it a prerequisite to obtain information on the solids motion and bubble behavior simultaneously.

Two non-invasive, optical measuring techniques have been combined, namely Particle Image Velocimetry (PIV) and Digital Image Analysis (DIA), so that the instantaneous emulsion phase velocity fields are obtained together with detailed information on the bubble phase (local bubble size and velocity distribution, bubble fraction, etc.), which allows investigation of the mutual interaction between the bubble and emulsion phase in detail. However, a disadvantage of these techniques is the requirement of visual accessibility, limiting the application to a pseudo-2D

fluidized bed.

PIV was first applied to dense gas-fluidized beds by Bokkers et al. (2004), who measured the emulsion phase circulation patterns in freely bubbling gas-solid fluidized beds, in order to validate the extent of particle drift induced by rising gas bubbles predicted by Euler-Lagrange and Euler-Euler models. Link et al. (2004) used PIV to establish fluidization regime maps in spouted fluidized beds and found excellent agreement with their discrete particle simulations. Dijkhuizen et al. (2007) extended the PIV technique to enable the measurement of the granular temperature distribution simultaneously in the fluidized bed. The granular temperature is a very important parameter in the modeling of fluidized beds with Euler-Euler models using closures for the solids phase rheology based on the Kinetic Theory of Granular Flow. PIV has been also applied to study particle behavior in the freeboard region (a.o. Duursma et al. (2001)), and to investigate bubble eruption at the top of the bed (Muller et al. (2007)). Pallares et al. (2006) investigated the particle behavior using phosphorescent tracer particles. They measured the concentration, velocity and dispersion of the tracer particles in a pseudo-2D bed. The particle acceleration of erupting bubbles in the freeboard has been measured by Almendros-Ibanez et al. (2007), with which they experimentally determined the gas through-flow velocity crossing the dome of erupting bubbles.

Lim et al. (1990) were the first to perform DIA measurements to a pseudo 2D fluidized bed studying the bubble size and velocity distribution and bubble hold-up distribution. Aragwal et al. (1997) used DIA to investigate the bubble-wake acceleration in a pseudo-2D bed. Goldschmidt et al. (2003) measured the bed expansion and segregation rates of a binary particle mixture using a high speed color camera. Shen et al. (2004) used DIA to derive relations for the bubble growth and bubble rise velocity in a pseudo 2D bubbling fluidized bed filled with Geldart B particles. Mudde et al. (1994) used DIA to measure the local hold-up, and bubble size, shape and velocity in a bubbling fluidized bed, while Utikar and Randade (2007) used DIA to validate there Euler-Euler model for a single jet fluidized bed. Finally, Lim et al. (2007) investigated the bub-

ble distribution and behavior in bubbling fluidized beds. Hulme and Kantzas (2004) used X-ray fluoroscopy to investigate the bubble properties in a fluidized bed filled with glass beads and with LLDPE particles. The LLDPE particles had a broad particle size distribution of 100 μm up to 1500 μm. Hulme and Kantzas (2004) varied the gas velocity and found larger bubbles at increased superficial gas velocities. They concluded that the bubble properties could be described with the correlations from literature.

To the authors' knowledge, PIV and DIA have never been applied simultaneously before. When using PIV to measure the number-averaged emulsion phase circulation profiles in gas-solid freely bubbling fluidized beds of Geldart B type particles, it is important to correct for the large velocities associated with particles raining through the roofs of the larger bubbles. Correction for particle raining can be achieved by combining PIV with DIA. In this chapter the number-averaged emulsion phase velocity profiles have been determined using PIV combined with DIA in two different pseudo-2D fluidized beds investigating the influence of the fluidization velocity and bed aspect ratio. Moreover, the DIA results have been used to determine the average bubble diameter and bubble velocity as a function of the height in the bed for different bed aspect ratios and fluidization velocities. In addition two types of bed material were investigated. The particle size was selected such that the Archimedes number was approximately the same.

First, the experimental set-up and the two non-invasive measuring techniques are described, followed by a discussion on how the PIV and DIA results are combined. Subsequently, the results on the averaged bubble size and velocity as a function of the height in the bed for different bed aspect ratios and fluidization velocities are discussed and compared with literature correlations. Finally, the influence of the bed aspect ratio, fluidization velocity and bed material on the number-averaged emulsion phase velocity profiles is presented and discussed.

2.2 Experimental

2.2.1 Setup

In Figure 2.1 the flow sheet of the pseudo 2D setup is presented. Two different pseudo-2D fluidized beds with a width of 0.15 m and 0.30 m, both with a height of 0.7 m and a depth of 0.015 m could be mounted in the setup. The front of the 0.15 m bed was made of glass and the back was made of polycarbonate. The front and the back wall of the 0.30 m bed were both made of glass. The side walls of both beds consisted of aluminum strips.

Two different particles types were used in the experiments, glass beads and linear low density polyethylene (LLDPE), both particle types were also used in chapter 2. The glass beads were purchased from Sigmund and Lindner and the particle size ranged from 400 to 600 μm. The density of the glass particles is 2500 $kg.m^{-3}$ and the minimum fluidization velocity has been experimentally determined to be 0.18 $m.s^{-1}$ via the pressure drop versus velocity method, see Kunii and Levenspiel (1991). The second particle type is linear low density polyethylene (LLDPE), courteously provided by LyondellBasell. The original LLDPE particles had a broad particle size distribution; therefore, the particles were sieved to obtain a narrow particle size distribution. The particle size for the LLDPE particles after sieving ranged from 1000 to 1300 μm, yielding an experimental minimum fluidization velocity of 0.24 $m.s^{-1}$. According to Glicksman (1984), when keeping the ratio Ar/Re_{mf} the same for both bed materials, the dynamics should remain the same in the fluidized bed. The ratio Ar/Re_{mf} for glass beds is 1.73×10^3 and for the LLDPE particles is 1.76×10^3.

Air was used as fluidization gas. The air was supplied by a central net and a buffer vessel was used to ensure a steady air supply. The air flow was controlled with two mass flow controllers, to ensure a homogeneous air distribution over the porous plate which was used to inject the air in to the fluidized bed. To prevent electrostatic build-up, the air was first humidified with steam to 60-70% relative humidity. Illumination was achieved with four lamps which directly illuminated the front of the

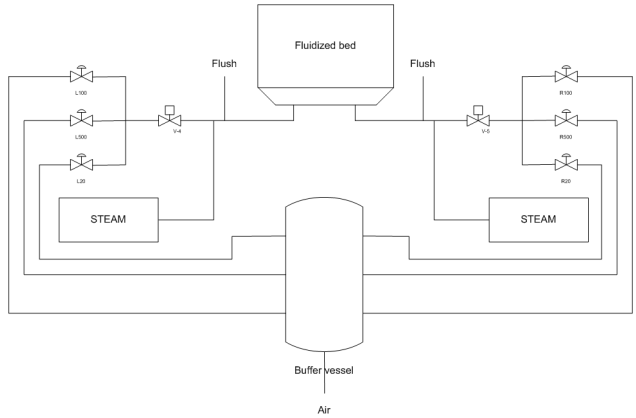

Figure 2.1: Flow sheet of the experimental setup.

Table 2.1: Experimental Settings

Parameter	**Glass beads**	**LLDPE particles**
Min. fluidization vel.† $u_{mf}\ \left(m.s^{-1}\right)$	0.18	0.24
Superficial gas vel. $u_0/u_{mf}(-)$	1.5-3.5	1.5-3.5
Bed diameter $d_{bed}\ (m)$	0.15-0.30	0.15-0.30
Packed bed height (m)	0.15-0.45	0.15-0.45
Particle size distribution (μm)	400-600	1000-1300

† measured experimentally using the pressure drop versus velocity method

fluidized bed (see Figure 2.2). An overview of the experimental settings can be found in Table 2.1.

2.2.2 Measuring techniques

Digital Image Analysis

The principle of DIA is to record images of the fluidized bed with a high speed camera and use the pixel intensity of the recorded images to discriminate between the bubble and the emulsion phase. If the pixel intensity is below a certain threshold value, the pixel area is assigned to

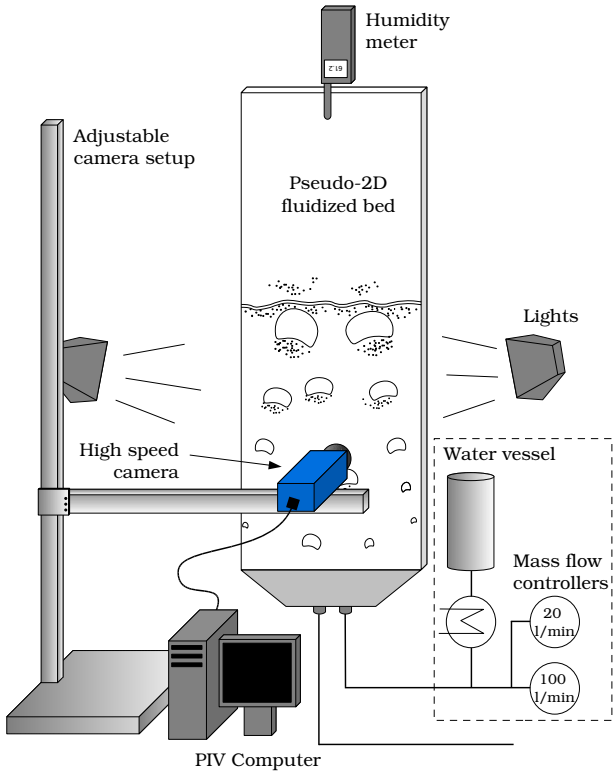

Figure 2.2: A schematic impression of the experimental setup.

the bubble phase, and otherwise to the emulsion phase. The DIA algorithm starts with importing the recorded digital image into a normalized intensity matrix $I_{i,j}$. The original image is shown in Figure 2.3a, whereas the normalized image is depicted in Figure 2.3b. The algorithm continues by removing the walls and the freeboard, using a standard Sobel discrete edge detection algorithm (5×5 mask). Due to inhomogeneous illumination a gradient in the pixel intensity can be observed in Figure 2b. To correct for this, the algorithm determines the local average over a predefined area, in this case the area over which the local average was half the column width (see Figure 2.3c), and subtracts this from the

matrix which results in Figure 2.3d. The final preprocessing step is to smooth the emulsion phase using a 5×5 mask, which results in a more uniform emulsion phase and removes noise from the image. The next step is the phase separation, using an image independent threshold of $T = 0.9$, where T is the average image intensity (see Figure 2.3e). Then, adjoining pixels which are both labeled as bubble phase, are considered as a single bubble. Again, an Sobel edge detection algorithm is used to determine the shape of the bubbles (Figure 2.3f). The equivalent bubble diameter d_b is determined by summing over the tagged adjacent bubble pixels.

$$d_b = \sqrt{\frac{4S_b}{\pi}} \tag{2.1}$$

The center of mass of the bubble in the x and z direction is determined by

$$\vec{x_b} = \frac{1}{N_{pix}} \sum_{i=1}^{N_{pix}} \vec{x_i} \Delta x \tag{2.2}$$

Were N_{pix} is the number of pixels in the bubble under investigation, $\vec{x_i}$ is the position in the x or z direction of the pixel and Δx is the pixel size. The bubble velocities were determined by dividing the displacement of the center of mass of the equivalent spherical bubbles by the time-step between two recorded images.

Finally, the bubble aspect ratio, A_b, is the ratio of vertical span d_z vs. the horizontal span d_x of the bubble under investigation

$$A_b = \frac{d_z}{d_x} \tag{2.3}$$

The bubble properties were determined by performing DIA on images recorded with a LaVision ImagerPro HS CCD camera of the entire bed in order to avoid problems associated with bubbles that are captured only partially in the image. This allowed measuring for at least 30 s using a constant time delay of 10 ms between the images. The DIA program was validated thoroughly using 'synthetic' images (user created images where the size and position of the bubbles were known exactly). An

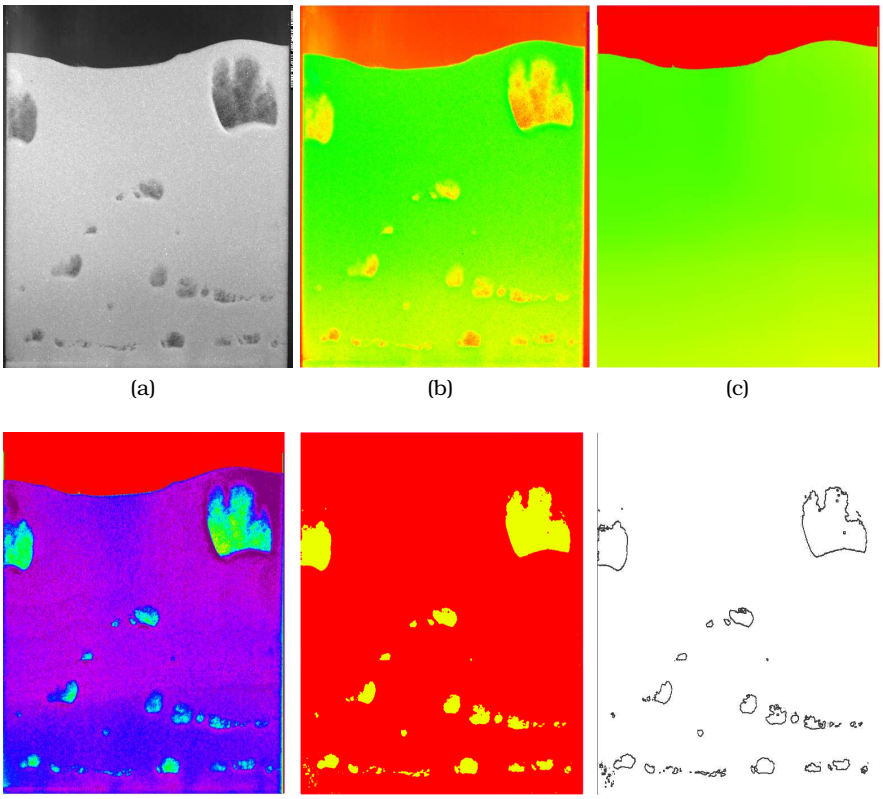

Figure 2.3: The different steps in DIA: (a) original image; (b) normalized image; (c) local average of the normalized image; (d) result after preprocessing image;(e) phase separation; (f) circumference of the bubble

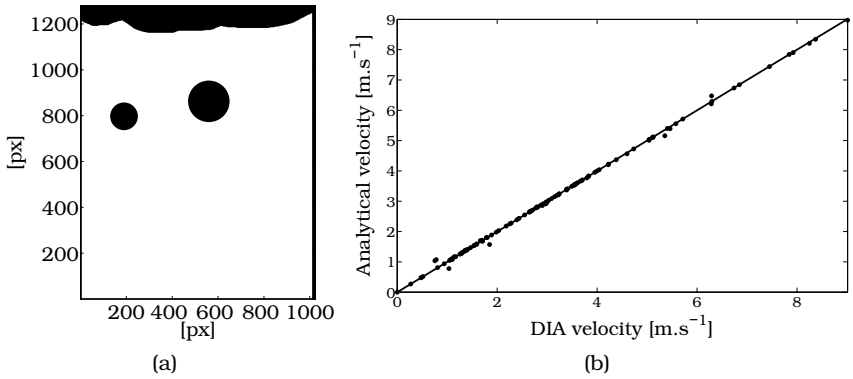

Figure 2.4: The different steps in DIA: (a) example of an user created image; (b) parity plot of the velocity.

illustrative example is given in Figure 2.4a. In Figure 2.4b, the parity plot of the velocity of all bubble shapes, diameters and rise velocities is given. It can be seen that the bubble rise velocity is determined correctly. The velocity of the bubbles in the synthetic images is higher than in the experiments, this is caused by the chosen time-step between the synthetic images.

Particle Image Velocimetry

Particle Image Velocimetry (PIV) is a non-invasive measuring technique developed originally to investigate liquid or gas-liquid systems, but recently extended to gas-solid dispersed flows. The basic principle of PIV is to divide the recorded images into $N \times N$ interrogation areas and use a spatial cross-correlation on two consecutive images

$$\hat{R}[x,y] = \frac{1}{N_x N_y} \sum_{i=1}^{N_x} \sum_{j=1}^{N_y} \left(I'[i,j] - \langle I \rangle\right) \left(I''[i+x, j+y] - \langle I \rangle\right) \tag{2.4}$$

to obtain the average displacement of the particles S_p. Note that the average image intensity $\langle I \rangle$ is subtracted from both images before the cross-correlation is carried out in order to reduce the background corre-

lation. $I'[i, j]$ is the intensity of pixel (i, j) in the first image and $I''[i+x, j+y]$ is the intensity of pixel $(i + x, j + y)$ in the second image.

With the time Δt between the two images and the displacement of the particles S_p inside the interrogation area, the average velocity v_p of the particles inside this particular interrogation area can be calculated with

$$v_p(x, t) = \frac{S_p(x, t)}{M\Delta t} \tag{2.5}$$

where M represents the magnification of the image. Careful selection of the time between two consecutive images is required to minimize the influence of out-of plane movement of particles (see e.g. Westerweel (1997) for further details). By combining the velocities of all interrogation areas, the instantaneous particle velocity profile is obtained.

Images with a resolution of 1024x1280 *pixels* were recorded with a LaVision ImagerPro HS CCD camera which has an internal memory of 2 *GB*. For the PIV measurements, the camera was located at such a distance from the front of the bed, that a single particle was represented by at least 2-3 *pixels* in diameter in order to obtain the desired spatial resolution (Westerweel (1997)). This allowed a measurement area of the fluidized bed of approximately 11.8 x 15 *cm* for the glass beads, for the LLDPE particles the same settings were used. The number-averaged emulsion phase velocity profiles of the entire bed were determined by repositioning the camera 2 to 15 times, depending on the bed width and height, where the data of the different measurements were combined using bilinear interpolation. The bottom 1.5 *cm* of the wide fluidized bed and the bottom 0.6 *cm* of the small fluidized bed above the distributor could not be studied due to lack of visual accessibility. The frequency with which the PIV image pairs were recorded was 4 *Hz*. The exposure time was set to 1 *ms* with an effective time delay of 5.003 *ms* between the images in a pair. With this scheme, the camera was able to record for 3 *minutes*.

2.2.3 Coupling PIV and DIA

Although with PIV the instantaneous average particle velocity in every interrogation zone is measured, the measurement technique does not

account for the varying number of particles in different interrogation zones. To obtain the emulsion phase mass fluxes, one needs to correct for differences in particle density, especially because of particle raining through the bubbles, where a small number of particles have a very high velocity, while the particle mass flux is small. The influence of particle raining is demonstrated in Figure 2.5, for the case of a single bubble injected into a fluidized bed at incipient fluidization conditions.

To filter for particle raining, information on the local particle number density (for every PIV interrogation area) is required. Although PIV is carried out such that all the particles are individually distinguishable (using 2 to 3 *pixels*), the exact number of particles in an interrogation area is difficult to determine automatically for systems with relatively small particles. One could use the average intensity of an interrogation zone as an estimate for the number of particles in that particular zone. However, in this case a very homogeneous illumination is required and a relation between the intensity and the packing degree has to be determined. For larger particles (belonging to Geldart D) this has been done by van Buijtenen et al. (2009). In this work the DIA phase separation technique was used to assign a pixel of the image to the bubble ($\varepsilon^*_{i,j} = 0$) or emulsion phase ($\varepsilon^*_{i,j} = 1$). Assuming (as a first approximation) that there are no particles inside a bubble and that the emulsion phase density is constant, the average emulsion phase fraction $\left\langle \varepsilon^*_{i,j} \right\rangle$ was determined for every interrogation area. The filtered velocity field $\vec{u}^*_{i,j}$ is obtained from the original PIV velocity field $\vec{u}_{i,j}$ via

$$\vec{u}^*_{i,j} = \vec{u}_{i,j} \left\langle \varepsilon^*_{i,j} \right\rangle \tag{2.6}$$

where

$$\left\langle \varepsilon^*_{i,j} \right\rangle = \frac{1}{N^2} \times \sum_{p=i-\frac{N}{2}}^{i+\frac{N}{2}} \sum_{q=j-\frac{N}{2}}^{j+\frac{N}{2}} \varepsilon^*_{p,q} \tag{2.7}$$

Note, that the number-averaged velocity field $\left\langle \vec{u}^*_{i,j} \right\rangle$ is obtained by normalizing over the average emulsion phase fraction:

$$\left\langle \vec{u}^{*}_{i,j} \right\rangle = \frac{\frac{1}{N_f} \sum_{f=1}^{N_f} \left\langle \varepsilon^{*}_{i,j} \right\rangle \vec{u}_{f,i,j}}{\frac{1}{N_f} \sum_{f=1}^{N_f} \left\langle \varepsilon^{*}_{i,j} \right\rangle} \tag{2.8}$$

where f denotes the image number of the PIV images. The number-averaged emulsion phase velocity profiles where obtained by averaging over more than 700 PIV image pairs.

To determine the minimum required measuring time, four measuring series of 3 minutes at the same condition, for both glass beads and LLDPE particles have been performed. One of the measuring series has been compared to the average of the other three series.

$$\sigma_f = \frac{1}{N_f} \sum_{f=0}^{N_p} \sqrt{\frac{\left(v_{x,f} - \overline{v}_x\right)^2 + \left(v_{z,f} - \overline{v}_z\right)^2}{\overline{v}_x^2 + \overline{v}_z^2}} \tag{2.9}$$

The deviation in the measuring series is less than 5% after 200 images.

2.3 Results and Discussion

In this paragraph, the results from the DIA and PIV-DIA measurements are presented and discussed. First, the average bubble diameter as function of the axial position and the average bubble rise velocity as function of the average bubble diameter for different fluidization velocities, bed material, bed aspect ratios and bed widths are presented and compared with literature correlations where available. Then, the number-averaged emulsion phase velocity profiles are presented and discussed, again as function of the fluidization velocity, bed material, bed aspect ratio and bed width. Finally, the novel measuring approach is validated by performing independent Positron Emission Particle Tracking experiments at the University of Birmingham (see chapter 4).

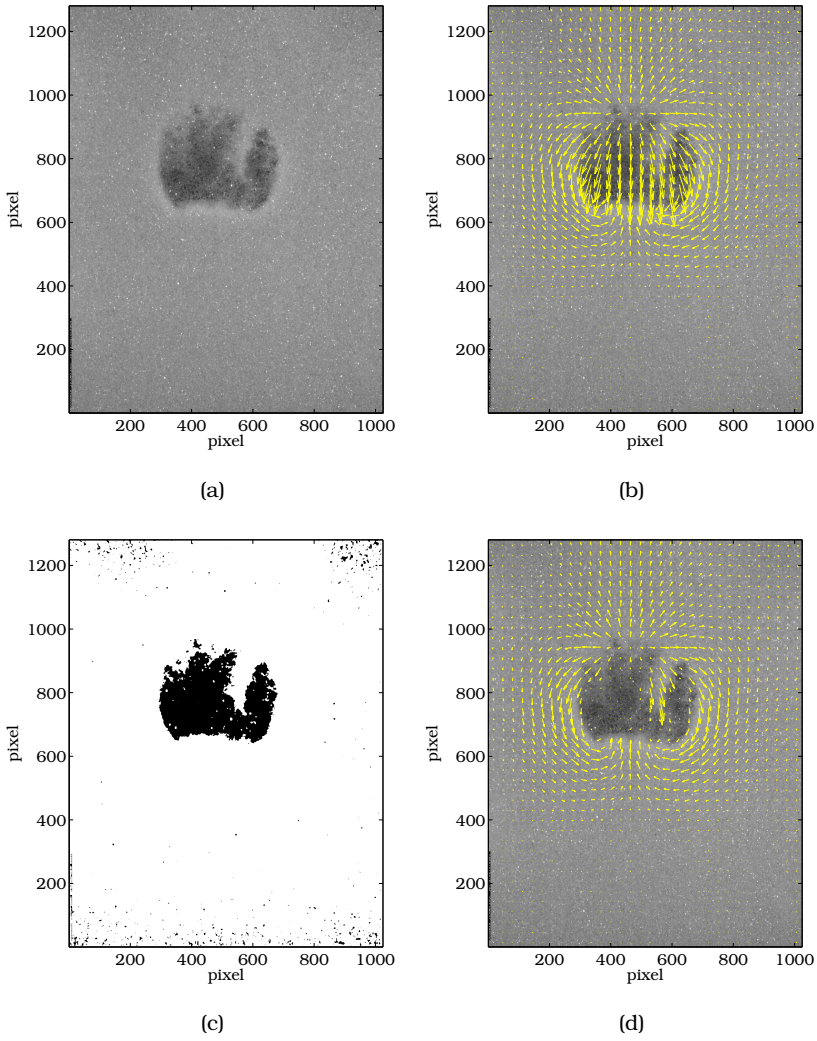

Figure 2.5: Coupling PIV with DIA for a single bubble injection into a fluidized bed at incipient fluidized conditions: (a) original digital image; (b) PIV velocity field without filtering; (c) phase separation; (d) instantaneous flow field after PIV-DIA filtering

2.3.1 Influence of particle raining on the number-averaged emulsion phase velocity profiles

The large influence of filtering out of particle velocities of particles inside bubbles on the number-averaged emulsion phase velocity profiles can be discerned from Figures 2.6 and 2.7. Figure 2.6 shows the number-averaged emulsion phase velocity profiles before (a) and after (b) filtering making use of DIA. Note that for clarity of presentation not all obtained velocity vectors are plotted in the figure. The figure clearly shows that without filtering the up-flow of the emulsion phase in the center of the fluidized bed is strongly underestimated. Since most bubbles move through the fluidized bed at the center of the bed, the effect of the filtering procedure is most pronounced at the center, while the extent of down-flow is hardly affected by the filtering. This becomes clear from Figure 2.7, showing the lateral profiles of the axial emulsion phase velocity at three different heights in the bed. In the experimental results for the lower bed height two peaks in the emulsion phase velocity can be observed, corresponding to the expected lateral movement of the bubbles toward the center of the bed. Note that the number-averaged emulsion phase velocity profiles obtained directly from the PIV results without the filtering wrongly indicates the absence of up-flow of the emulsion phase at lower positions, while it underestimates the maximum longitudinal emulsion phase velocity at higher positions in the bed by a factor as large as 2.

2.3.2 Sensitivity study of the filtering technique

To study the influence of several parameters used in the PIV and DIA measurements a sensitivity study has been conducted. The parameters that have been investigated are the size of the interrogation zone in the PIV measurements, the threshold value in the DIA measurements and the range which was used in the DIA measurements to determine the local average.

By decreasing the size of the interrogation zone in the PIV measurements, the resolution of the measurement is increased and when the fil-

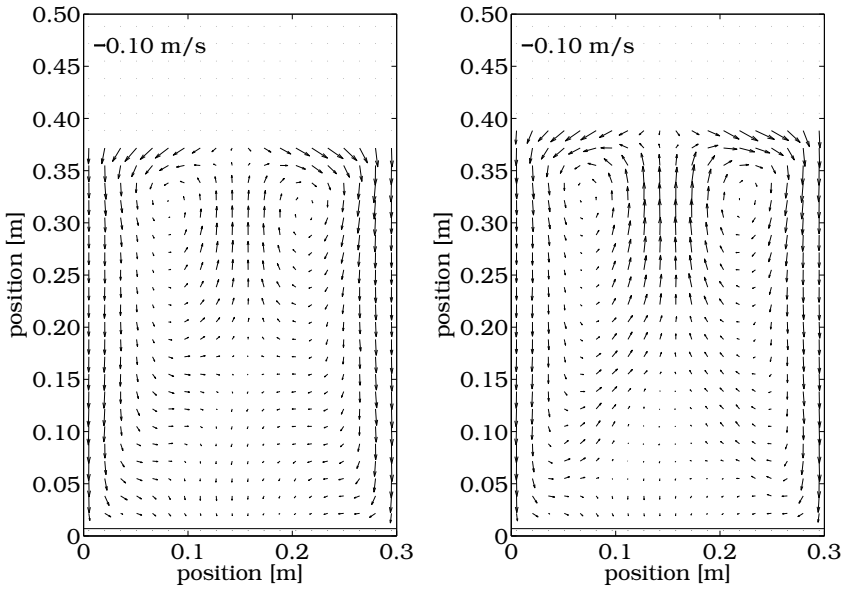

Figure 2.6: Number-averaged emulsion phase velocity profiles for 2.5 u_0/u_{mf} in the 0.30 m fluidized bed filled with glass beads: (a) before filtering using DIA; (b) after filtering using DIA.

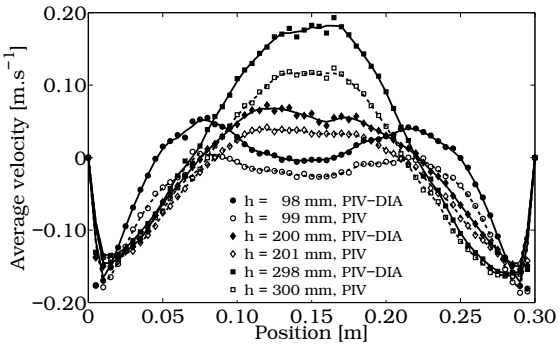

Figure 2.7: Comparison of the number-averaged lateral profiles of the axial emulsion phase velocity between before and after filtering at three heights above the distributor. Fluidization velocity was 2.5 u_0/u_{mf} and the packed bed height was 0.30 m.

tering is performed, the bubble shape can be described more accurately. The interrogation zone has been decreased from 32×32 to 16×16 *pixels* for the PIV measurement using glass beads as bed material, where the superficial gas velocity was set to 3.5 u_0/u_{mf} and the packed bed aspect ratio was 1 using the 0.3 m fluidized bed. As can be seen in Figure 2.8a, where the influence of the interrogation zone on the number-averaged vertical emulsion phase velocity is given at three different heights above the distributor, the interrogation zone has little to no influence on the results.

The influence of the threshold value on the novel filtering technique has been investigated by varying the threshold value between 0.85 and 0.95. If the threshold value is a sensitive parameter, the bubble size can be over- or under predicted and therefore the filtering for the particle raining can be over- or under predicted. In Figure 2.8b the results are presented, for this case the LLDPE particles were used as bed material, the superficial gas velocity was set to 3.5 u_0/u_{mf} and the packed bed aspect ratio was 1 using the 0.15 m fluidized bed. As can be seen from the figure, the influence of the threshold is negligible.

The last parameter investigated is the range used to determine the local average. This was implemented in the DIA algorithm to remove inhomogeneous lighting, however, the measuring area in the PIV measurements is smaller than in the DIA measurements, and therefore a bubble can span over the entire range of the area used in for the local averaging, and subsequently might not be detected as bubble. Therefore, the averaging range has been increased to span over the entire measurement. In Figure 2.8c the results are presented for the same case as used in the threshold case. Again, the influence of the parameter has negligible influence on the final results obtained.

2.3.3 Bubble phase

Equivalent bubble diameter and bubble rise velocity

First, it was investigated how the laterally averaged equivalent bubble diameter varies as function of the height above the distributor for dif-

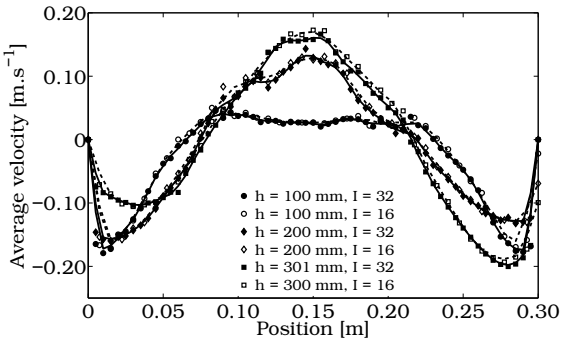

(a)

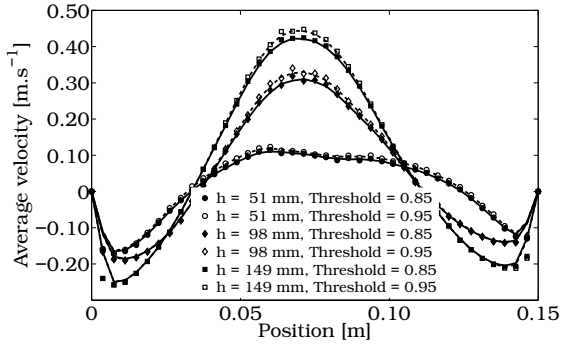

(b)

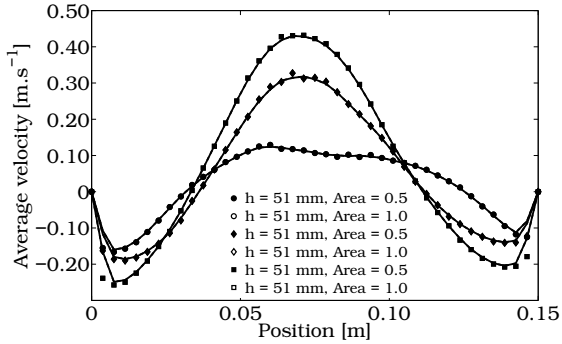

(c)

Figure 2.8: Sensitivity study of the PIV-DIA filtering technique, (a) influence of the interrogation zone, 32×32 and 16×16 pixels; (b) influence of the threshold value, 0.85 vs. 0.95; (c) influence of the local average range 0.5 and 1.

ferent fluidization velocities, bed aspect ratios, bed materials and bed widths (see Figures 2.9 till 2.14). The results show that the averaged bubble diameter increases less than proportionally with the distance to the distributor for both the glass beads and the LLDPE particles. In addition, it was found that larger equivalent bubble diameters are found at higher fluidization velocities. Furthermore, the figures show that the bubble diameter hardly depends on the bed aspect ratio, but is strongly affected by the bed width. The bubble growth is clearly obstructed in the 0.15 m bed, as a result of the prevailing emulsion phase velocity profiles (shown later).

The experimental results for the averaged equivalent bubble diameter as a function of the height in the bed are presented in Figure 2.9 together with a correlation proposed by Shen et al. (2004). They fitted a Darton-like equation for the average bubble size d_b based on DIA experiments, performed in a pseudo-2D freely bubbling fluidized bed using Geldart B type solids:

$$d_b = 0.89\left[\left(u_0 - u_{mf}\right)\left(h + 3.0\frac{A_0}{t}\right)\right]^{(2/3)} g^{(-1/3)} \tag{2.10}$$

where h is the height above the distributor, A_0 is the catchment area (for porous plate $4\sqrt{A_0} = 0.03$ m), t is the depth of the bed and g is the gravitational acceleration. Since both the width and the depth of their fluidized bed were larger than used in this work (their bed dimensions were 0.68×0.07 m vs. bed dimensions in this work of 0.15×0.015 m and 0.30×0.015 m), their correlation overpredicts our experimental results, especially at higher superficial gas velocities. Not only can the bubbles grow to a larger maximum bubble diameter in their set-up, bubbles with a diameter smaller than the bed depth (0.07 m) could not be well detected in their experimental rig. Furthermore, it can be seen that the fluidized bed filled with LLDPE particles, the averaged equivalent bubble diameter is larger than the fluidized bed filled with glass beads and that at 2.5 u_0/u_{mf} the bubble growth for the LLDPE particles is restricted in our experimental setup, where the bubbles in the fluidized bed are restricted at 2.0 u_0/u_{mf}.

Besides that, the influence of the bed aspect ratio on the average

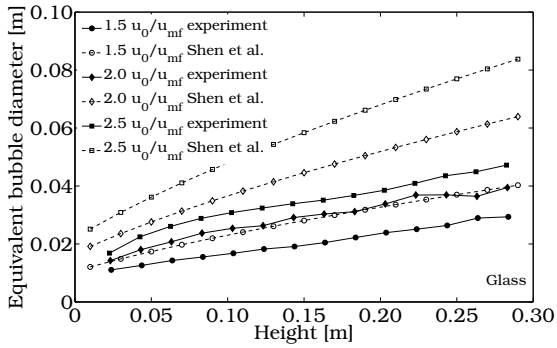

(a)

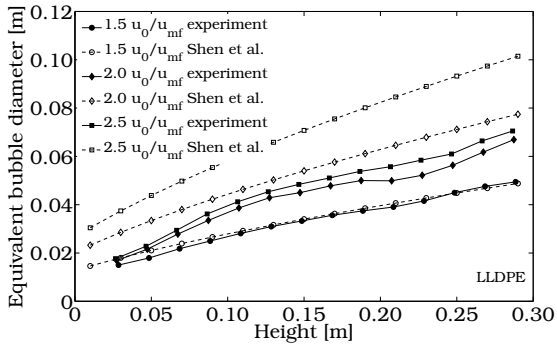

(b)

Figure 2.9: Equivalent bubble diameter as function of the position in the bed above the distributor for different bed materials compared with the correlation proposed by Shen et al. (2004). (a) 0.30 m bed width, bed material glass beads, 0.30 m packed bed height; (b) 0.30 m bed width, bed material LLDPE, 0.30 m packed bed height.

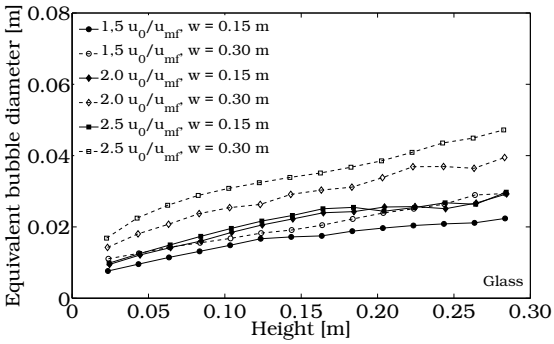

(a)

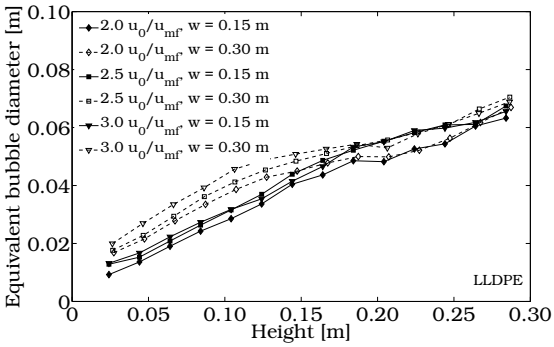

(b)

Figure 2.10: Influence of the bed width on the equivalent bubble diameter as a function of the height in the bed. Solid lines: bed width of 0.15 m; dashed lines: bed width of 0.30 m. The packed bed height was 0.30 m for both bed widths. The bed material was (a) glass beads and (b) LLDPE particles.

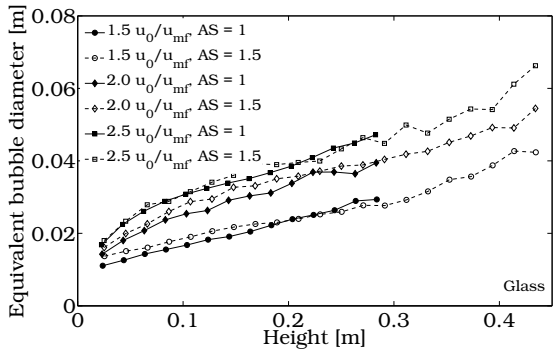

(a)

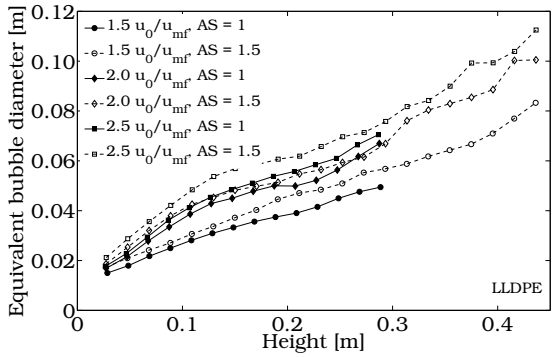

(b)

Figure 2.11: Equivalent bubble diameter as function of the position in the bed above the distributor for different bed materials and aspect ratios. (a) 0.30 *m* bed width, bed material glass beads, 0.30 and 0.45 *m* packed bed height; (b) 0.30 *m* bed width, bed material LLDPE, 0.30 and 0.45 *m* packed bed height.

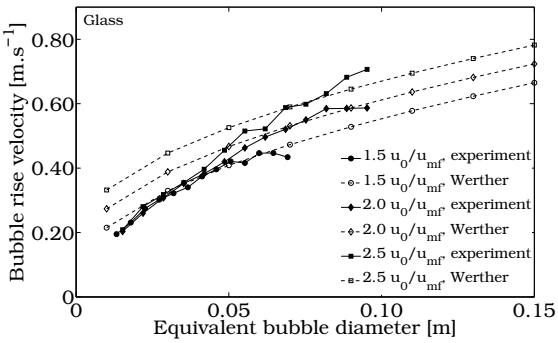

(a)

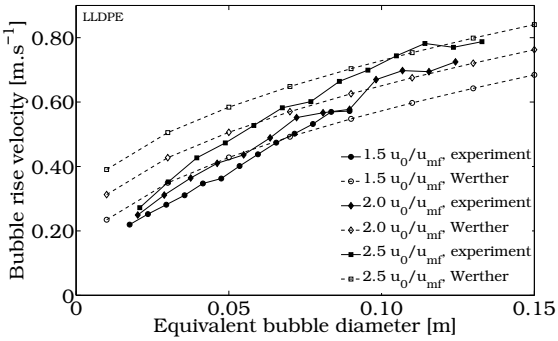

(b)

Figure 2.12: Averaged bubble velocity as function of the bubble diameter for different bed materials compared with the correlation proposed by Werther (1978). (a) 0.30 *m* bed width, bed material glass beads, 0.30 *m* packed bed height; (b) 0.30 *m* bed width, bed material LLDPE, 0.30 *m* packed bed height.

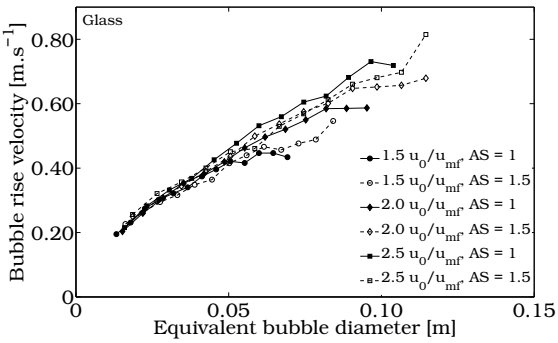

(a)

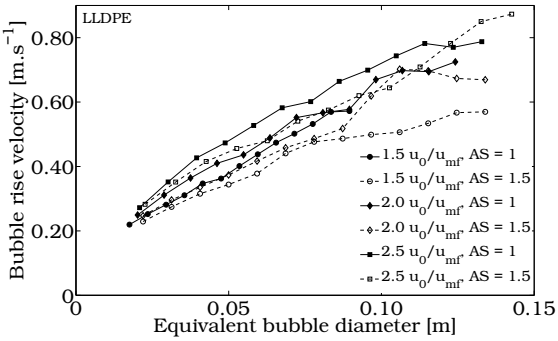

(b)

Figure 2.13: Averaged bubble velocity as function of the averaged bubble diameter for different bed materials and aspect ratios. (a) 0.30 *m* bed width, bed material glass beads, 0.30 and 0.45 *m* packed bed height; (b) 0.30 *m* bed width, bed material LLDPE, 0.30 and 0.45 *m* packed bed height.

bubble diameter has been investigated in the 0.30 m wide fluidized bed, see Figure 2.11. The packed bed height of the fluidized bed has been varied between 0.30 and 0.45 m, i.e. an bed aspect ratio of 1 and 1.5. It can be seen that the aspect ratio has no influence on the average bubble size for the fluidized bed filled with glass beads (Figure 2.11a, however, the average bubble diameter in the fluidized bed filled with LLPDE particles is slightly higher for a bed aspect ratio of 1 compared to 1.5.

In Figure 2.10 the average bubble rise velocity is plotted as a function of the equivalent bubble diameter for the two different beds, where in Figure 2.10a the bed material was glass beads and in Figure 2.10b LLDPE was used as bed material. From this figure the influence of the bed width becomes clear. In the small bed using glass beads as bed material, the bubbles are constricted due to the width of the bed. When LLDPE was used, the bubbles in the wide bed are initially larger, however, when the averaged equivalent bubble diameter reaches approximately 0.05 m in the wide bed, the averaged bubble diameter is restricted due to the influence of the walls.

Subsequently, the measured average bubble rise velocity as a function of the equivalent bubble diameter is plotted for different fluidization velocities and the two bed materials in Figure 2.12 and compared with literature correlations. The bubble rise velocity u_b in a freely bubbling fluidized bed is usually correlated to the bubble diameter and fluidization velocity via a correlation proposed by Werther (1978):

$$u_b = \psi \left(u_0 - u_{mf} \right) + C \sqrt{g d_b} \tag{2.11}$$

where different values ranging between 0.5 and 1 have been proposed for the constant C. Mudde et al. (1994) a.o. suggested for a single isolated bubble 0.5-0.6 for C, in this work the value 0.5 was used. The visual bubble flow rate ψ has been experimentally determined by Hilligardt and Werther (1986) to be approximately 0.65 for Geldart B powders for a bed aspect ratio up to 2. The measured bubble velocity agrees reasonably well with this correlation for both glass beads and LLDPE particles. However, the bubble rise velocities are strongly overestimated for very

small bubbles, where probably experimental errors and wall effects may play an important role.

The influence of the bed aspect ratio on the average bubble rise velocity versus the averaged bubble diameter has been determined in the 0.30 m wide fluidized bed, see Figure 2.13. The packed bed height of the fluidized bed has been varied between 0.30 and 0.45 m. The average bubble rise velocity for the case where the fluidized bed was filled with glass beads, the bed aspect ratio has no influence on the averaged bubble rise velocity, however when the fluidized bed was filled with LLDPE particles, the average bubble rise velocity for a bed aspect ratio of 1 is slightly higher than for the fluidized bed filled to an aspect ratio 1.5.

Visual bubble flow rate

In addition to the average equivalent bubble diameter and average bubble rise velocity, the visual bubble flow rate ψ has been determined. The visual bubble flow rate is defined as the observed bubble flow rate v_b divided by the excess flow rate.

$$\psi = \frac{v_b}{\left(u_0 - u_{mf}\right) A_t} \tag{2.12}$$

To determine the visual bubble flow rate, the volume of the bubbles passing through a horizontal plane in the fluidized bed is summed and then divided by the excess volumetric flow rate of the gas.

In Figure 2.15, the results of the visual bubble flow rate (using the 0.3 m wide fluidized bed) are presented, where in Figure 2.15a the bed material was glass beads and in Figure 2.15b LLDPE. It can be seen that the visual bubble flow rate for both bed materials show a similar qualitative behavior. The measured visual bubble flow rate for both bed materials start at 0.1 just above the distributor and subsequently increase until it reaches a constant value. This indicates either degassing of the emulsion phase, i.e. bubbles grow due to gas exchange from the emulsion phase, or the bubbles at the bottom of the bed are too small to be detected and therefore DIA underestimates the visual bubble flow rate. However, when inspecting to the visual bubble flow rate results

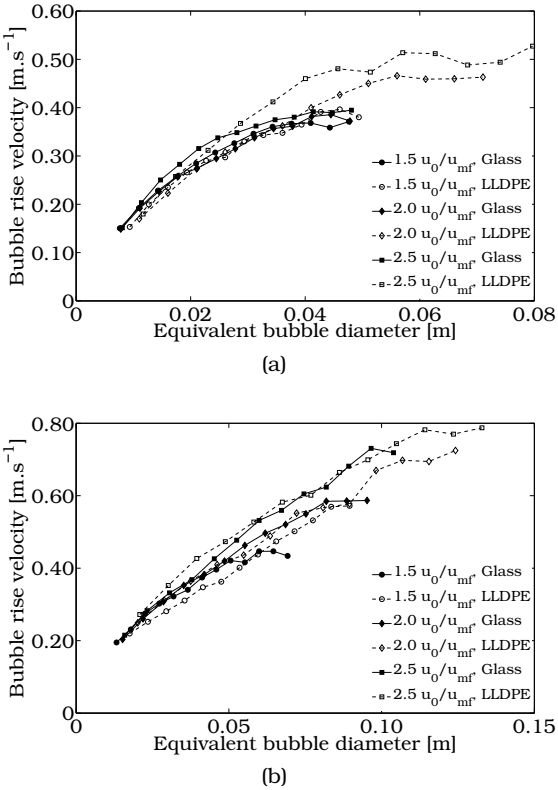

Figure 2.14: Averaged bubble rise velocity as function of the equivalent bubble diameter at different fluidization velocities, (a) 0.15 m bed width, 0.15 m packed bed height; (b) 0.30 m bed width, 0.30 m packed bed height.

quantitatively, the visual bubble flow rate for the glass beads is much lower than that for the LLDPE particles, respectively 0.4 and 0.6, indicating that in the LLDPE experiments more gas is passing through the bed as bubbles compared to the experiments conducted with glass beads, which also explains the difference in measured average equivalent bubble size at lower heights above the distributor. The measured visual bubble flow rate for both the glass beads and the LLDPE particles agrees with the results published by Hilligardt and Werther (1986), who used miniaturized capacitance probes to measure the visual bubble flow rate. However Hilligardt and Werther did not measure the steep increase in the visual bubble flow rate, which is probably explained by the fact that their miniaturized capacitance probes could measure smaller bubbles then the DIA measurement technique used in this work. The LLDPE particles behave as Geldart particle type B, the glass beads which are used in this work are similar (also same minimum fluidization velocity) to the particles which Hilligardt and Werther considered as Geldart D particles because the glass beads behavior could be better described as Geldart D particles. Geldart (1970/71) determined the visual bubble flow rate at the top of a three- and two-dimensional fluidized bed, and found that the visual bubble flow rate for the two dimensional bed varied between 0.4 and 0.6, corresponding nicely with the measured values in this work.

Bubble shape

The final bubble property which will be investigated in this chapter is the bubble shape. In Figure 2.16 the influence of the superficial gas velocity on the bubble shape for both glass beads (Figure 2.16a) and for LLDPE particles (Figure 2.16b) is presented in the 0.3 m wide fluidized bed. Initially, the bubbles in the LLDPE filled fluidized bed are rounder, e.g. the bubble aspect ratio is closer to 1. In addition, for both bed materials it can be seen that if the superficial gas velocity is increased, the bubbles are elongated at the same equivalent bubble diameter. This could be caused by the increased velocity of the gas passing through the bubbles. Furthermore, the bubble aspect ratio for both bed materials

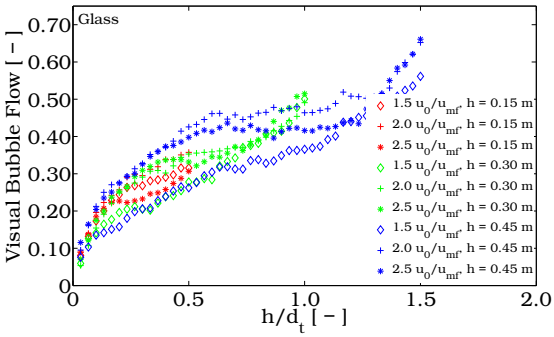

(a)

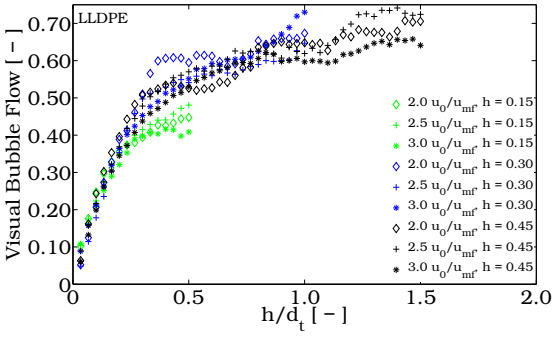

(b)

Figure 2.15: Visual bubble flow as function of the normalized height in the wide fluidized bed, where the fluidized bed was filled to a packed bed height of 0.15, 0.30 and 0.45 m, the bed material was (a) glass beads; (b) LLDPE particles.

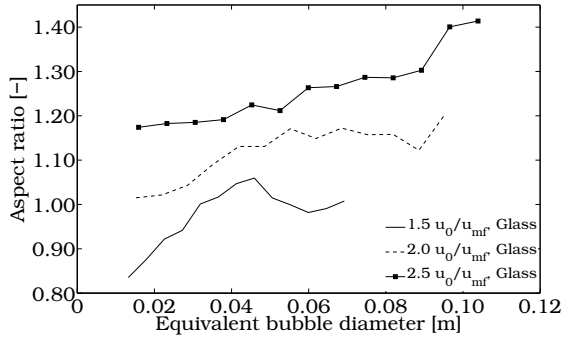

(a)

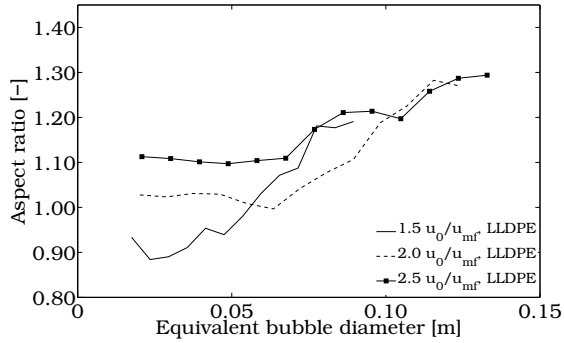

(b)

Figure 2.16: Bubble aspect ratio as a function of the equivalent bubble diameter at various superficial gas velocities. The fluidized bed was filled to a packed bed height of 0.30 *m*, and the bed material was (a) glass beads; (b) LLDPE particles.

remain approximately the same, however when the bubble diameter approaches 8 *cm* the bubble aspect ratio increases rapidly. At this bubble diameter the bubble growth become restricted in the horizontal direction by the walls of the fluidized bed.

2.3.4 Number-averaged emulsion phase velocity profiles

Influence of the superficial gas velocity

In Figures 2.17 and 2.18 the number-averaged emulsion phase velocity profiles (i.e. combined PIV DIA experiment) are given for different superficial gas velocities in the 0.3 m wide fluidized bed filled with respectively glass beads and LLDPE particles to a packed bed height of 0.3 m (bed aspect ratio = 1). Note that only one out of three measured vectors are shown for clarity and that the lateral movement of the emulsion phase just above the distributor could not be measured in out set-up due to of lack of visual accessibility, indicated with a white bar.

At very low fluidization velocities below, 1.5 u_0/u_{mf}, asymmetric flow patterns were obtained, probably caused by a slightly inhomogeneous gas distribution at the bottom of the bed. At higher fluidization velocities, the emulsion phase circulation patterns become much more pronounced, clearly showing two symmetric vortices with their center located in the top half of the fluidized bed. At relatively low superficial gas velocities 2-2.5 u_0/u_{mf}, two additional vortices close to the bottom of the bed can be discerned causing down-flow of the emulsion phase in the center of the bed close to the distributor. However, at fluidization velocities above 2.5 u_0/u_{mf} the down-flow region extends completely down to the distributor and the vortices at the bottom disappear. This corresponds well to observations by many others that the lateral movement of the bubbles is enhanced at higher fluidization velocities caused by the increased circulation of the emulsion phase. The macroscopic circulation patterns are qualitatively similar, however, when the lateral profiles of the axial emulsion phase velocities for the fluidized bed filled with glass beads and LLDPE particles are compared at three different heights above the distributor (see Figure 2.19), it can be seen that the upward number averaged emulsion phase velocity in the center of the bed is much higher at the same excess gas velocity for the LLDPE particles, note the difference in scale used in the graph. In addition, the vortices in the fluidized bed filled with LLDPE particles are more elongated than the fluidized bed filled with glass beads. The behavior of

the emulsion phase corresponds with the bubble behavior discussed in the previous paragraph. Although the averaged bubble rise velocity is similar for both particle types, the averaged equivalent bubble diameter in the bed with the LLDPE particles is much larger, yielding a higher emulsion phase velocity in the center of the bed.

Influence of the bed width

To study the influence of the bed width on the number-averaged emulsion phase velocity profiles, a measurement in the 0.15 m (a) fluidized bed is compared with a measurement in the 0.30 m (b) wide fluidized bed, see Figure 2.20. Both beds were filled with LLDPE particles to a packed bed height of 0.15 m, the superficial gas velocity for both cases was 2.5 u_0/u_{mf}. In the 0.15 m bed, two distinct and developed vortices can be seen, however in the 0.30 m bed, more vortices appear in the fluidized bed, caused by the incomplete lateral movement bubble movement toward the center of the fluidized bed resulting in a undeveloped bubble profile.

In Figure 2.21 the 0.15 m (a) and the 0.30 m (b) have been compared where the bed material in both beds were LLDPE particles the bed was filled to a packed bed aspect ratio of 1, the superficial gas velocity was in both cases 2.5 u_0/u_{mf}. It can be seen that qualitatively the number-averaged emulsion phase velocity profiles are the same. This was already observed by Baeyens and Geldart (1986) who stated that when the same excess gas velocity and aspect ratio were used in fluidized beds with different diameters, the emulsion phase flow patterns and solids down flow velocities are similar.

In Figure 2.22 the number-averaged lateral emulsion phase velocities are compared at three different heights above the distributor. The lateral position in the bed is normalized by dividing the lateral position by the bed width, the three heights are one third, two third and three third of the packed bed height. Although the number-averaged emulsion phase velocity profiles are qualitatively similar it appears that at the lowest height, two distinct velocity peaks can be seen in for the wide bed, however, these can not be seen anymore in the small bed indicating

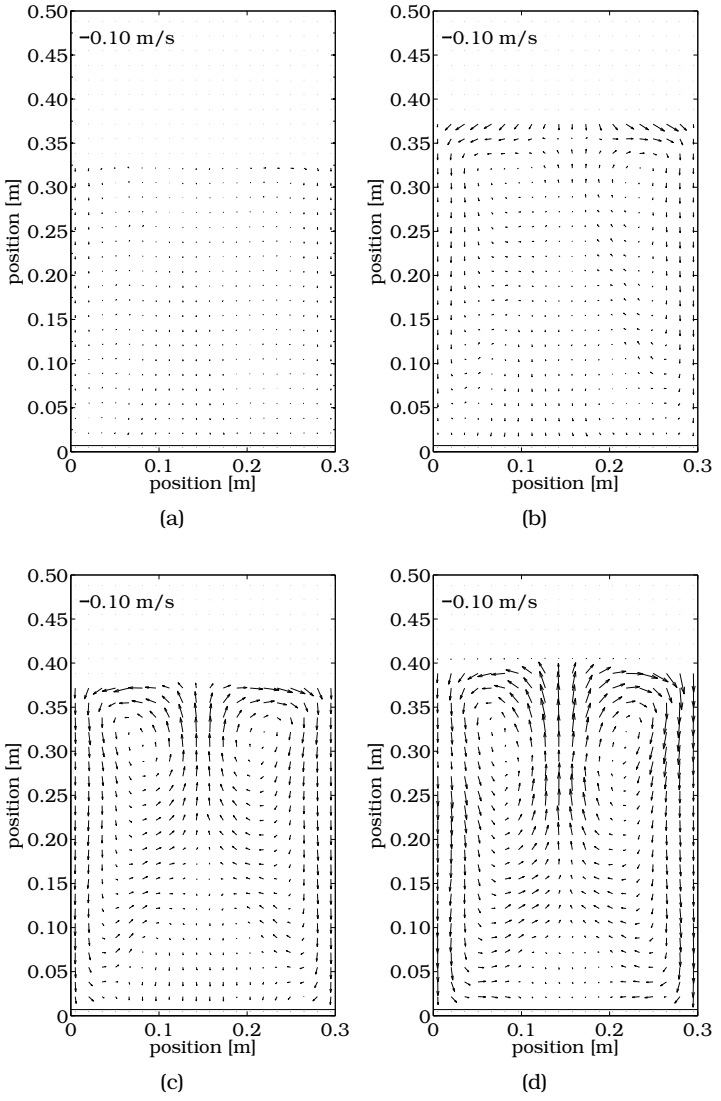

Figure 2.17: Number-averaged emulsion phase velocity for the 0.30 m fluidized bed filled with glass beads, the packed bed height was 0.30 m, the superficial gas velocity was (a) 1.5 u/u_mf; (b) 2.0 u/u_mf; (c) 2.5 u/u_mf; (d) 3.5 u/u_mf.

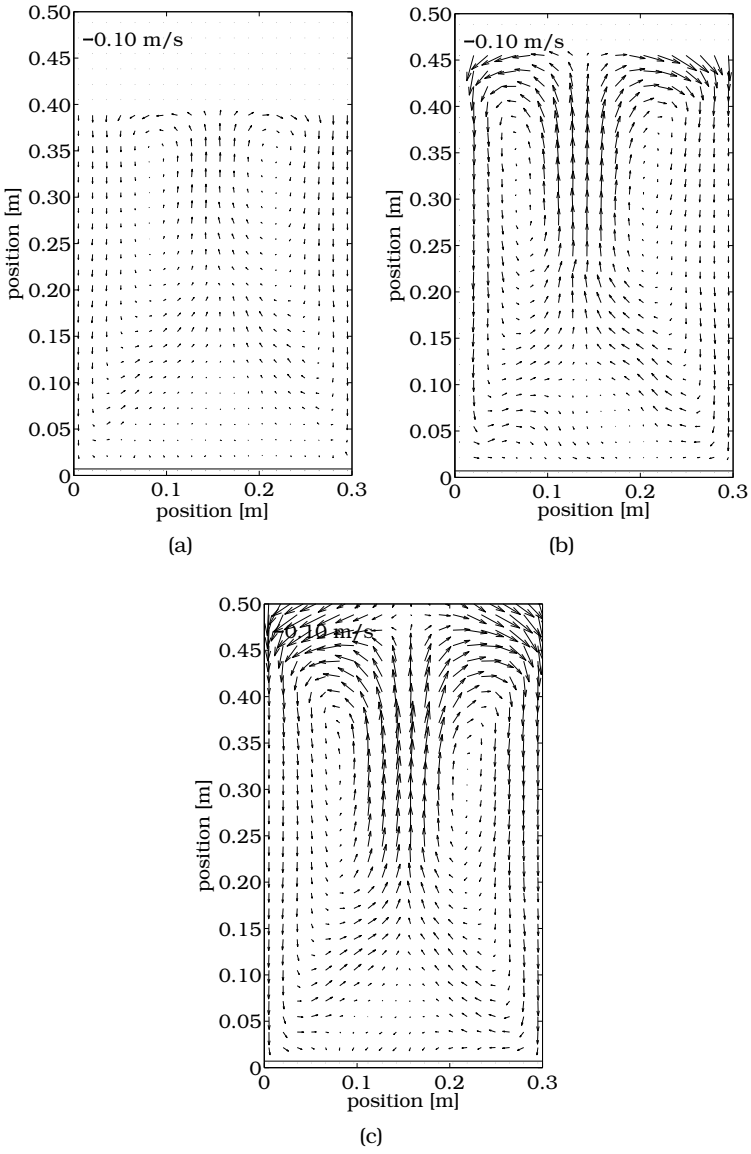

Figure 2.18: Number-averaged emulsion phase velocity for the 0.30 m fluidized bed filled with LLDPE particles, the packed bed height was 0.30 m, (a) 2.0 u/u_mf; (b) 2.5 u/u_mf; (c) 3.0 u/u_mf.

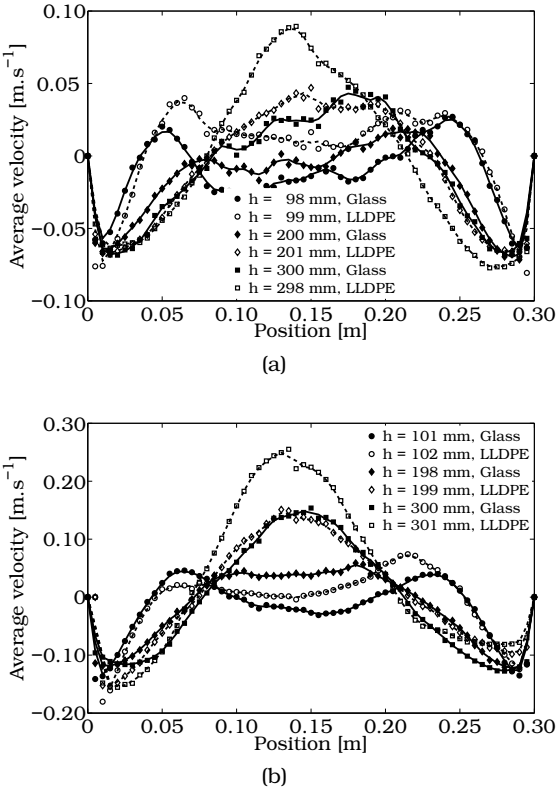

Figure 2.19: Number-averaged lateral profile of the axial emulsion phase velocity for both glass beads and LLDPE particles in the 0.30 m fluidized bed at 100, 200 and 300 mm above the distributor for a fluidization velocity of (a) 2.0 and (b) 2.5 u_0/u_{mf}.

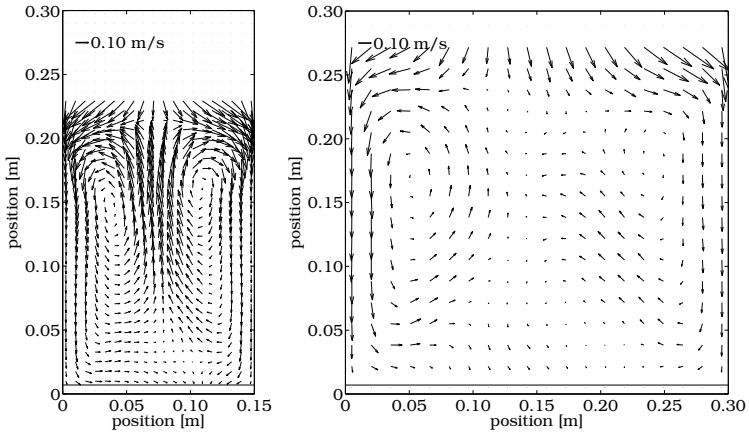

Figure 2.20: Influence of the bed width on the number-averaged emulsion phase velocity for the LLDPE at the same packed bed height (0.15 m). The bed widths were (a) 0.15 m and (b) 0.30 m, the bed material was LLDPE and the fluidization velocity was 2.5 u_0/u_{mf}.

that the bubble plumes originating at the walls have reached each other slightly sooner in the small bed. In addition, the axial velocity at the the packed bed height, the axial emulsion phase velocity in the small bed is higher than for the small bed.

Influence of bed aspect ratio

The effect of the bed aspect ratio on the number-averaged emulsion phase velocity profiles was investigated for the 0.3 m fluidized bed. The results for two different fluidization velocities, 2 and 2.5 u_0/u_{mf} are compared at two aspect ratios respectively 1 and 1.5 for glass beads (Figure 2.23) and LLDPE particles (Figure 2.24). Both Figures show that at higher bed aspect ratios the vortices at the top of the bed become more elongated, while the number-averaged emulsion phase velocity profiles at the bottom of the bed are hardly effected. This indicates that the bubble behavior in the bottom section of the fluidized bed is hardly affected. In Figures 2.25 and 2.26 the number-averaged lateral emulsion phase

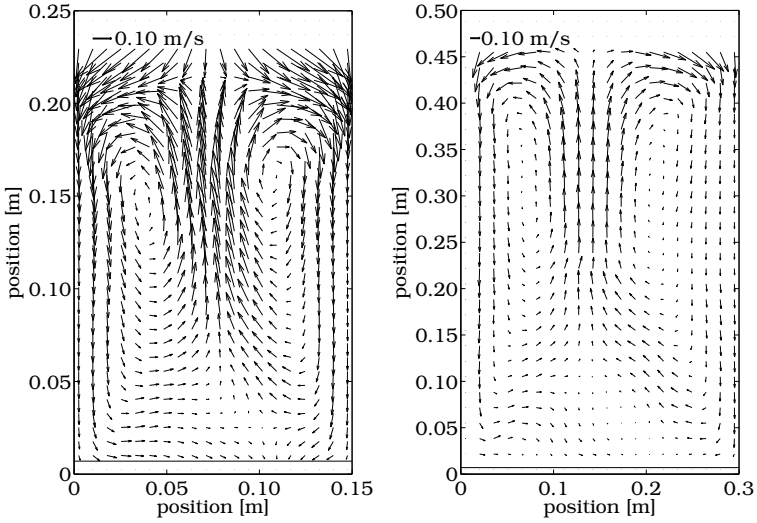

Figure 2.21: Influence of the bed width on the number-averaged emulsion phase velocity for the LLDPE at the same aspect ratio of 1. The bed widths were (a) 0.15 m and (b) 0.30 m, the bed material was LLDPE and the fluidization velocity was 2.5 u_0/u_{mf}.

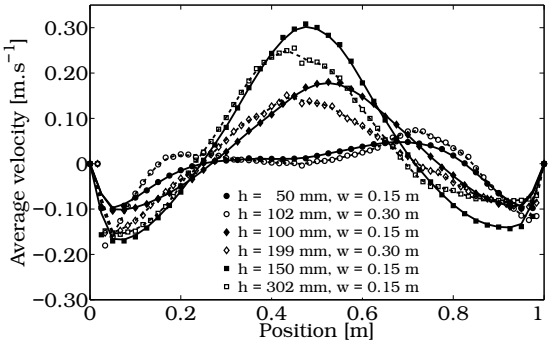

Figure 2.22: Influence of the bed widths on the number-averaged lateral emulsion phase velocity profiles. Superficial gas velocity was 2.5 u_0/u_{mf}, bed material was LLDPE and the packed bed aspect ratio was 1.

velocities are compared at three different heights above the distributor. It can be seen that the number-averaged lateral emulsion phase velocity is for most cases not really affected by the difference in aspect ratio only in case of LLDPE as bed material at a superficial gas velocity of 2.5 u/u_{mf} and at 0.3 m above the distributor is lower, as is the bubble rise velocity for this case.

2.3.5 Validation using Positron Emission Particle Tracking

To validate the new PIV-DIA measuring approach, independent PEPT measurements were performed at the University of Birmingham in the wide pseudo-2D fluidized bed filled with the same glass beads as were used during the PIV-DIA experiments. The difference between the experimental setups used in the DIA-PIV and PEPT experiments was that during the PEPT experiments the air was supplied by a VACOM side channel blower VC375-1009 and the air was humidified in a spray column, for more details about the air supply used during the PEPT measurements, see the experimental setup paragraph in chapter 4.

The principle of PEPT is based on the tracking a radioactively labeled particle, which is taken from the emulsion phase, which is moving through the measuring vessel for a certain time, Parker et al. (1997). When two positions of the tracer particles are known and the time between the two measured positions is known, the velocity between the two points can be calculated, under the assumption that the particle moves in a straight line between the two points. More details about the PEPT measuring technique, reconstruction of the position of the radioactively labeled particle and the calculation of the time-averaged emulsion phase velocity are given in chapter 4.

As can be seen in Figure 2.27, the agreement between the PIV-DIA and the PEPT measurements is good for fluidization velocities up to 2.5 u_0/u_{mf}. When the superficial gas velocity is relatively high (3.5 u_0/u_{mf}), as can be seen in Figure 2.27c, the agreement between the PIV-DIA measurements and the PEPT measurements is still satisfactory for the lower positions in the bed (100 mm above the distributor), however higher in the bed, the agreement is less satisfactory.

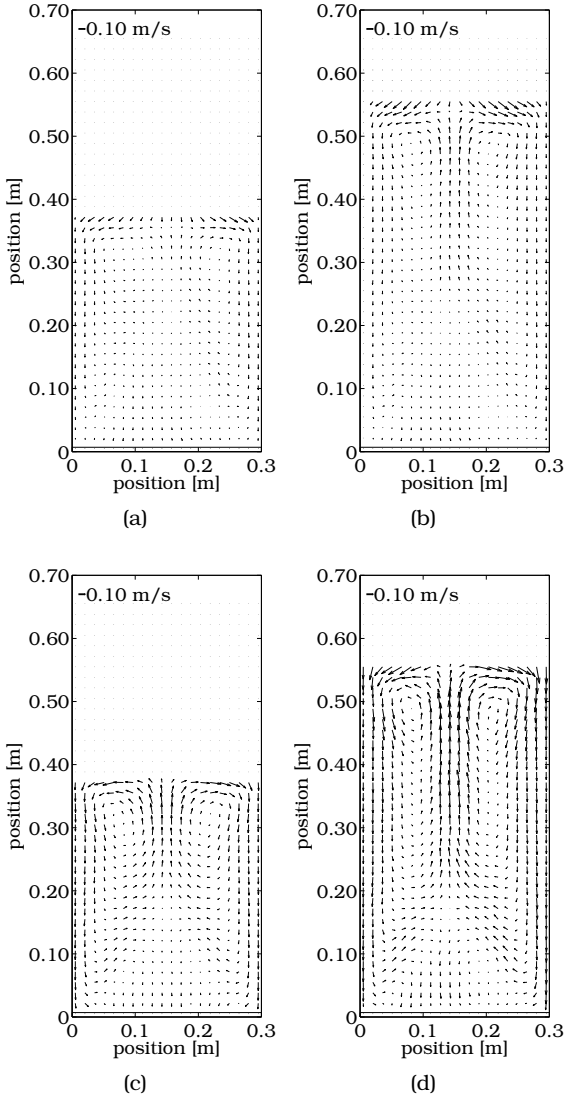

Figure 2.23: Number-averaged emulsion phase velocity for the 0.3 m and 0.45 m fluidized bed filled with glass beads, the superficial gas velocity and the packed bed height were, (a) 2.0 u/u_mf, 0.3 m; (b) 2.0 u/u_mf, 0.45 m; (c) 2.5 u/u_mf, 0.3 m; (d) 2.5 u/u_mf, 0.45 m.

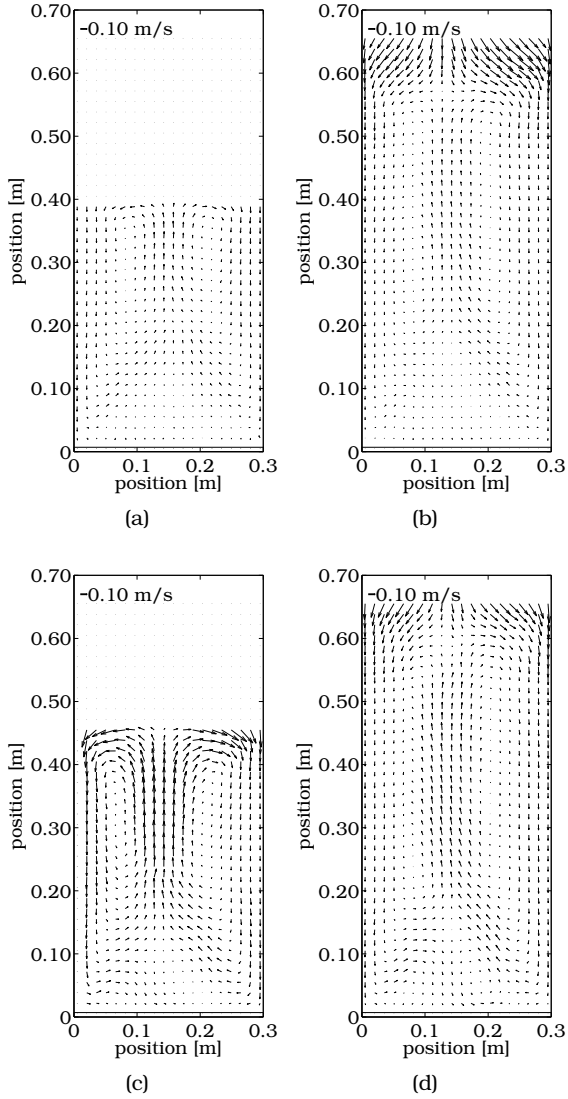

Figure 2.24: Number-averaged emulsion phase velocity for the 0.3 m and 0.45 m fluidized bed filled with LLDPE particles, the superficial gas velocity and the packed bed height were, (a) 2.0 u/u_mf, 0.3 m; (b) 2.0 u/u_mf, 0.45 m; (c) 2.5 u/u_mf, 0.3 m; (d) 2.5 u/u_mf, 0.45 m.

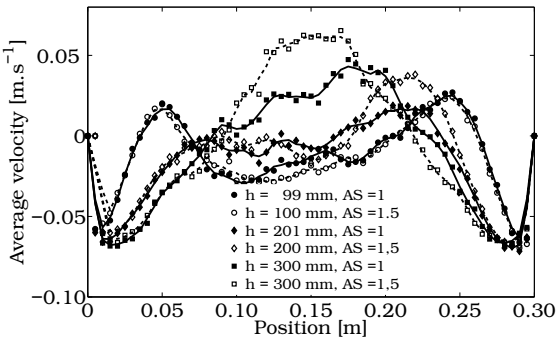

(a)

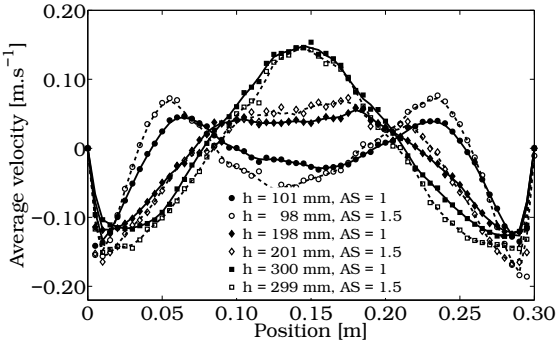

(b)

Figure 2.25: Influence of the aspect ratio on the number-averaged lateral emulsion phase velocity profiles measured in the bed with a width of 0.30 m at 100, 200 and 300 mm above the distributor. The bed material and the superficial gas velocity was (a) glass beads, 2.0 u_0/u_{mf}; (b) glass beads, 2.5 u_0/u_{mf}.

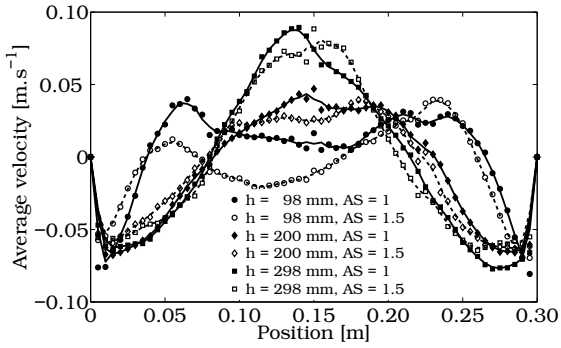

(a)

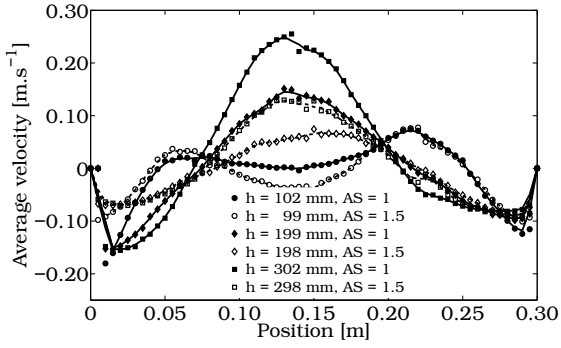

(b)

Figure 2.26: Influence of the aspect ratio on the number-averaged lateral emulsion phase velocity profiles measured in the bed with a width of 0.30 m at 100, 200 and 300 mm above the distributor. The bed material and the superficial gas velocity was (a) LLDPE particles, 2.0 u_0/u_{mf}; (b) LLDPE particles, 2.5 u_0/u_{mf}.

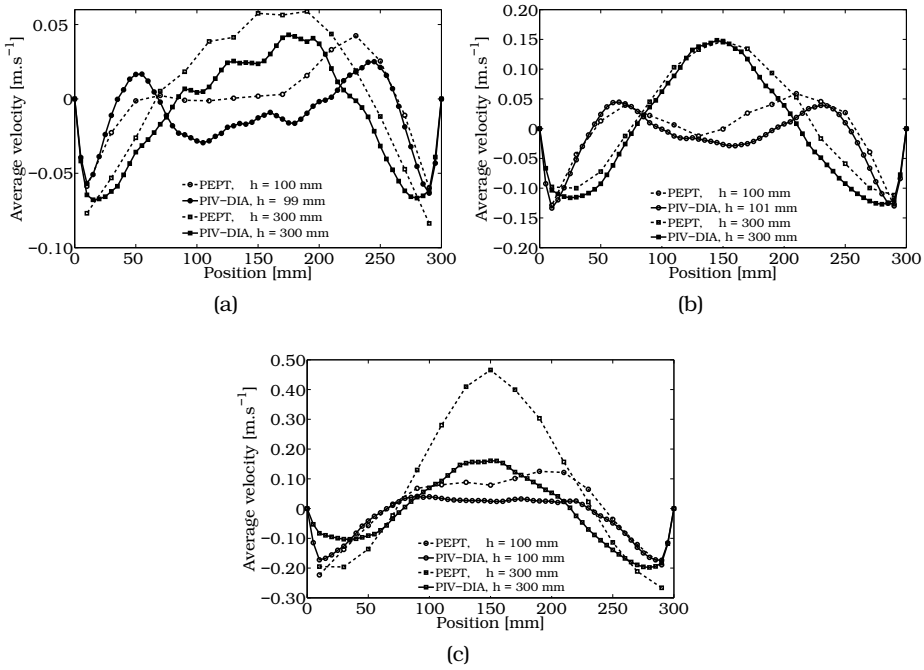

Figure 2.27: Validation of PIV-DIA measurements using independent PEPT measurements using the wide 0.30 m fluidized bed, the bed material were the glass beads. The fluidization velocity and the aspect ratio were (a) 2.0 u_0/u_{mf}, 1; (b) 2.5 u_0/u_{mf}, 1; (c) 3.5 u_0/u_{mf}, 1.

It was shown in the sensitivity analysis, that the deviation between the PIV-DIA and the PEPT measurements can not be attributed to the threshold of the DIA measurements, the size of the interrogation zones in the PIV measurements or the averaging area used in the DIA algorithm.

Another cause which could account for the deviation between the PIV-DIA and PEPT measurements at higher superficial gas velocities and higher heights in the fluidized bed are large clusters of particles raining through the bubble. From literature it is known that smaller bubbles are in general cleaner (less particle raining) than large bubbles. This is confirmed in the PIV measurements, see for example Figure 2.28, where the PIV images are presented as they were recorded with the high-speed

camera (Figures 2.28a and 2.28c) and the corresponding PIV instantaneous velocity vectors (Figures 2.28b and 2.28d). The superficial gas velocity was 3.5 u_0/u_{mf} and the lower left hand corner was at 0.091 m for the left hand side and 0.207 m above the distributor and the top right hand corner was positioned at 0.240 m for the left hand side and 0.389 m above the distributor. It can be seen that when the bubbles are large, the DIA algorithm is unable to distinguish between the raining particles in the bubbles and the emulsion phase. Therefore, the DIA algorithm should be extended such that the raining could be better discarded. In addition, the size of the bubbles should not exceed or approach the size of the area of investigation of the PIV images, because this also influences both the PIV measurements and the DIA correction.

The final possibility for the deviation between the two measuring techniques is that the walls have a large influence on the macroscopic circulation patterns of the emulsion phase. To investigate the influence of the walls in the pseudo-2D fluidized bed, the PEPT measurement at a superficial gas velocity of 3.5 u_0/u_{mf} has been re-processed. In the new analysis, the depth of the fluidized bed has been divided into four zones. The results of the two outer zones (the wall zones) have been combined with each other to obtain more events in these zones. The influence of the walls on the time-averaged vertical emulsion phase velocity is presented in 2.29, were the dashed lines are the results of the complete fluidized bed, and the solid lines are the results of the time-averaged emulsion phase velocity for the wall region, as can be seen the wall effect on the time-averaged emulsion phase velocity of the entire pseudo-2D bed is very small for the number-averaged emulsion phase velocity.

2.4 Conclusions

Two non-invasive, optical measuring techniques, namely Particle Image Velocimetry (PIV) and Digital Image Analysis (DIA), have been combined to obtain the instantaneous emulsion phase velocity profiles together with detailed information on the bubble phase (local bubble size and velocity distribution and bubble fraction), which allows investigating the

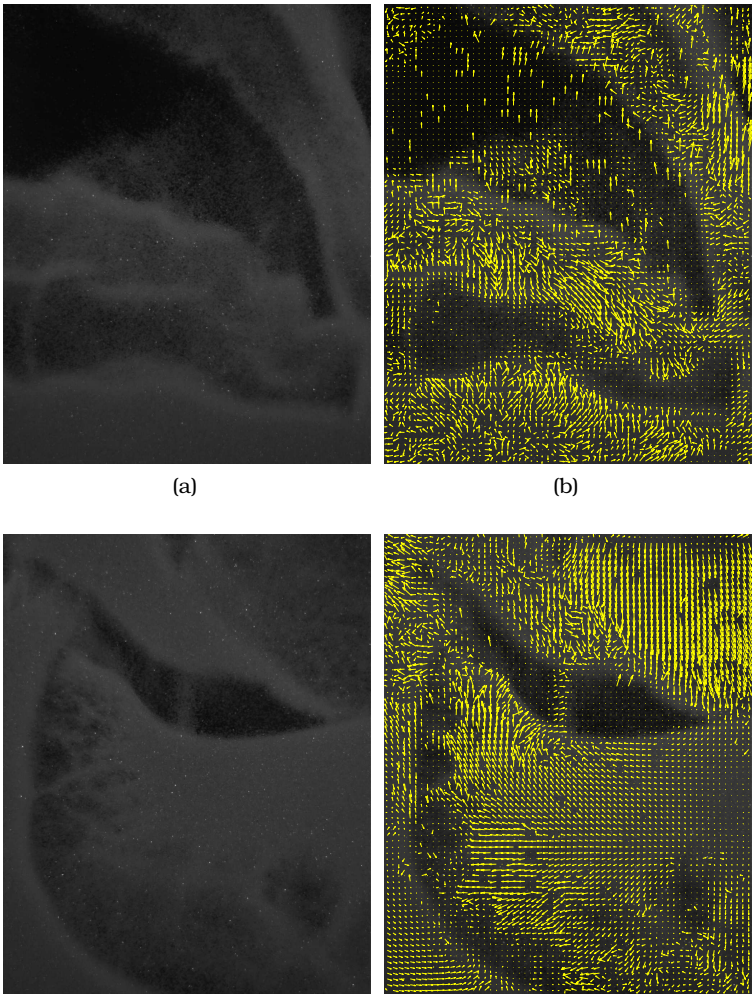

(a) (b)

(c) (d)

Figure 2.28: Influence of raining particles on the PIV-measurements, the superficial gas velocity was 3.5 u_0/u_{mf}, the packed bed height was 0.30 m (a) original image 1; (b) corresponding PIV velocity vector field 1; (c) original image 2; (d) corresponding PIV velocity vector field 2.

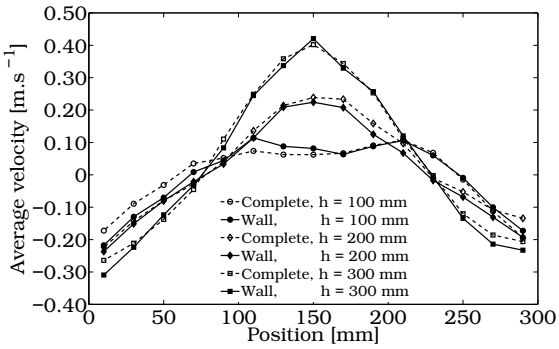

Figure 2.29: Influence of the walls on the time-averaged lateral emulsion phase velocity, determined using PEPT measurements. The fluidization velocity was 3.5 u_0/u_{mf}, bed material was glass beads and the packed bed height was 0.30 m. The solid lines represent the time-averaged lateral emulsion phase velocity at the walls and the dashed lines the time-averaged lateral emulsion phase velocities of the entire bed.

mutual interaction between the bubble and emulsion phase in detail. Moreover, the combination of PIV and DIA allows correcting for the large influence of particles raining through the roof of the bubbles on the number averaged emulsion phase velocity profiles.

The DIA results for the average bubble diameter as function of the height in the bed and the average bubble rise velocity as function of the equivalent bubble diameter were found to compare reasonably well with literature correlations, considering the differences in experimental setup. In addition, the influence of the bed width and bed material on the averaged equivalent bubble diameter was rather large. The average equivalent bubble diameter as function of the height in the bed filled with LLDPE was higher than in the bed filled with glass beads. However, the averaged bubble rise velocity as function of the bubble diameter was not influenced by the bed material. Although in the experiments with LLDPE as bed material showed that the averaged bubble rise velocity was influenced by the packed bed height.

It has been shown that the visual bubble flow is different for different bed materials. The visual bubble flow for the glass beads and LLDPE

agrees with the values for the visual bubble flow published by Hilligardt and Werther (1986). In addition, the shape of the bubble was influenced by the system walls when the bubble diameter was approximately a third of system width. The bubble aspect ratio was increased with increased superficial gas velocity.

The number-averaged emulsion phase velocity profiles show two symmetric vortices with their centers located at the top half of the bed, becoming more pronounced at higher fluidization velocities. Two additional smaller vortices were observed close to the bottom of the bed at lower velocities, which disappear at higher fluidization velocities when the down-flow region extends completely to the bottom of the bed. It was found that the number-averaged emulsion phase velocities do not depend on the bed height, when compared at the same distance from the distributor at the same fluidization velocity.

The lateral upward emulsion phase velocity was higher when the bed was filled with LLDPE particles, which is a directly related to the larger bubbles in the fluidized bed filled with LLDPE particles.

The difference in fluidization behavior can be attributed to the difference in the extent and manner of mechanical energy dissipation between particles-particle interaction and particle-wall interaction. This will be investigated further in chapter 3, using sophisticated CFD models.

The novel measuring technique has been validated using independent and dedicated Positron Emission Particle Tracking experiments at the University of Birmingham. The results show good agreement between the two measuring techniques. However, when the DIA correction algorithm has difficultly to distinguish between raining particles through the bubbles and particles in the emulsion phase, the PIV-DIA measuring technique underestimates the number-averaged emulsion phase velocity. Typically this occurs at higher superficial gas velocities.

Furthermore, it has been shown that the front and back wall of the fluidized bed have no influence on the number-averaged emulsion phase velocity in the axial direction of the fluidized bed i.e. the measured number-averaged emulsion phase velocity at the wall is the same as the number-averaged emulsion phase velocity. Therefore it is

concluded that the novel measuring approach measures the number-averaged emulsion phase velocity of the entire bed.

Finally the experimental data provide a basis for further development and validation of CFD models to describe the solids motion and the bubble behavior in gas-solid fluidized beds, see chapter 3.

CHAPTER 3

Modeling of pseudo 2D fluidized beds using DPM and TFM

ABSTRACT

In this chapter, the influence of microscopic particle properties on the hydrodynamics in a bubbling gas-solid fluidized bed will be investigated using the Discrete Particle Model (DPM) and the Two-Fluid Model (TFM). First, the minimum fluidization velocity is determined with the two models. It is shown that it is important to accurately determine the minimum fluidization velocity for the simulations since it also depends on the collisional properties of the particles. Subsequently the influence of the microscopic particle properties on the macroscopic particle circulation patterns and time-averaged bubble properties are investigated using the Discrete Particle Model. It can be concluded that, for the conditions investigated, indeed bubbles are formed due to collisional dissipation. Furthermore the nature (i.e. due to restitution or friction) of the energy dissipation is important for the shape of the bubbles. It was also shown that the utilization of an effective restitution coefficient is not sufficient to account for the energy dissipated during the particle collisions. In addition it is shown that in a bubbling fluidized bed, the energy is mainly dissipated by fric-

tion between particles and particles and the wall. The influence of the normal restitution coefficient on the macroscopic circulation pattern was investigated with the Two-Fluid Model. The observed influence of the coefficient of restitution in the normal direction agreed with the influence of the coefficient of restitution in the normal direction in the DPM. Finally, the experimental results reported in chapter 2 were compared with simulations performed with the DPM and the TFM. It was shown that when free-slip boundary conditions were applied, the trends for the emulsion phase and the bubble phase can be predicted with the DPM. Furthermore, it was concluded that the collisional model embedded in the TFM is not suitable to simulate a bubbling fluidized bed.

3.1 Introduction

The most commonly used computational fluid dynamics models to describe the hydrodynamics in fluidized beds used in literature are the Discrete Element Model (in this case, the discrete elements are particles therefore the abbreviation of DPM will be used in the remainder of this chapter) and the continuum model (in this chapter the Two-Fluid Model is used, therefore the abbreviation TFM is adopted in the remainder of this chapter).

These models will be used to investigate the influence of the microscopic particle properties on the time-averaged emulsion phase velocity and the time-averaged bubble properties in a bubbling gas-solid fluidized bed. Furthermore, the DPM and TFM simulations will be compared with PIV-DIA and DIA experiments which were presented in chapter 2.

When the DPM is used, every particle in the fluidized bed is tracked using Newton's second law. In the DPM a more detailed (i.e. including friction) collision model is used compared to the TFM. In previous studies, it has been shown that especially the magnitude of the energy dissipation rate has a a profound influence on the fluidization behavior. To account for the particle collisions in the DPM, two different approaches can be used, the hard sphere model and the soft sphere model. The hard sphere model is an event driven model, which means that the

model calculates from one binary collision to the next binary collision. Therefore, the hard sphere model is mainly used in dilute systems, and is less suitable to use for dense fluidized beds. The soft sphere model is a time driven model, which allows for multiple collisions during a single time-step. The contact forces are calculated by taking the overlap and the relative velocity of the particles into account. In this chapter the soft sphere approach is used and will be discussed further in section 3.2.

In our DPM typically about 1 million particles can be simulated, for larger systems, the continuum approach should be used. In the TFM both the gas phase and the solids phase are represented by conservation equations for mass and momentum. To include the particle behavior in the TFM the Kinetic Theory of Granular Flow (KTGF) is used. For the solids phase an additional transport equation is solved for the kinetic energy associated with the fluctuating motion of the particles. The advantage of the TFM is that it can be used to simulate large scale fluidized beds.

Many researchers reported the importance of the collisional properties, for example, Hoomans et al. (1996) included the hard- and soft-sphere model in the DPM, and performed a sensitivity analysis of the bed behavior with respect to the parameters in the collision model. They found that the bed behavior depends strongly on the collisional properties. When ideal particles were used, unrealistic flow behavior was found. Goldschmidt et al. (2001) used the Two-Fluid Model to investigate the effect of collisional parameters on the bed behavior and confirmed the results of Hoomans et al. Furthermore, Lindborg et al. (2007) compared experimental data with results from TFM simulations and stressed the importance of the magnitude of the energy dissipation in order to obtain agreement between experiment and simulation. In addition, they found that the bubble rise velocity was not very sensitive to the restitution coefficient.

First, the DPM and TFM will be described, followed by the numerical verification of the settings of both models used in this study. Furthermore, the minimum fluidization velocity of the particles in both models is determined. Then the influence of the microscopic particle proper-

ties on the macroscopic solids behavior and bubble properties will be investigated. Next, the DPM and TFM results will be compared with the experimental PIV-DIA results which were presented in chapter 2 and finally the main conclusions from this chapter are given.

3.2 Discrete Particle Model

3.2.1 Gas phase dynamics

In the DPM, the gas phase is described by the continuity equation (3.1) and the volume-averaged Navier-Stokes equation (3.2), following Anderson and Jackson (1967):

$$\frac{\partial\left(\varepsilon_g \rho_g\right)}{\partial t} + \nabla \cdot \left(\varepsilon_g \rho_g \vec{u}_g\right) = 0 \tag{3.1}$$

$$\frac{\partial\left(\varepsilon_g \rho_g \vec{u}_g\right)}{\partial t} + \nabla \cdot \left(\varepsilon_g \rho_g \vec{u}_g \vec{u}_g\right) = -\varepsilon_g \nabla p_g - \nabla \cdot \left(\varepsilon_g \vec{\tau}_g\right) - \vec{S} + \varepsilon_g \rho_g \vec{g} \tag{3.2}$$

where ε_g, ρ_g, p_g and $\vec{g}$ are respectively the gas phase porosity, gas phase density, gas phase pressure and the gravitational acceleration. The gas phase density is determined by the equation of state for an ideal gas. $\vec{\tau}_g$ is the gas phase viscous stress tensor, which is assumed to obey the Newtonian form (Bird et al. (1960)),

$$\vec{\tau}_g = -\mu_g \left[\nabla \vec{u}_g + \left(\nabla \vec{u}_g\right)^T - \frac{2}{3}\vec{\vec{I}}\left(\nabla \vec{u}_g\right)\right] \tag{3.3}$$

μ_g is the shear viscosity of gas phase and $\vec{\vec{I}}$ the unit tensor. $\vec{S}$ represents the source term, which accounts for the momentum exchange between the gas phase and the particles. The source term is given by

$$\vec{S} = \frac{1}{V} \int \sum_{k=0}^{N_p} \frac{V_{p,k}\beta}{1-\varepsilon_g} \left(\vec{u} - \vec{v}_{p,k}\right) \delta\left(\vec{r} - \vec{r}_{p,k}\right) dV \tag{3.4}$$

The distribution function, δ, distributes the force exerted on the gas phase by the particles to the Eulerian grid.

3.2.2 Particle dynamics

The motion of every particle in the DPM is computed with Newton's second law of motion

$$m_p \frac{d\vec{v}_p}{dt} = \sum \vec{F} = \vec{F}_{external} + \vec{F}_{contact} \tag{3.5}$$

where m_p and $\vec{v}_p$ denote the particle mass and velocity. The total force acting on the particles is divided into an external and a contact force, which will be discussed subsequently.

External force

The external force, $\vec{F}_{external}$, is the sum of all external forces acting on a particle and is calculated using

$$\vec{F}_{external} = m_p \vec{g} - V_p \nabla p_g + \frac{V_p \beta}{1 - \varepsilon_g} \left(\vec{u}_g - \vec{v}_p \right) \tag{3.6}$$

The first term of the external force, is the gravitational force, the second term is the force due to the pressure gradient in the gas phase, and the third term is the drag force exerted by the gas phase on the particle, where β represents the inter-phase momentum exchange coefficient, which is given by

$$\beta = 18 \left(1 - \varepsilon_g \right) \varepsilon_g \mu_g \frac{F}{d_p^2} \tag{3.7}$$

In which F is the dimensionless drag force. In this work, the dimensionless drag force expression suggested by van der Hoef et al. (2005) has been used. van der Hoef et al. (2005) derived their dimensionless drag force expression from Lattice Boltzmann simulations for monodisperse configurations, and is defined as

$$F = F_0 \left(\varepsilon_g \right) + F_1 \left(\varepsilon_g \right) Re \tag{3.8}$$

where

$$F_0\left(\varepsilon_g\right) = 10\frac{\left(1-\varepsilon_g\right)}{\varepsilon_g^2} + \varepsilon_g^2\left(1 + 1.5\sqrt{1-\varepsilon_g}\right)$$

$$F_1\left(\varepsilon_g\right) = \frac{0.48 + 1.9\left(1-\varepsilon_g\right)}{18\left(\varepsilon_g\right)^2}$$

$$Re = \frac{\varepsilon_g d_p \left(\vec{u}_g - \vec{v}_p\right)\rho_g}{\mu_g}$$

To obtain the drag force, the dimensionless drag force has to be multiplied with the Stokes-Einstein equation, $3\pi\mu_g d\vec{U}F$, where $\vec{U} = \varepsilon_g\left(\vec{u}_g - \vec{v}_p\right)$.

Contact force

The contact force, $\vec{F}_{contact}$, is the sum of all individual contact forces exerted by all particles in contact with the particle under consideration. A soft-sphere collision model is used to describe the contact force. The reason that the soft-sphere collision model is used instead of the hard-sphere model, is because the soft-sphere collision model is better suited for dense fluidized beds due to the high collision frequency. In the soft-sphere model the collisions are described with a linear spring/dash-pot model, proposed by Cundall and Strack (1979) and depicted in Figure 3.1. When the soft-sphere collision model is used, in addition to the equation of motion for every particle (see Equation 3.5), the rotational motion has to be solved,

$$I\frac{d\vec{\omega}}{dt} = \vec{T} \tag{3.9}$$

where I, ω and $\vec{T}$ are respectively the moment of inertia, the angular velocity and the torque acting on the particle.

The total contact force between particles a and b is divided into a normal, $\vec{F}_{ab,n}$, and a tangential component, $\vec{F}_{ab,t}$

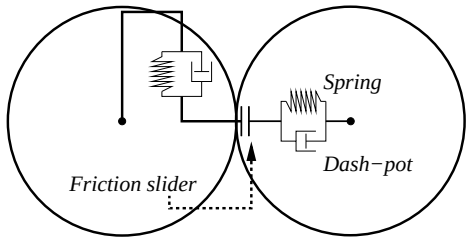

Figure 3.1: Graphical representation of the linear spring/dash-pot soft-sphere model, after Hoomans (1999)

$$\vec{F}_{contact,a} = \sum_{b} \left(\vec{F}_{ab,n} + \vec{F}_{ab,t} \right) \tag{3.10}$$

The normal component of the contact force between particle a and b, is calculated using

$$\vec{F}_{ab,n} = -k_n \delta_n \vec{n}_{ab} - \eta_n \vec{v}_{ab,n} \tag{3.11}$$

in which k_n, $\vec{n}_{ab}$, η_n, $\vec{v}_{ab,n}$ and δ_n are respectively the spring stiffness in the normal direction, the normal unit vector, the damping coefficient in the normal direction, relative velocity and the overlap between the particles in the normal direction. For the tangential component of the contact force, two cases should be distinguished, namely "sticking" and "sliding". If the tangential component is sufficiently high, the impact can be described as "sliding" during the entire collision, however, when after the initial sliding phase the relative tangential velocity between the two colliding particles becomes zero, the impact of the particles belongs to the sticking case.

$$\vec{F}_{ab,t} = \begin{cases} -k_t \delta_t - \eta_t \vec{v}_{ab,t} & \text{for } |\vec{F}_{ab,t}| \leq \mu_f |\vec{F}_{ab,n}| \quad \text{sticking} \\ -\mu_f |\vec{F}_{ab,n}| \vec{t}_{ab} & \text{for } |\vec{F}_{ab,t}| > \mu_f |\vec{F}_{ab,n}| \quad \text{sliding} \end{cases} \tag{3.12}$$

where k_t, $\vec{t}_{ab}$, η_t, $\vec{v}_{ab,t}$, μ_f and δ_t are respectively the spring stiffness in the tangential direction, the tangential unit vector, the damping coefficient in the tangential direction, relative velocity, coefficient of friction

and the overlap between the particles in the tangential direction. The parameters needed to calculate the normal and tangential components of the total contact force are listed in Table 3.1.

3.2.3 Collisional parameters DPM

In order to calculate the total contact force five parameters have to be determined: the spring stiffness in the normal and tangential direction (k_n and k_t), the coefficient of restitution in the normal and tangential direction (e_n and e_t) and the friction coefficient μ_f.

When the spring stiffness in the normal direction is set to an infinitely high value, the soft-sphere model converges toward the hard-sphere model (Hoomans (1999)). However, the disadvantage of an infinitely high spring stiffness in the normal direction is that it requires an infinitely small time-step to compute the contact forces. Therefore it has to be demonstrated that the chosen spring stiffness is large enough to obtain simulation results which are independent of the value of the spring stiffness in the normal direction. When the spring stiffness in the normal direction is known, the tangential spring stiffness in the soft-sphere is calculated using a.o. the normal spring stiffness, see Table 3.1.

Furthermore, the coefficient of restitution in the normal and tangential direction determine the amount of kinetic/rotational energy which is dissipated during a collision between two particles or a particle and a wall. Finally, the friction coefficient accounts for the energy dissipation due to non perfectly smooth particles. The coefficient of restitution in the normal and tangential direction and friction coefficient can be determined with accurate impact measurements, see Kharaz et al. (1999).

Table 3.1: Equations used in the soft-sphere model for the contact force, after Hoomans (1999).

Parameter	**Equation**
Normal displacement	$\delta_n = (R_a + R_b) - \left\|\vec{r}_a - \vec{r}_b\right\|$
Tangential displacement	$\delta_t(t) = \int_{t_0}^{t} \vec{v}_{ab,t} dt$
Normal damping coefficient	$\eta_n = \begin{cases} \dfrac{-2\ln e_n \sqrt{m_{ab}k_n}}{\sqrt{\pi^2 + \ln^2 e_n}} & \text{if } e_n \neq 0 \\ 2\sqrt{m_{ab}k_n} & \text{if } e_n = 0 \end{cases}$
Tangential damping coefficient	$\eta_t = \begin{cases} \dfrac{-2\ln e_t \sqrt{\frac{2}{7}m_{ab}k_t}}{\sqrt{\pi^2 + \ln^2 e_t}} & \text{if } e_t \neq 0 \\ 2\sqrt{\frac{2}{7}m_{ab}k_t} & \text{if } e_t = 0 \end{cases}$
Reduced mass	$m_{ab} = \left(\frac{1}{m_a} + \frac{1}{m_b}\right)^{-1}$
Normal vector unit	$\vec{n}_{ab} = \dfrac{\vec{r}_b - \vec{r}_a}{\left\|\vec{r}_b - \vec{r}_a\right\|}$
Tangential vector unit	$\vec{t}_{ab} = \dfrac{\vec{v}_{ab,t}}{\left\|\vec{v}_{ab,t}\right\|}$
Relative velocity between particles a and b	$\vec{v}_{ab} = (\vec{v}_a - \vec{v}_b) + (R_a\vec{\omega}_a + R_b\vec{\omega}_b) \times \vec{n}_{ab}$
Normal component of relative velocity	$\vec{v}_{ab,n} = (\vec{v}_{ab} \cdot \vec{n}_{ab})\,\vec{n}_{ab}$
Tangential component of relative velocity	$\vec{v}_{ab,t} = \vec{v}_{ab} - \vec{v}_{ab,n}$
Tangential spring stiffness	$k_t = \frac{2}{7}\left(\dfrac{\pi^2 + (\ln e_t)^2}{\pi^2 + (\ln e_n)^2}\right)k_n$
Moment of inertia	$I = \frac{2}{5}m_a R_a^2$
Torque acting on particle	$\vec{T}_a = \sum_b \left(R_a\vec{n}_{ab} \times \vec{F}_{t,ab}\right)$
Normal contact time	$t_{contact,n} = \sqrt{\dfrac{\pi^2 + (\ln e_n)^2}{B_2 k_n}}$,
Tangential contact time	$t_{contact,t} = \sqrt{\dfrac{\pi^2 + (\ln e_t)^2}{B_1 k_t}}$
B_1, B_2	$\frac{7}{2}\left(\frac{1}{m_a} + \frac{1}{m_b}\right)$, $\left(\frac{1}{m_a} + \frac{1}{m_b}\right)$

3.3 Two-Fluid Model

In the TFM, the gas phase and solids phase are described by conservation equations for mass (3.13 and 3.14) and momentum (3.15 and 3.16)

$$\frac{\partial\left(\varepsilon_g\rho_g\right)}{\partial t}+\nabla\cdot\left(\varepsilon_g\rho_g\vec{u}_g\right)=0 \tag{3.13}$$

$$\frac{\partial\left(\varepsilon_s\rho_s\right)}{\partial t}+\nabla\cdot\left(\varepsilon_s\rho_s\vec{u}_s\right)=0 \tag{3.14}$$

$$\frac{\partial\left(\varepsilon_g\rho_g\vec{u}_g\right)}{\partial t}+\nabla\cdot\left(\varepsilon_g\rho_g\vec{u}_g\vec{u}_g\right)=-\varepsilon_g\nabla p_g-\nabla\cdot\varepsilon_g\bar{\bar{\tau}}_g-\beta\left(\vec{u}_g-\vec{u}_s\right)+\varepsilon_g\rho_g\vec{g} \tag{3.15}$$

$$\frac{\partial\left(\varepsilon_s\rho_s\vec{u}_s\right)}{\partial t}+\nabla\cdot\left(\varepsilon_s\rho_s\vec{u}_s\vec{u}_s\right)=-\varepsilon_s\nabla p_g-\nabla\cdot\varepsilon_s\bar{\bar{\tau}}_s-\nabla p_s+\beta\left(\vec{u}_g-\vec{u}_s\right)+\varepsilon_s\rho_s\vec{g} \tag{3.16}$$

To include the particle-particle interaction in the continuum approach, the Kinetic Theory of Granular Flow (KTGF) is used in the TFM. The KTGF expresses the isotropic and deviatoric parts of the solids stress tensor as function of the granular temperature, which is defined as

$$\theta=\frac{1}{3}\left\langle\vec{C}\cdot\vec{C}\right\rangle \tag{3.17}$$

Where $\vec{C}$ represents the particle fluctuation velocity, which is computed using a separate conservation equation, the so-called granular temperature equation

$$\frac{3}{2}\left[\frac{\partial\left(\varepsilon_s\rho_s\theta\right)}{\partial t}+\nabla\cdot\left(\varepsilon_s\rho_s\theta\vec{u}_s\right)\right]=-\left(p_s\bar{\bar{I}}+\varepsilon_s\bar{\bar{\tau}}_s\right):\nabla\vec{u}_s-\nabla\cdot\left(\varepsilon_s q_s\right)-3\beta\theta-\gamma \tag{3.18}$$

The constitutive equations used in the TFM, which were derived by Nieuwland et al. (1996), are listed in Table 3.2. The drag force suggested by van der Hoef et al. (2005) which was used in the DPM, was also used in the TFM, see section 3.2.

Table 3.2: Constitutive equations for TFM, after Nieuwland et al. (1996)

Particle pressure	$p_s = \left[1 + 2\left(1 + e_n\right)\varepsilon_s \mathrm{g}_0\right]\varepsilon_s \rho_s \theta$
Newtonian stress-tensor	$\bar{\bar{\tau}}_s = -\mu_s \left[\nabla \vec{u} + (\nabla \vec{u})^T - \frac{2}{3}\vec{I}(\nabla \vec{u})\right]$
Bulk viscosity	$\lambda_s = \frac{4}{3}\varepsilon_s \rho_s d_p \mathrm{g}_0 \left(1 + e_n\right)\sqrt{\frac{\theta}{\pi}}$
Shear viscosity	$\mu_s = 1.01600\frac{5}{96}\pi\rho_s d_p \sqrt{\frac{\theta}{\pi}}\frac{\left(1 + \frac{8}{5}\frac{(1+e_n)}{2}\varepsilon_s \mathrm{g}_0\right)\left(1 + \frac{8}{5}\varepsilon_s \mathrm{g}_0\right)}{\varepsilon_s \mathrm{g}_0} + \frac{4}{5}\varepsilon_s \rho_s d_p \mathrm{g}_0 \left(1 + e_n\right)\sqrt{\frac{\theta}{\pi}}$
Pseudo-Fourier fluctuating kinetic energy flux	$\vec{q}_s = -\kappa_s \nabla \theta$
Pseudo-thermal conductivity	$\kappa_s = 1.02513\frac{75}{384}\pi\rho_s d_p \sqrt{\frac{\theta}{\pi}}\frac{\left(1 + \frac{12}{5}\frac{(1+e_n)}{2}\varepsilon_s \mathrm{g}_0\right)\left(1 + \frac{12}{5}\varepsilon_s \mathrm{g}_0\right)}{\varepsilon_s \mathrm{g}_0} + 2\varepsilon_s \rho_s d_p \mathrm{g}_0 \left(1 + e_n\right)\sqrt{\frac{\theta}{\pi}}$
Dissipation of granular energy due to inelastic particle-particle collisions	$\gamma = 3\left(1 - e_n^2\right)\varepsilon_s^2 \rho_s \mathrm{g}_0 \theta \left[\frac{4}{d_p}\sqrt{\frac{\theta}{\pi}} - (\nabla \cdot \vec{u}_s)\right]$

3.3.1 Collisional parameters TFM

In the Kinetic Theory of Granular Flow the particle-particle dynamics are described by a single parameter collision model. The single parameter collision model calculates the impact velocity between particle a and particle b ($\bar{c}_{ab} = \bar{c}_a - \bar{c}_b$) to the rebound velocity $\left(\bar{c}'_{ab}\right)$ using the coefficient of restitution

$$\bar{c}'_{ab} \cdot \bar{k} = -e_n \left(\bar{c}_{ab} \cdot \bar{k}\right) \tag{3.19}$$

where $\bar{k}$ is the unit vector directed in the normal direction from the center of particle a to the center of particle b. In literature several authors (for example Jenkins and Zhang (2002) and Bokkers (2005)) have tried to combine the friction coefficient and the normal restitution coefficient in a single parameter, the so-called effective restitution coefficient e_{eff}. Bokkers (2005) estimated the effective restitution coefficient by

$$e_{eff} = e_n - \frac{\pi}{2}\mu_f + \frac{9}{2}\mu_f^2 \tag{3.20}$$

Bokkers (2005) found that due to the extra energy dissipation, the mixing of the particles was slightly decreased, however the particle mixing was still strongly over predicted. In addition, the effective restitution coefficient described the shape of the bubble slightly better. Another approach to describe the energy dissipation during the collisions is by including the frictional stresses, discussed in the next section.

3.3.2 Long term and multiple contact

In the KTGF, the collisions are assumed to be binary and quasi-instantaneous and do not account for long-term and multiple particle contacts which occur in the dense part of the fluidized bed. To account for the these long-term and multiple particle contacts, Savage (1998) suggested that the particulate phase stress tensor is the sum of the kinetic stress tensor and a frictional stress tensor, which have to be calculated separately. This leads to an additional term in the solids phase pressure and the solids phase viscosity.

$$p_s = p_{s,kc} + p_{s,f} \tag{3.21}$$

$$\mu_s = \mu_{s,kc} + \mu_{s,f} \tag{3.22}$$

Subscript kc stands for the kinetic and collisional part and f is the frictional part of the solids phase pressure and the solids phase viscosity. When the frictional part of the solids phase is equal to the critical pressure $p_c(\varepsilon_s)$, this yields (Johnson and Jackson (1987))

$$p_{s,f} = p_c(\varepsilon_s) = \begin{cases} F\dfrac{(\varepsilon_s - \varepsilon_{s,min})^r}{(\varepsilon_{s,min} - \varepsilon_s)^s} & \varepsilon_s > \varepsilon_{s,min} \\ 0 & \varepsilon_s < \varepsilon_{s,min} \end{cases}$$

The frictional stress tensor used in the TFM simulations was suggested by Srivastava and Sundaresan (2003) and is given by

$$\mu_{s,f} = \frac{p_c(\varepsilon_s)\ \sqrt{2}\sin\phi_I}{2\varepsilon_s\sqrt{\left(\overline{\overline{D}}_{i,j} : \overline{\overline{D}}_{i,j}\right) + \psi\theta_s/d_p^2}} \tag{3.23}$$

Where the rate of strain tensor, $\overline{\overline{D}}_{i,j}$, is given by:

$$\overline{\overline{D}}_{i,j} = \frac{1}{2}\left((\nabla\vec{u}_s) + (\nabla\vec{u}_s)^T\right) - \frac{1}{3}\nabla\cdot\vec{u}_s\bar{\bar{I}} \tag{3.24}$$

F, r, s and ψ are empirical constants and are assumed to be F = 0.05 $N.m^{-2}$, r = 2, s = 5, ψ = 1 and finally $e_{s,min}$ is assumed to be 0.5, after Johnson et al. (1990).

3.3.3 Numerical solution

To solve the volume-averaged Navier-Stokes equations in the DPM and in the TFM, the SIMPLE algorithm is used, however, to solve the particle volume fraction, taking into account the compressibility of the particle phase, an additional step is implemented in the TFM, see for more details Goldschmidt (2001). To evaluate the convective terms in the continuity and momentum equations, a second order accurate Barton

scheme is used, whereas the standard second order central discretization is used for the diffusive terms. A first order time integration is used in the DPM to solve the force balance for every individual particle in the fluidized bed and a soft-sphere collision model is used to compute the collisions between particles and between particles and the system wall.

3.3.4 Boundary conditions

The boundary conditions that are imposed on the walls utilize the matrix concept of Kuipers et al. (1993). In the DPM, the bottom cells are the influx cells; with the influx cells the DPM is able to introduce the gas into the system. The side walls of the column are represented as a no-slip boundary, whereas at the top of the column the gas leaves the column, therefore a prescribed pressure boundary is implemented at the top of the column. In the TFM the same boundary conditions are used for the gas phase, whereas for the particle phase, the partial slip boundary conditions were applied, following Sinclair and Jackson (1989):

$$\left(\bar{\bar{I}} - \overline{nn}\right) \cdot \varepsilon_s \bar{\bar{\tau}}_s \cdot \overline{n} = \frac{\alpha_{wall} \pi \varepsilon_s \rho_s g_0 \sqrt{\theta}}{2\sqrt{3}\varepsilon_0} \overline{u}_s \tag{3.25}$$

$$\varepsilon_s \overline{q}_s \cdot \overline{n} = -\overline{u}_s \cdot \varepsilon_s \bar{\bar{\tau}}_s \cdot \overline{n} + \frac{\sqrt{3}\pi \left(1 - e_{n,wall}^2\right) \varepsilon_s \rho_s g_0 \sqrt{\theta}}{4\varepsilon_0} \theta \tag{3.26}$$

In our simulations we have used 0.9 for the coefficient of restitution for particle-wall collisions, $e_{n,wall}$, and 0.5 for the specularity coefficient, α_s, after Pita and Sundaresan (1991).

3.3.5 Energy balance for the DPM and the TFM

To investigate the energy dissipation in the simulations, the mechanical energy balance is included in the CFD models. Following van der Hoef et al. (2006) the mechanical energy balance in the Discrete Particle Model is given by:

$$E_t = E_{pot} + E_{kin} + E_{rot} + E_{sn} + E_{st} + W_{dn} + W_{dt} + W_{df} - W_{drag} - W_{pres} \tag{3.27}$$

Where E_{pot}, E_{kin} and E_{rot} are respectively the potential, kinetic and rotational energy. E_{sn}, E_{st}, W_{dn}, W_{dt}, W_{df}, W_{drag} and W_{pres} are the potential energy of the normal spring, potential energy of the tangential spring, energy dissipated by the by the normal dashpot, energy dissipated by the tangential dashpot, the energy dissipated by the friction between the particles, the work performed by the drag on the particle and finally the work performed by the pressure on the particles. The different terms of the energy balance are described in Table 3.3.
The mechanical energy balance for the TFM was derived by Goldschmidt et al. (2004) for systems with non-moving walls and where the walls do not dissipate energy is given by

$$\frac{d}{dt}\left(E_{conv} + E_{gran} + E_{pot}\right) = W_{pres} + W_{drag} + W_{drag,gran} + W_{rest} \tag{3.28}$$

where E_{conv}, E_{gran} and E_{pot} are respectively the convection energy of the ensemble as a whole, the contribution due to random motion of particles within the ensemble and the potential energy in the system. Combined, the E_{conv} and E_{gran} yield the kinetic energy of the system. W_{pres}, W_{drag}, $W_{drag,gran}$ and W_{rest} represent the work performed by the pressure, the work performed by drag, the work performed by drag due to the granular temperature of the particles and the energy dissipated due to collisions. A description of the terms of the energy balance is given in Table 3.4.

The independent energy terms in the DPM are calculated every $8{\times}10^{-3}$ seconds and averaged over a time-span of 5 s. The different energy terms in TFM are calculated from the simulation output, then the different contributions are averaged over a time-span of 25 s.

3.3.6 Verification of the computational settings

As was discussed in section 3.2.3, in the DPM soft-sphere collision model it is important to use a spring stiffness in the normal direction which is large enough to describe the particle collisions correctly, however it should not be too large to yield a very small time-step to compute the contact force. To verify the normal spring stiffness, three independent DPM simulations have been performed with a normal spring stiffness of 750, 1500 and 3000 N.m^{-1}. In the simulations, the coefficients

Table 3.3: All contributions to the energy balance in the DPM

Term	**Equation**
Potential energy	$E_{pot} = \sum_{a}^{N_{part}} m_a \left(g \cdot h_a\right)$
Kinetic energy	$E_{kin} = \frac{1}{2} \sum_{a}^{N_{part}} m_a \left(\vec{v}_a \cdot \vec{v}_a\right)$
Rotational energy	$E_{rot} = \frac{1}{2} \sum_{a}^{N_{part}} I_a \left(\vec{\omega}_a \cdot \vec{\omega}_a\right)$
Potential energy of the normal spring†	$E_{sn} = \frac{1}{2} \sum_{a}^{N_{part}} \sum_{b} k_n \delta_{ab,n}^2$
Potential energy of the tangential spring†	$E_{st} = \frac{1}{2} \sum_{a}^{N_{part}} \sum_{b} k_t \left(\delta_{ab,n} \cdot \delta_{ab,n}\right)$
Work by drag	$W_{drag} = \int \sum_{a}^{N_{part}} \frac{\beta V_a}{(1-\varepsilon)} \left(\vec{u} - \vec{v}_a\right) \cdot \vec{v}_a dt$
Work by pressure	$W_{pres} = -\int \sum_{a}^{N_{part}} V_a \nabla p \cdot \vec{v}_a dt$
Energy dissipated by the normal dashpot†	$W_{dn} = \int \sum_{a}^{N_{part}} \sum_{b} \eta_n \left(\vec{v}_{ab,n} \cdot \vec{v}_{ab,n}\right) dt$
Energy dissipated by the tangential dashpot†	$W_{dt} = \int \sum_{a}^{N_{part}} \sum_{b} \eta_t \left(\vec{v}_{ab,t} \cdot \vec{v}_{ab,t}\right) dt$
Energy dissipated by the friction between the particles†	$W_{df} = \int \sum_{a}^{N_{part}} \sum_{b} \left(\mu_f \mid \vec{F}_{ab,n} \mid \vec{t}_{ab} \cdot \vec{v}_{ab,t}\right) dt$

† where $b > a$ and $b \in$ the contact list of a.

Table 3.4: All contributions to the energy balance in the TFM

Term	**Equation**
Kinetic energy	$E_{conv} = \sum_{k}^{N_{cell}} \frac{1}{2} \varepsilon_{s,k} \rho_s u_{s,k}^2 V_{cell,k}$
Random kinetic energy	$E_{gran} = \sum_{k}^{N_{cell}} \frac{3}{2} \varepsilon_{s,k} \rho_s \theta_k V_{cell,k}$
Potential Energy	$E_{pot} = \sum_{k}^{N_{cell}} \varepsilon_{s,k} \rho_s g_z h_k V_{cell,k}$
Dissipation due to restitution	$W_{rest} = -\sum_{k}^{N_{cell}} \gamma_k V_{cell,k}$
Work by drag	$W_{drag} = \sum_{k}^{N_{cell}} \beta_k \left(\vec{u}_{g,k} - \vec{u}_{s,k} \right) \cdot \vec{u}_{s,k} V_{cell,k}$
Work by drag gran	$W_{drag,gran} = -\sum_{k}^{N_{cell}} 3 \beta_k \theta_k V_{cell,k}$
Work by pressure	$W_{pres} = -\sum_{k}^{N_{cell}} \varepsilon_{s,k} \nabla p_{g,k} \cdot \vec{u}_{s,k} V_{cell,k}$

of restitution were set to 0.8 and 0.6 for respectively the normal and tangential direction. The friction coefficient was set to 0.1. All other settings are given in Table 3.5. The simulations were conducted parallel on 3 processors (AMD Opteron 1.8GHz dualcore processor). The computational time was respectively 109, 169 and 260 hours for a spring stiffness of 750, 1500 and 3000 N.m^{-1}. In Figure 3.2a and 3.2b the time-averaged axial emulsion phase velocity are presented at 0.050 and 0.075 m above the distributor. From these figures it can be concluded that the used normal spring stiffness was large enough to calculate the contact force correctly. In addition, the average bed height for all three simulations was approximately 0.11 m. In Figure 3.2c and 3.2d the influence of the number of grid cells on the time-averaged axial emulsion phase velocity is presented. The number of grid cells was varied between 25×1×75, 50×1×150 and 75×1×225. In this work 50×1×150 grid cells

was considered sufficient. Finally, in Figure 3.2e and 3.2f the influence of the time-step for the flow-solver is presented. This time-step has been varied between 2.0×10^{-4}, 1.0×10^{-4} and 1.0×10^{-5} s. It can be concluded that a flow-solver time step of 1×10^{-4} yields a time-step independent solution and therefore will be used in the simulations which are performed in the remainder of this chapter.

To investigate the influence of the grid size on the TFM simulations, several simulations of an 0.15 m width and 0.30 m height fluidized bed, with a packed bed height of 0.15 m, have been performed. The time step used in the TFM simulations was 1×10^{-5} s. For a summary of all computational settings, see Table 3.5. In Figure 3.3a and 3.3b the influence of the number of grid cells on the time-averaged emulsion phase velocity in a TFM simulation is shown. In the two simulations, only the number of grid cells has been varied from 60×1×120 grid to 90×1×180 grid, while keeping the other parameters of the simulation the same. From this figure it can be concluded that a grid of 60×1×120 produces (nearly) grid independent solutions.

To verify if the simulated time was sufficiently long, the results of a DPM and TFM simulation have been averaged over different time-spans, 1-30, 5-30 and 10-30 s. The collisional properties of the DPM simulation were e_n = 0.97, e_t = 0.6, μ_f = 0.1. The coefficient of restitution in the normal direction in the TFM simulation was set to e_n = 0.97. The other settings used in the simulations are given in Table 3.5. It can be seen from Figure 3.4 that the simulation time for all three cases was sufficiently long, i.e. the results show no significant differences in time-averaged axial particle velocity for both models. In addition, the fluidized bed has operated sufficiently long to exclude start-up effects.

3.4 Results

In this section the results of the simulations will be presented. First, the minimum fluidization velocity of the particles will be determined with the DPM and the TFM and compared with experimental findings. A correct prediction of the minimum fluidization velocity is required for an accurate setting of the excess velocity. Subsequently, the influence of

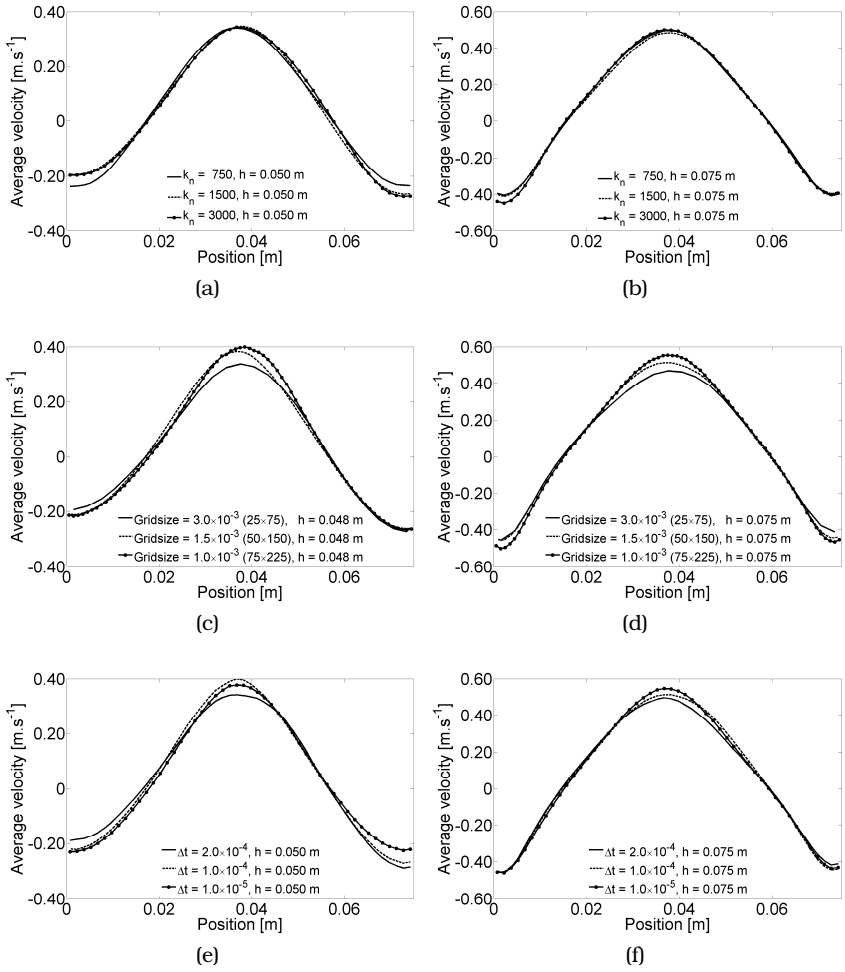

Figure 3.2: Influence of spring stiffness (750,1500,3000 $N.m^{-1}$), grid size and time-step (2×10^{-4}, 1×10^{-4} and 1×10^{-5} s) on the time-averaged axial solids phase velocity. (a) influence of the spring stiffness at 0.05 m above the distributor; (b) influence of the spring stiffness at 0.075 m above the distributor; (c) influence of the grid size at 0.05 m above the distributor; (d) influence of the grid size at 0.75 m above the distributor; (e) influence of the time-step at 0.05 m above the distributor (f) influence of the time-step at 0.075 m above the distributor.

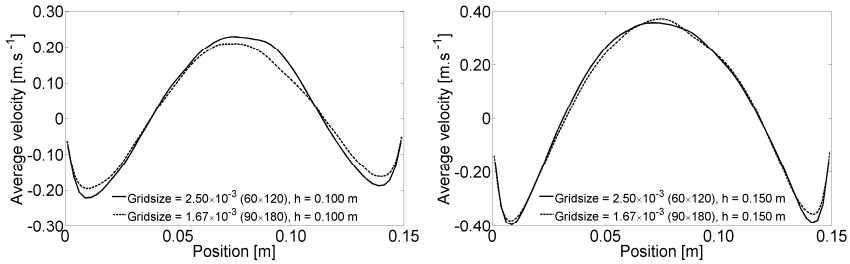

Figure 3.3: Influence of grid size on the time-averaged axial solids phase velocity, (a) influence of the grid size at 0.10 m above the distributor; (b) influence of grid size at 0.15 m above the distributor.

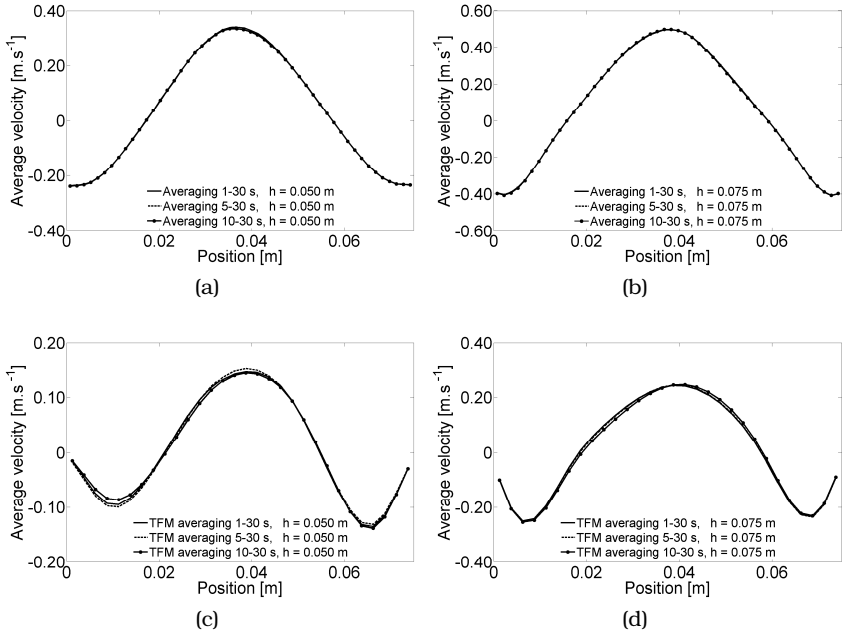

Figure 3.4: Influence of averaging time on the time-averaged axial solids phase velocity during the DPM and TFM simulations, (a) DPM; height is 0.05 m; (b) DPM; height is 0.075 m; (c) TFM; height is 0.05 m; (d) TFM; height is 0.075 m.

the microscopic particle properties on the hydrodynamics in a bubbling fluidized bed will be investigated on basis of DPM and TFM simulations. Finally, DPM and TFM results will be compared with the experimental data, reported in chapter 2.

3.4.1 Determination of the minimum fluidization velocity

To compare the experimental results obtained in chapter 2 with the simulations performed in this chapter, the minimum fluidization velocity of the glass beads has been determined by the pressure drop versus velocity method, see for example Kunii and Levenspiel (1991). To determine the minimum fluidization velocity in the simulations the following steps were performed: at the start of the simulation, the bed was fluidized at approximately 2.5 u_0/u_{mf} for 1 s, subsequently the gas supply in the simulation was switched off, leading to the formation of a packed bed state. Finally, the superficial gas flow was slowly increased again, up to approximately 2.5 u_0/u_{mf}.

In Figure 3.5 the results of the simulations are compared with the experimental minimum fluidization velocity for both the DPM (Figure 3.5a) and the TFM (Figure 3.5b). In Figure 3.5d, the pressure drop over the fluidized bed is normalized by dividing the pressure drop by the final pressure drop.

The pressure drop over the 'packed bed' in the TFM simulations is a slightly curved line instead of a straight line, see Figure 3.5b. The TFM accounts only for energy dissipation in the normal direction, and not for energy dissipation in the tangential direction or by friction between the particles. To investigate the influence of the energy dissipation due to friction, two DPM simulation were performed in which the coefficient of restitution in the tangential was set to zero and the friction coefficient was set to 0.1 and 0, see Figure 3.5a. Although the collisional properties of the particles are not responsible for the curved TFM pressure drop line, the coefficient of restitution in the tangential direction has a small influence on the minimum fluidization velocity whereas the friction coefficient has a large influence on the minimum fluidization velocity. In the case without friction, the particles loose no energy due to friction if they

collide with each other. The curved pressure drop line could be caused by the averaging of the porosity in the z-direction, therefore the number of grid cells in the z-direction was increased. The number of grid cells in the z-direction has been increased two and four times. It can be seen in Figure 3.5b that the number of grid cells has no influence on the results. This should also be expected because the TFM results were grid independent. Finally, the porosity gradient over the fluidized bed in the TFM simulation was investigated. The results are presented in Figure 3.5c. It can be seen that when the superficial gas velocity is increased, the porosity over the fluidized bed in the radial direction of the fluidized bed decreases, and that the bed becomes slightly expanded even though the superficial gas velocity is still below the minimum fluidization velocity. The influence of the superficial gas velocity on the porosity causes the observed slightly non-linear pressure drop versus superficial velocity curve.

The pressure drop over the 'packed bed' versus superficial velocity obtained from the DPM simulations also exhibits a slightly non-linear trend, see Figure 3.5b. As already discussed, the collisional properties have no influence on the pressure drop over the packed bed at various superficial gas velocities. Next, the spring constant in the normal direction, k_n was increased. The reasoning was that if the spring constant is increased, the overlap between the particles is decreased. However, the spring constant in the normal direction has almost no influence on the pressure drop over the packed bed at various superficial gas velocities.

In Figure 3.5d the experimentally determined pressure drop vs. the superficial gas velocity is compared with the results of the DPM and the TFM. It can be seen that the DPM and the TFM results are comparable which should be the case provided that in both models the same drag relation has been used. The difference between the computational results and the experimental results can have several reasons, such as the particle size distribution in the experiment or a different porosity in the packed bed due to the sphericity of the particles (in the simulations assumed to be 1). In addition, there can be a small deviation in the measured mean particle diameter that was used in the simulations.

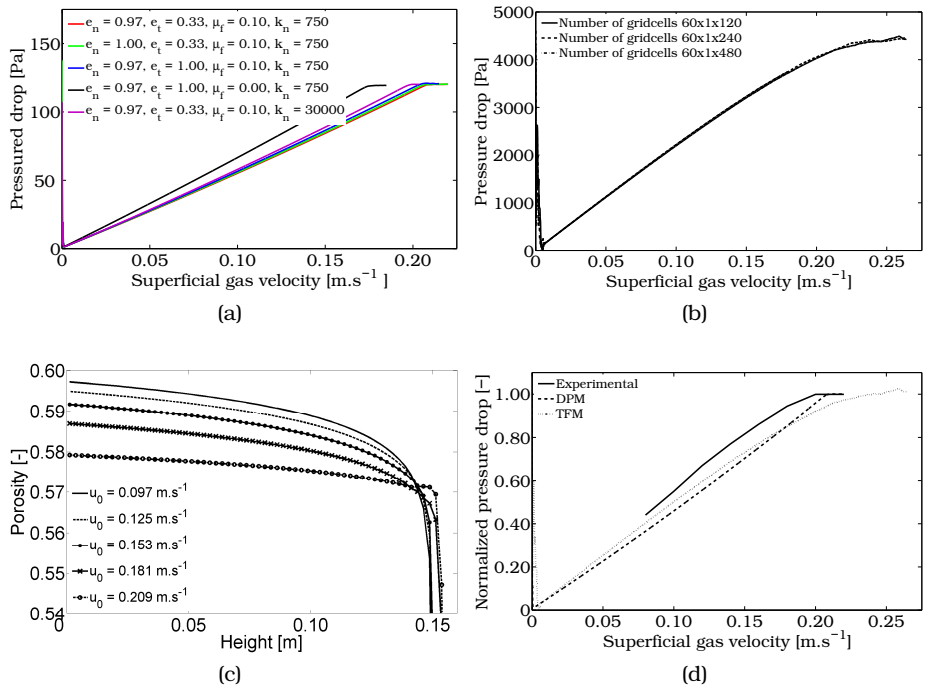

Figure 3.5: Determination of the minimum fluidization velocity using the pressure drop method, for the DPM, TFM and the experimental: (a) pressure drop vs. superficial gas velocity using the DPM; (b) pressure drop vs. superficial gas velocity using the TFM; (c) porosity vs. height in TFM simulation at various superficial gas velocities; (d) comparison of the pressure drop vs. superficial gas velocity for the simulations and the experiment.

The minimum fluidization velocity for glass beads with a diameter of 0.485 mm is determined to be 0.21 $m.s^{-1}$, and the polymer particles with a diameter of 1.03 mm possess a minimum fluidization velocity of 0.26 $m.s^{-1}$ (not shown here).

3.4.2 Influence of the microscopic particle properties

To investigate the impact of microscopic particle properties on the macroscopic circulation patterns and the bubble properties, several DPM and TFM simulations were conducted. The properties which were investigated using the DPM are the collision parameters and the particle density. For the TFM, the influence of the normal restitution on the macroscopic particle circulation and the bubble properties has been investigated. A overview of the settings used in the simulations is given in Table 3.5.

Table 3.5: Settings for DPM and TFM simulations for the investigation of the impact of the microscopic particle properties on the hydrodynamics in a bubbling fluidized bed.

Parameter	**DPM**	**TFM**
Width x-direction [m]	0.075	0.075
Depth y-direction [m]	0.00628	0.0025
Height z-direction [m]	0.225	0.225
Grid cells (x,y,z)	50,1,150	30,1,90
Packed bed height [m]	0.075	0.075
# of particles [-]	~36,500	-
Particle diameter [mm]	1.03	1.03
Particle density [$kg.m^{-3}$]	~800	~800
Minimum fluidization velocity [$m.s^{-1}$]	0.26	-
Superficial gas velocity [$m.s^{-1}$]	0.66	0.66
Normal restitution coefficient [-]	0.65-1.00	0.90-1.00
Tangential restitution coefficient [-]	0.60-0.00	-
Normal spring stiffness [$N.m^{-1}$]	750	-
Frictional coefficient [-]	0.00-0.10	-
Time step [s]	1×10^{-4}	1×10^{-5}
Simulation time [s]	30	30

Influence of the collisional properties

First the influence of the collisional properties was investigated by varying the parameter values between those for ideal particles and glass beads (keeping the particle density constant).

Table 3.6: Range of values for the collisional properties in the DPM simulations.

e_n	0.97, 1.0	μ_f	0.10, 0.00
e_t	0.60, 1.0	u_0	0.66 $m.s^{-1}$

The influence of the collisional properties on the macroscopic circulation patterns computed with the DPM is depicted in Figure 3.6. From the figure it is evident that the collisional properties have a large influence on the time-averaged particle velocity in the DPM simulations. In all simulations, with the exception of the simulation without energy dissipation due to collisions (e_n = e_t = 1.0 and μ_f = 0.0), the particles ascend in the center of the bed and descend near the walls in agreement with the experiments reported in chapter 2. One large circulation cell can be seen if no energy dissipated due to particle collisions. To quantify the time-averaged axial solids velocity, the lateral profiles at two different heights above the distributor are given in Figure 3.7. It can be concluded from this figure that the coefficient of restitution in the tangential and the normal direction have a minor influence on the time-averaged axial solids velocity. Furthermore, it can be concluded that the coefficient of friction has the largest influence on the time-averaged axial emulsion phase velocity. When no energy is dissipated during the collision of particles, pronounced solids motion is absent. It appears that when the friction coefficient is set to zero, the influence of the coefficient of restitution in the normal direction is larger than when the friction coefficient is included in the simulations.

In Figure 3.8 the influence of the collision parameters on the bubble properties is presented. From the different graphs in Figure 3.8 it can be seen that the coefficients of restitution in the normal and tangential direction have little influence on the bubble properties. However in the two simulations in which the friction coefficient was set to zero, the equivalent bubble diameter decreases significantly. In addition, the number of bubbles also decreases in these two simulations. This results in a lower visual bubble flow as can be seen in Figure 3.8e. Finally, the

collision properties have almost no influence on the bubble rise velocity as a function of the equivalent bubble diameter.

In Table 3.7 the energy balance is presented. It can be seen that the friction coefficient has the largest influence on the kinetic, rotational and potential energy. The coefficient of restitution in the normal or tangential direction have hardly any influence on the kinetic, rotational and potential energy. Furthermore it can be seen that the energy dissipated by the tangential dashpot is two orders of magnitude smaller than the energy dissipated by the normal dashpot and the energy dissipated by friction between the particles.

It can be concluded that bubbles are mainly formed due to the fact that particles dissipate energy during the collisions. Most of the energy is dissipated by the friction between the particles and the energy dissipated by the normal dashpot. The influence of the coefficient of restitution in the normal direction and the friction coefficient on the different terms in the energy balance will be presented in the next sections in more detail.

Table 3.7: Influence of collisional properties on the energy levels, where the work terms have been time-averaged over a time span 10-15 s.

Case	E_{kin} $[J]$	E_{rot} $[J]$	E_{pot} $[J]$	W_{drag} $[J.s^{-1}]$	W_{pres} $[J.s^{-1}]$
0.97, 0.6, 0.1	6.543×10^{-4}	6.929×10^{-6}	-8.463×10^{-3}	2.659×10^{-3}	2.631×10^{-3}
0.97, 1.0, 0.1	6.634×10^{-4}	6.933×10^{-6}	-8.463×10^{-3}	2.560×10^{-3}	2.485×10^{-3}
0.97, 1.0, 0.0	3.169×10^{-4}	2.509×10^{-9}	-8.316×10^{-3}	3.462×10^{-4}	6.031×10^{-4}
1.00, 1.0, 0.1	6.051×10^{-4}	7.566×10^{-6}	-8.398×10^{-3}	2.385×10^{-3}	2.221×10^{-2}
1.00, 1.0, 0.0	1.630×10^{-4}	2.509×10^{-9}	-8.243×10^{-3}	-1.538×10^{-4}	2.009×10^{-4}
e_n, e_t, μ_f	E_{sn} $[J]$	E_{st} $[J]$	W_{dn} $[J.s^{-1}]$	W_{dt} $[J.s^{-1}]$	W_{df} $[J.s^{-1}]$
0.97, 0.6, 0.1	6.829×10^{-6}	1.527×10^{-8}	1.105×10^{-3}	3.188×10^{-5}	6.315×10^{-3}
0.97, 1.0, 0.1	5.538×10^{-6}	1.475×10^{-8}	1.071×10^{-3}	0	6.030×10^{-3}
0.97, 1.0, 0.0	8.006×10^{-6}	0	1.328×10^{-3}	0	0
1.00, 1.0, 0.1	1.069×10^{-5}	1.687×10^{-8}	0	0	6.441×10^{-3}
1.00, 1.0, 0.0	8.358×10^{-6}	0	0	0	0

Influence of the coefficient of restitution in the normal direction

The influence of the coefficient of restitution in the normal direction was investigated by conducting several DPM simulations in which the

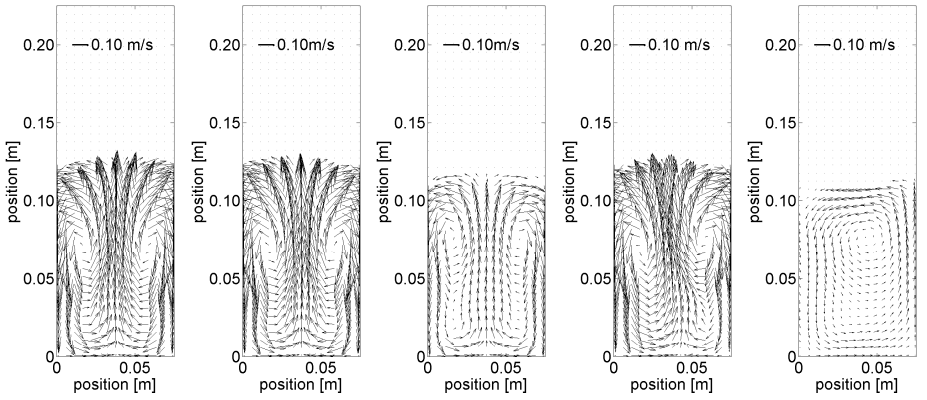

Figure 3.6: Influence of the collision properties on the time-averaged particle velocity of the DPM simulations. Superficial gas velocity: 2.5 u_0/u_{mf}, number of particles was ~36,500 particles, and packed bed aspect ratio of 1, (a) e_n = 0.97, e_t = 0.6, μ_f = 0.1; (b) e_n = 0.97, e_t = 1.0, μ_f = 0.1; (c) e_n = 0.97, e_t = 1.0, μ_f = 0.0; (d) e_n = 1.00, e_t = 1.0, μ_f = 0.1; (e) e_n = 1.00, e_t = 1.0, μ_f = 0.0.

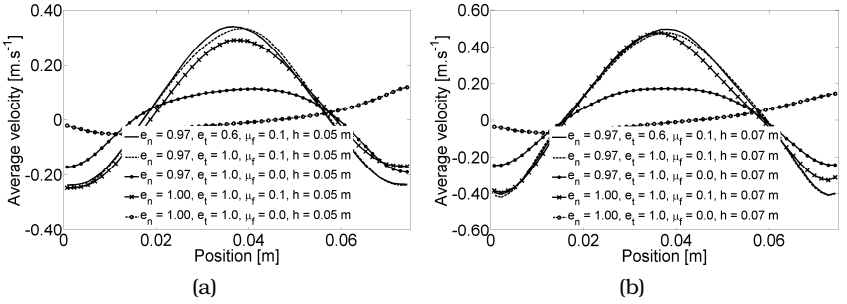

Figure 3.7: Influence of the collision properties on the time-averaged axial solids velocity. Superficial gas velocity: 2.5 u_0/u_{mf}, number of particles was ~36,500 particles, and packed bed aspect ratio of 1. (a) h = 0.05 m; (b) h = 0.075 m.

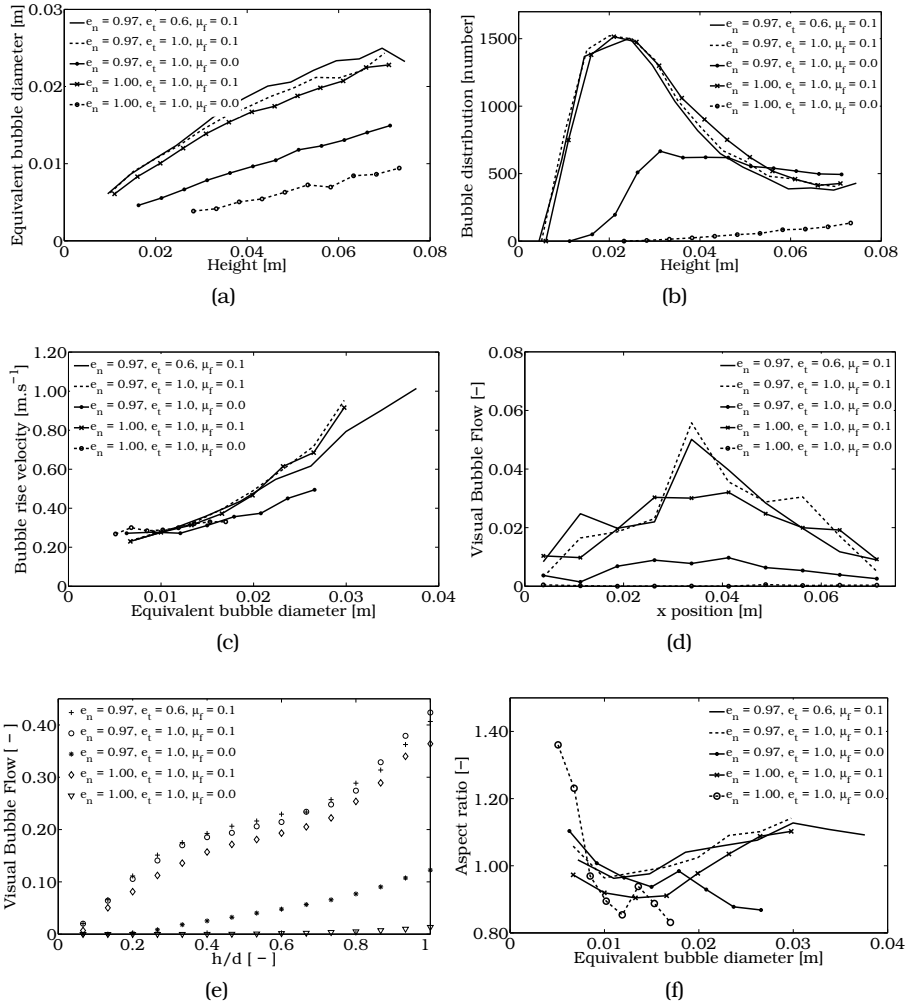

Figure 3.8: Influence of the collision parameters on the time-averaged bubble properties, (a) Equivalent bubble diameter vs. height above the distributor; (b) Number of bubbles vs. height above the distributor; (c) Averaged bubble rise velocity vs. equivalent bubble diameter; (d) Indicative axial visual bubble flow vs height above the distributor at 0.05 m above the distributor; (e) Visual bubble flow vs. height above the distributor; (f) Bubble aspect ratio vs. equivalent bubble diameter.

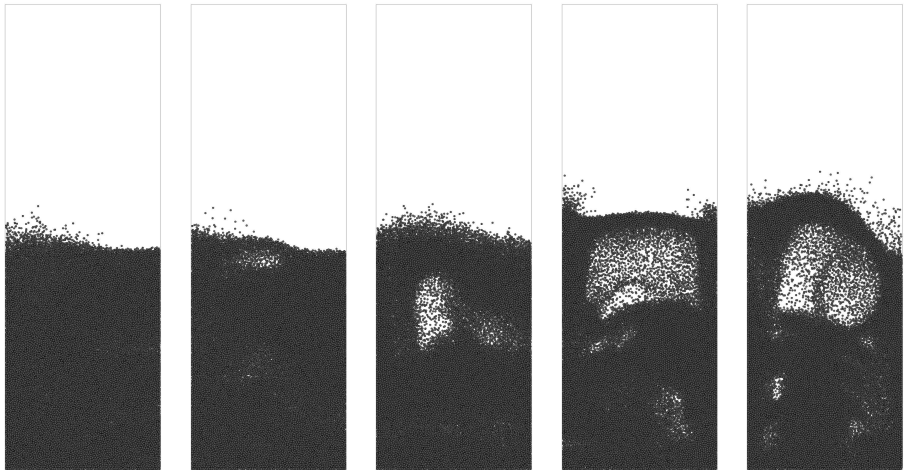

(a) (b) (c) (d) (e)

Figure 3.9: Influence of the coefficient of restitution in the normal direction, snapshots of the DPM simulations at t = 10.0 s. Superficial gas velocity: 2.5 u_0/u_{mf}, number of particles was ~36,500 particles, and packed bed aspect ratio of 1. (a) e_n = 1.00; (b) e_n = 0.99; (c) e_n = 0.97; (d) e_n = 0.94; (e) e_n = 0.90.

coefficient of restitution in the normal direction was varied between 0.90 and 1.00. The collision properties and the superficial gas velocity are given in Table 3.8. In Figure 3.9 snapshots of the DPM simulation are presented. It can be seen from Figure 3.9 that when the coefficient of restitution is increased the formation of bubbles is decreased.

Table 3.8: Settings for DPM simulations

e_n	0.90, 0.94, 0.97, 0.99, 1.00	μ_f	0.00
e_t	1.0	u_0	0.66 $m.s^{-1}$

The time-averaged axial emulsion phase velocity profiles are given in Figure 3.10. For a coefficient of restitution in the normal direction up to 0.97, two symmetrical vortices appear in the bed. However, when the coefficient of restitution is increased further, these vortices disappear

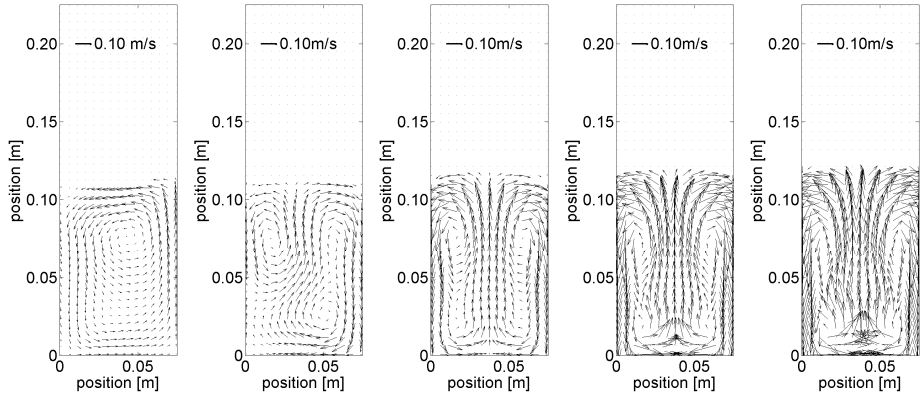

Figure 3.10: Influence of the coefficient of restitution in the normal direction on the time-averaged particle velocity of the DPM simulations. Superficial gas velocity: 2.5 u_0/u_{mf}, number of particles was ~36,500 particles, and packed bed aspect ratio of 1, (a) e_n = 1.00; (b) e_n = 0.99; (c) e_n = 0.97; (d) e_n = 0.94; (e) e_n = 0.90.

and one large circulation cell (roll) appears. Although there are almost no bubbles in case of e_n = 1.0, the particles are not stationary. The direction of the roll probably depends on the starting conditions of the fluidized bed.

In Figure 3.11 the influence of the coefficient of restitution in the normal direction on the time-averaged axial solids velocity at 0.05 and 0.075 m above the distributor are given. It can be seen that both the (absolute) velocity of the ascending (center) and descending particles (wall) increases with decreasing coefficient of restitution in the normal direction. In addition, it also appears that the transition from positive to negative particle velocity is occurring at approximately the same position in the fluidized bed. Furthermore, from Figure 3.11a it can be seen that with a coefficient of restitution in the normal direction of 0.90 and 0.94 two peaks are visible. This suggests that the bubbles which are formed in the bottom corners of the fluidized bed have not yet reached each other at 0.05 m above the distributor.

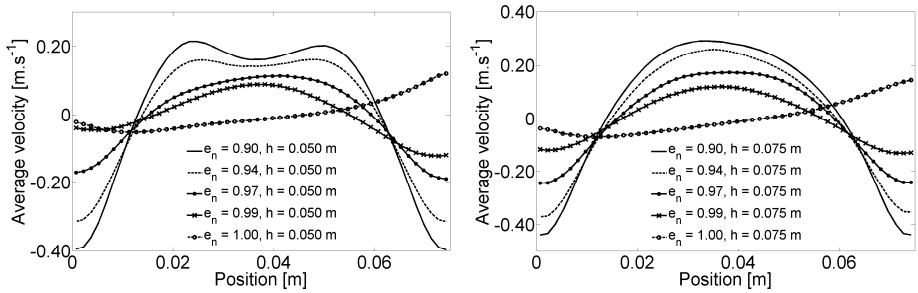

Figure 3.11: Influence of the coefficient of restitution in the normal direction on the time-averaged axial solids velocity. Superficial gas velocity: 2.5 u_0/u_{mf}, number of particles was ~36,500 particles, and packed bed aspect ratio of 1. (a) h = 0.05 m; (b) h = 0.075 m.

The influence of the coefficient of restitution in the normal direction on the bubble properties is presented in Figure 3.12. As could be seen in the snapshots of the simulations, the averaged bubble diameter as function of the height in the fluidized bed obtained form the simulations reduces, when the coefficient of restitution in the normal direction is increased, see Figure 3.12a. In Figure 3.12c the bubble rise velocity is presented as function of the equivalent bubble diameter. It can be seen that the bubble rise velocity is the same up to a bubble diameter of 0.015 m. The bubbles in the simulation with a lower coefficient of restitution rise faster through the fluidized bed. This is due to the fact that larger bubbles appear higher in the fluidized bed, where the velocity of the particles is higher as well. The visual bubble flow rate as function of the normalized height in the fluidized bed is given in Figure 3.12e. In can be seen that the visual bubble flow rate increases with a decrease in coefficient of restitution. This means that when the coefficient of restitution is increased, more gas is moving through the emulsion phase. Finally, the influence of the coefficient of restitution in the normal direction on the bubble aspect ratio is presented. It can be seen that when the coefficient of restitution decreases, the bubbles become more elongated, i.e. the ratio between the vertical size of the bubble and the

horizontal size becomes larger. This would also explain that the bubble which are formed in the bottom corners of the fluidized bed have not reached each other in Figure 3.11a, resulting in two distinct peaks in the time-averaged lateral solids velocity profiles.

In Table 3.9 the influence of the coefficient of restitution in the normal direction on the contributions to the energy balance is presented. It can be seen that almost all energy contributions decrease in magnitude when the coefficient of restitution in the normal direction increases. The energy dissipated due to the normal dashpot decreases linearly with increasing coefficient of restitution. The rotational energy and the potential energy of the spring in the normal direction remain at the same level.

Table 3.9: Influence of coefficient of restitution in the normal direction on the contributions to the energy balance, where the work terms have been time-averaged over a time span 10-15 s.

Case	E_{kin} $[J]$	E_{rot} $[J]$	E_{pot} $[J]$	W_{drag} $[J.s^{-1}]$	W_{pres} $[J.s^{-1}]$
e_n = 0.90	6.611×10^{-4}	2.509×10^{-9}	-8.343×10^{-3}	1.276×10^{-3}	1.631×10^{-3}
e_n = 0.94	4.612×10^{-4}	2.509×10^{-9}	-8.372×10^{-3}	7.530×10^{-4}	1.030×10^{-3}
e_n = 0.97	3.169×10^{-4}	2.509×10^{-9}	-8.316×10^{-3}	3.462×10^{-4}	6.031×10^{-4}
e_n = 0.99	1.999×10^{-4}	2.509×10^{-9}	-8.300×10^{-3}	7.660×10^{-6}	3.679×10^{-4}
e_n = 1.00	1.360×10^{-4}	2.509×10^{-9}	-8.243×10^{-3}	-1.538×10^{-4}	2.009×10^{-4}

Case	E_{sn} $[J]$	E_{st} $[J]$	W_{dn} $[J.s^{-1}]$	W_{dt} $[J.s^{-1}]$	W_{df} $[J.s^{-1}]$
e_n = 0.90	8.766×10^{-6}	0	4.301×10^{-3}	0	0
e_n = 0.94	1.006×10^{-5}	0	2.649×10^{-3}	0	0
e_n = 0.97	8.006×10^{-6}	0	1.328×10^{-3}	0	0
e_n = 0.99	7.758×10^{-6}	0	4.920×10^{-4}	0	0
e_n = 1.00	8.358×10^{-6}	0	0	0	0

Influence of the coefficient of friction

The influence of the friction coefficient was investigated by conducting DPM simulations in which the friction coefficient was varied between 0.00 and 0.10. The coefficient of restitution in the normal and tangential direction were set to 1.00. In Figure 3.13 snapshots of DPM simulations using different values for the friction coefficient are presented. The

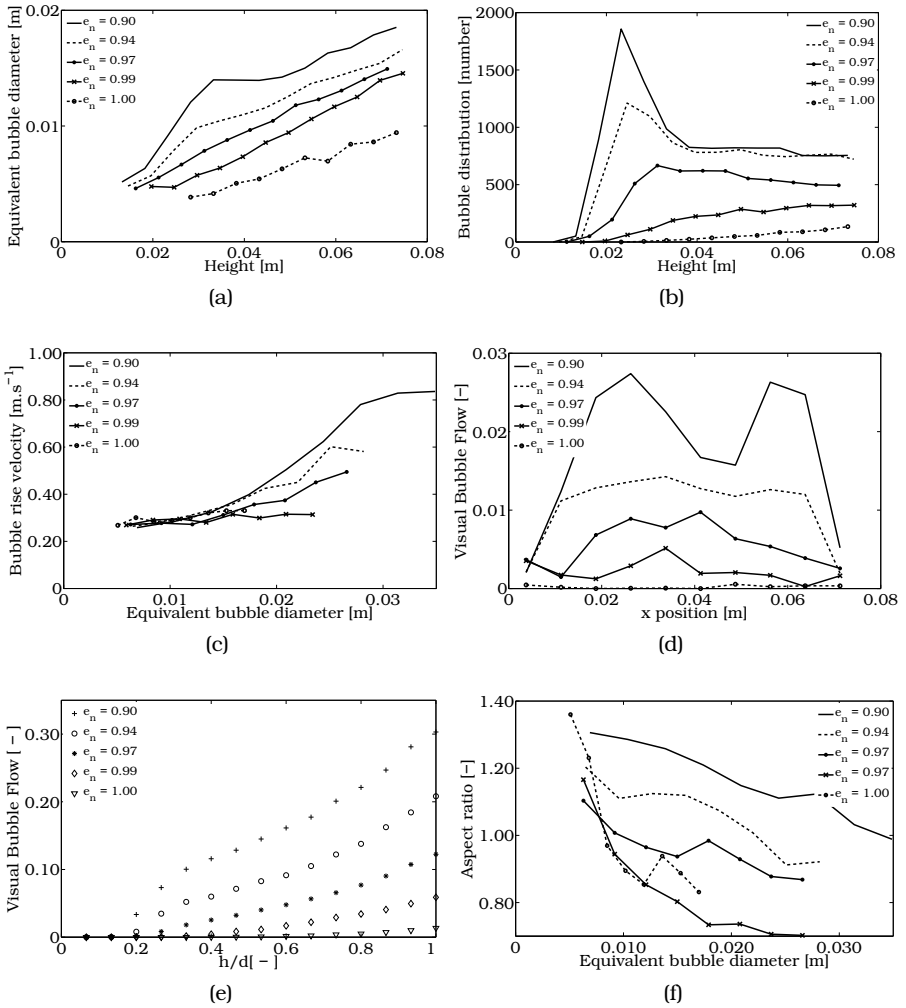

Figure 3.12: Influence of the normal coefficient of restitution on the time-averaged bubble properties, (a) Equivalent bubble diameter vs. height above the distributor; (b) Number of bubbles vs. height above the distributor; (c) Averaged bubble rise velocity vs. equivalent bubble diameter; (d) Indicative axial visual bubble flow vs height above the distributor at 0.05 m above the distributor; (e) Visual bubble flow vs. height above the distributor; (f) Bubble aspect ratio vs. equivalent bubble diameter.

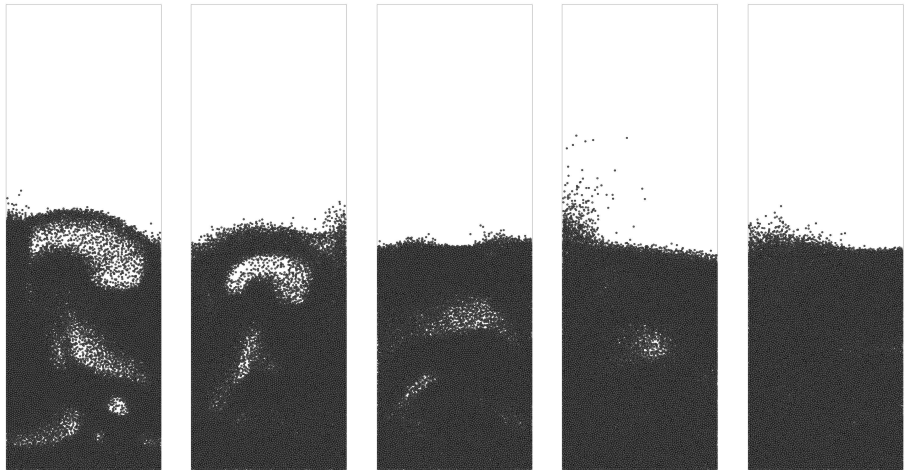

(a) (b) (c) (d) (e)

Figure 3.13: Influence of the friction coefficient, snapshots of the DPM simulations at t = 10.0 s. Superficial gas velocity: 2.5 u_0/u_{mf}, number of particles ~36,500 particles, and the packed bed aspect ratio of 1. (a) μ_f = 0.10;(b) μ_f = 0.06; (c) μ_f = 0.03; (d) μ_f = 0.01; (e) μ_f = 0.00.

figure shows that if the friction coefficient is increased, larger bubbles appear and the bed is fluidizing more vigorously.

Table 3.10: Settings for DPM simulations

e_n	1.0	μ_f	0.0, 0.01, 0.03, 0.06, 0.10
e_t	1.0	u_0	0.66 $m.s^{-1}$

This can also be discerned from Figure 3.14, where the time-averaged axial solids velocity as function of the friction coefficient is shown. In this figure, the friction coefficient increases from left to right. When the friction coefficient is increased from 0.00 to 0.01, two symmetrical vortices appear, which stretch from the top to the bottom of the fluidized bed. The vortices become stronger when the friction coefficient is increased, however, the shape of the vortices does not change anymore.

Lateral profiles of the time-averaged axial solids velocity at 0.05 and

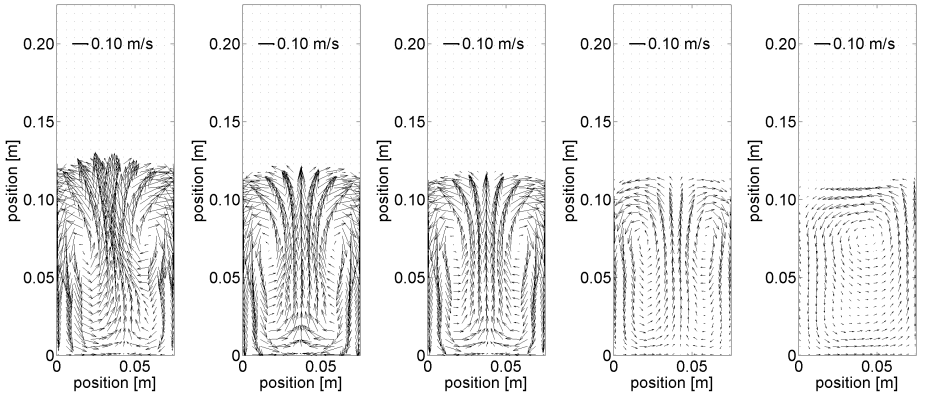

Figure 3.14: Influence of the friction coefficient on the time-averaged particle velocity of the DPM simulations. Superficial gas velocity: 2.5 u_0/u_{mf}, number of particles ~36,500 particles, and packed bed aspect ratio of 1. The time-averaged particle velocity of the DPM simulations. (a) μ_f = 0.0; (b) μ_f = 0.01; (c) μ_f = 0.03; (d) μ_f = 0.06; (e) μ_f = 0.10.

0.075 m above above the distributor are displayed in Figure 3.15. Similar to results obtained for the variation of the coefficient of restitution in the normal direction, the transition from a descending particle velocity to an ascending particle velocity occurred at approximately the same position in the fluidized bed. In addition, it can be seen that the maximum and minimum particle velocity prevails at the maximum value of the friction coefficient. Furthermore, when Figures 3.11 and 3.15 are compared, the maximum time-averaged axial emulsion velocity is approximately 1.5 times larger for the simulations with particle friction included. Also the shape at 0.05 m above the distributor is different, the bubble plumes have reached each other, yielding a single maximum time-averaged axial solids velocity.

The influence of the friction coefficient on the bubble properties is presented in Figure 3.16. In Figure 3.16a the equivalent bubble diameter is presented as function of the height in the fluidized bed. It can be seen that the equivalent bubble diameter increases when the friction

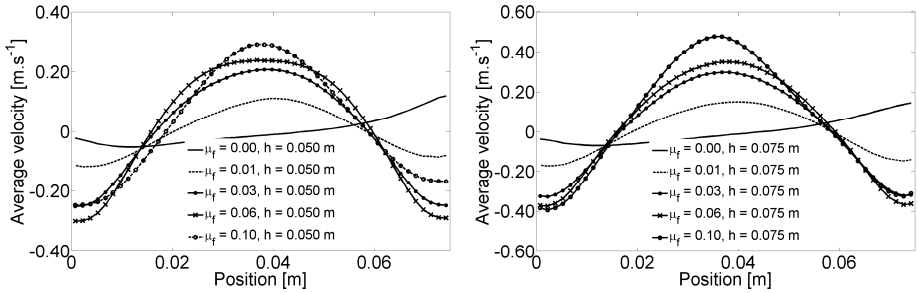

Figure 3.15: Influence of the friction coefficient on the time-averaged axial solids velocity at different positions above the distributor. Superficial gas velocity: 2.5 u_0/u_{mf}, number of particles ~36,500 particles, and packed bed aspect ratio of 1. (a) h = 0.05 m; (b) h = 0.075 m.

coefficient is increased. The dependence of the equivalent bubble size on the friction coefficient is even larger than the dependence of the bubble size on the coefficient of normal restitution. Figure 3.16c shows the bubble rise velocity as function of the bubble diameter. The bubble rise velocity as a function of the equivalent bubble diameter is not sensitive to the coefficient of friction. The number of bubbles which are present in the fluidized bed is larger when the friction coefficient is increased. The visual bubble flow rate is presented in Figure 3.16e as function of the normalized bed height. This figure shows that the visual bubble flow rate increases when the friction coefficient is increased.

In Table 3.11 the influence of the friction coefficient on the contributions to the energy balance is presented. It can be seen that almost all terms in the energy balance increase when the friction coefficient is increased. When the energy dissipated by the friction is compared to the energy dissipated by the normal dashpot (see Table 3.9), it can be seen that approximately 1.5 times as much energy is dissipated due to friction.

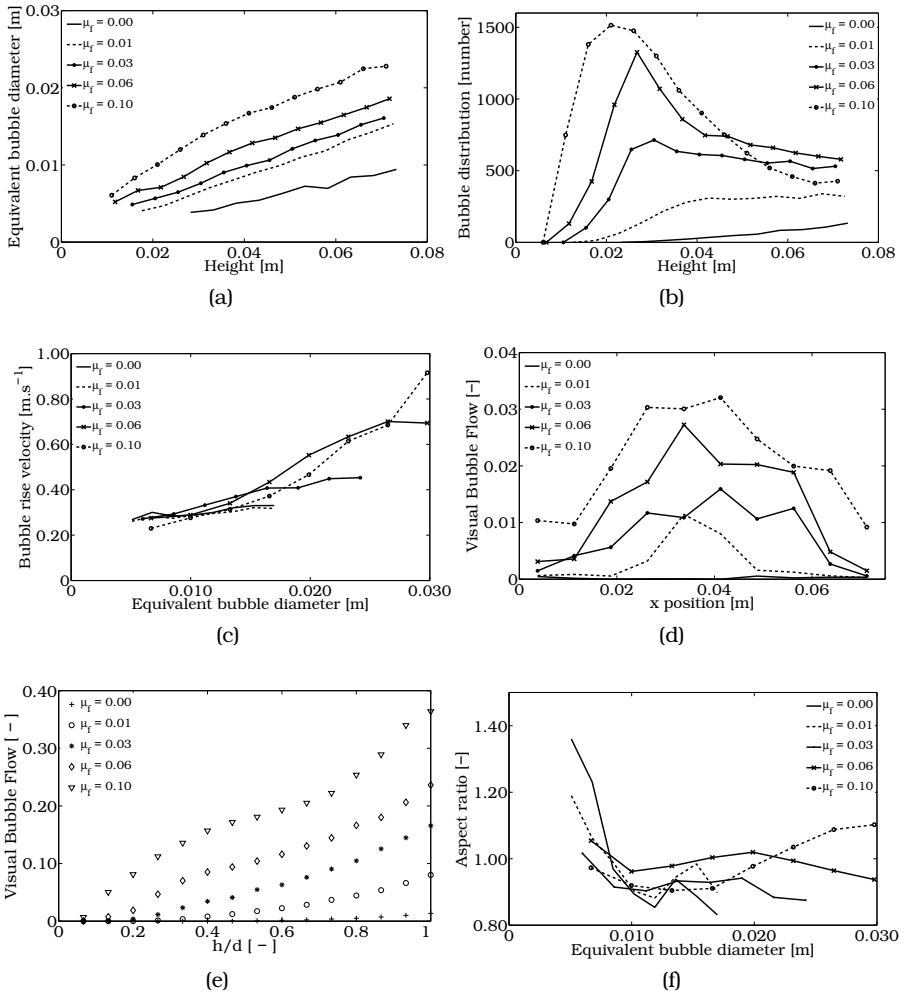

Figure 3.16: Influence of the friction coefficient on the time-averaged bubble properties, (a) Equivalent bubble diameter vs. height above the distributor; (b) Number of bubbles vs. height above the distributor; (c) Averaged bubble rise velocity vs. equivalent bubble diameter; (d) Indicative axial visual bubble flow vs height above the distributor at 0.05 m above the distributor; (e) Visual bubble flow vs. height above the distributor; (f) Bubble aspect ratio vs. equivalent bubble diameter.

Table 3.11: Influence of friction coefficient on the energy levels, where the work terms have been time-averaged over a time span 10-15 s.

Case	E_{kin} $[J]$	E_{rot} $[J]$	E_{pot} $[J]$	W_{drag} $[J.s^{-1}]$	W_{pres} $[J.s^{-1}]$
μ_f = 0.00	1.360×10^{-4}	2.509×10^{-9}	-8.243×10^{-3}	-1.538×10^{-4}	2.009×10^{-4}
μ_f = 0.01	2.410×10^{-4}	1.658×10^{-6}	-8.333×10^{-3}	1.381×10^{-4}	5.412×10^{-4}
μ_f = 0.03	3.660×10^{-4}	3.523×10^{-6}	-8.346×10^{-3}	6.803×10^{-3}	9.124×10^{-4}
μ_f = 0.06	4.721×10^{-4}	5.146×10^{-6}	-8.309×10^{-3}	1.227×10^{-3}	1.274×10^{-3}
μ_f = 0.10	6.051×10^{-4}	7.566×10^{-6}	-8.398×10^{-3}	2.385×10^{-3}	2.221×10^{-2}

Case	E_{sn} $[J]$	E_{st} $[J]$	W_{dn} $[J.s^{-1}]$	W_{dt} $[J.s^{-1}]$	W_{df} $[J.s^{-1}]$
μ_f = 0.00	8.358×10^{-6}	0	0	0	0
μ_f = 0.01	7.379×10^{-6}	2.472×10^{-10}	0	0	9.231×10^{-4}
μ_f = 0.03	5.335×10^{-6}	1.773×10^{-9}	0	0	2.233×10^{-3}
μ_f = 0.06	8.381×10^{-6}	5.320×10^{-9}	0	0	3.406×10^{-3}
μ_f = 0.10	1.069×10^{-5}	1.687×10^{-8}	0	0	6.441×10^{-3}

Effective restitution coefficient

In section 3.3.1 it was suggested that the effective restitution coefficient could be used as an alternative to include the effect of frictional dissipation in the TFM. To asses whether this is a valid approach, two DPM simulations were conducted. The collisional parameters of case 1, are e_n = 0.97, e_t = 1.00 and μ_f = 0.10. The effective restitution coefficient has been determined using Equation 3.20. Therefore the collisional parameters in case 2 were, $e_n = e_{eff}$ = 0.86, e_t = 1.00 and μ_f = 0.00.

Table 3.12: Settings for DPM simulations.

e_n	0.86, 0.97	μ_f	0.00, 0.10
e_t	1.0	u_0	0.66 $m.s^{-1}$

The obtained time-averaged solids velocities of the simulations are given in Figure 3.17. This figure shows that the time-averaged solids circulation patterns have different shapes. For case 1, the vortices extend from top to bottom, however for case 2, two small additional vortices appear at the bottom of the fluidized bed. In the experiments, the two lower vortices were also visible, however, the vortices moved in the other direction compared to the simulations of case 2.

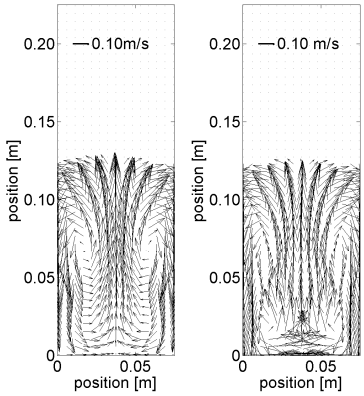

Figure 3.17: Influence of the effective coefficient of restitution on the time-averaged solids velocity of the DPM simulations. Superficial gas velocity: 2.5 u_0/u_{mf}, number of particles ~36,500 particles, and packed bed aspect ratio of 1. (a) e_n = 0.97, e_t = 1.00 and μ_f = 0.10; (b) e_n = e_{eff} = 0.86, e_t = 1.00 and μ_f = 0.00.

The lateral profiles of the time-averaged axial solids velocity for the simulation with friction and with the effective restitution coefficient are given in Figure 3.18 at two different heights above the distributor. It can be seen that for the simulation with friction, the area where the particles ascend is smaller than for the simulation with the effective restitution coefficient. In addition, two peaks appear in the time-averaged axial solids velocity suggesting that the bubble plumes in the simulation with friction reach each other at lower bed heights than those in the simulation with the effective restitution coefficient. The maximum upward particle velocity is higher for the simulation with friction.

In Figure 3.19 the influence of the effective restitution coefficient on the time-averaged bubble properties are given. It can be seen from Figure 3.19a that in case 2, the bubbles appear at higher axial positions in the fluidized bed. However, when the bubbles appear, they seem to coalesce faster and reach the same diameter as case 1. Moreover, the bubble size in case 2 seems to have reached its maximum, whereas in

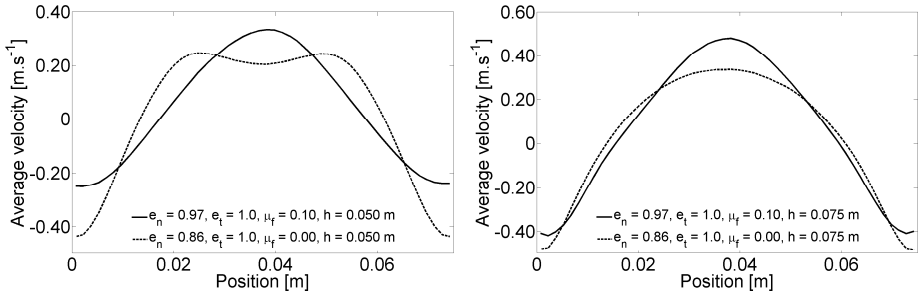

Figure 3.18: Influence of the effective restitution coefficient the time-averaged axial solids velocity at different positions above the distributor. Superficial gas velocity: 2.5 u_0/u_{mf}, number of particles ~36,500 particles, and packed bed aspect ratio of 1. (a) h = 0.05 m; (b) h = 0.075 m.

case 1, the bubble size is still increasing. The bubble rise velocity as function of the bubble diameter is presented in Figure 3.19c. It can be seen that the bubble rise velocity for both cases is similar. The influence of the effective restitution coefficient on the visual bubble flow rate is shown in Figure 3.19e. Again, from this figure it can be concluded that the bubbles appear higher above the distributor when case 2 is compared with case 1. Finally, the influence of the effective restitution coefficient on the bubble aspect ratio is presented in Figure 3.19f. When an effective restitution coefficient is used, the shape of the bubbles are elongated and when the the bubbles grow, they become more spherical. The shape of the bubbles when friction is included, is more spherical from the beginning and becomes slightly elongated when it grows in the fluidized bed. Therefore the bubbles in the simulation when friction is included are more likely to coalesce with bubbles next to each other and by that enhancing the lateral movement of the bubbles in the fluidized bed.

In Table 3.13 the influence of the effective coefficient of restitution on the contributions to the energy balance is presented. The kinetic energy, the potential energy of the normal spring and the energy dissipated by

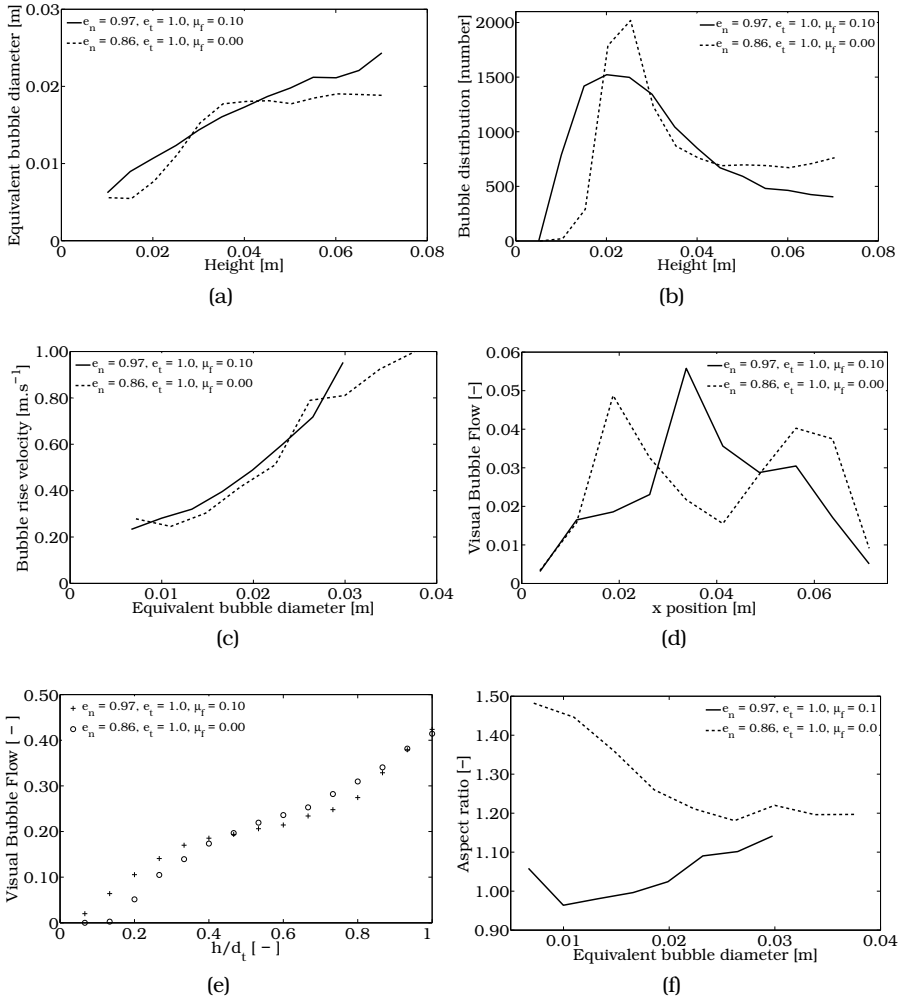

Figure 3.19: Influence of the effective restitution coefficient on the time-averaged bubble properties, (a) Equivalent bubble diameter vs. height above the distributor; (b) Number of bubbles vs. height above the distributor; (c) Averaged bubble rise velocity vs. equivalent bubble diameter; (d) Indicative axial visual bubble flow vs height above the distributor at 0.05 m above the distributor; (e) Visual bubble flow vs. height above the distributor; (f) Bubble aspect ratio vs. equivalent bubble diameter.

the normal dashpot are the three energy terms which are higher when the effective coefficient of restitution is used instead of the coefficient of restitution in the normal direction and the friction coefficient. However, the total energy dissipated due to particle-particle collisions and particle-particle friction is slightly lower when collisions are calculated using the effective restitution. It can therefore be concluded that not only the magnitude of energy dissipated due to collisions and friction is important for the hydrodynamics of a bubbling fluidized bed, also nature of the energy dissipation is important.

Table 3.13: Influence of effective coefficient of restitution on the energy levels, where the work terms have been time-averaged over a time span 10-15 s.

Case	E_{kin} $[J]$	E_{rot} $[J]$	E_{pot} $[J]$	W_{drag} $[J.s^{-1}]$	W_{pres} $[J.s^{-1}]$
Case 1	6.634×10^{-4}	6.933×10^{-6}	-8.490×10^{-3}	2.560×10^{-3}	2.485×10^{-3}
Case 2	7.856×10^{-4}	2.509×10^{-9}	-8.417×10^{-3}	1.588×10^{-3}	1.936×10^{-3}
Case	E_{sn} $[J]$	E_{st} $[J]$	W_{dn} $[J.s^{-1}]$	W_{dt} $[J.s^{-1}]$	W_{df} $[J.s^{-1}]$
Case 1	5.538×10^{-6}	1.475×10^{-8}	1.071×10^{-3}	0	6.030×10^{-3}
Case 2	6.788×10^{-6}	0	5.230×10^{-3}	0	0

Influence of the particle density

Baeyens and Geldart (1986) compared different particle types and found a difference in fluidization behavior for different types. Baeyens and Geldart related the differences in fluidization behavior to the Archimedes Number. They stated that when the Archimedes Number is higher, the gas flow through the bubbles will increase, resulting in smaller bubbles because less gas is available for bubble formation.

$$Ar = \frac{d_p^3 \rho_g \left(\rho_s - \rho_g\right) g}{\mu^2} \tag{3.29}$$

To investigate the influence of the particle density on the bed hydrodynamics, two simulations with different particle densities (~800 and 1000 $kg.m^{-3}$) and therefore two different Archimedes Numbers (2.81×10^4

and 3.8 $\times 10^4$) are compared. The particle density was not increased more, otherwise the particles would no longer belong to the Geldart B class.

Table 3.14: Settings for DPM simulations.

e_n	0.80	μ_f	0.10
e_t	0.60	u_0	0.66, 0.81 $m.s^{-1}$

To be able to compare the results of the two different particle densities the superficial gas velocity ratio u_0/u_{mf} was kept constant for both simulations. Therefore, the minimum fluidization velocity of the particles with a density of 1000 $kg.m^{-3}$ was determined with an independent DPM simulation, as described in section 3.4.1.

In Figure 3.20 a snapshot of the DPM simulation is given for both simulations at $t = 10\ s$. The coefficient of restitution in the normal direction, in the tangential direction and the friction coefficient for the three simulations were respectively 0.80, 0.60 and 0.1.

In Figure 3.21 corresponding the time-averaged solids velocity is presented. Two distinct vortices appear in both simulations. The vortices extend from the top to the bottom of the bed. The time-averaged particle velocity for the simulation with the higher density is not yet completely symmetric indicating that the time-averaged pattern is not completely developed.

The time-averaged axial particle velocity at 0.05 and 0.75 m above the distributor is given in Figure 3.22. It can be seen that the time-averaged axial particle velocity for both densities are similar at the same height above the distributor. Although the particle circulation is somewhat stronger at higher particle density.

In Figure 3.23 the time-averaged bubble properties are given. The average bubble diameter as function of the height in the bed is given in Figure 3.23a. It can be seen that the averaged bubble diameter of the simulation with a particle density of 1000 $kg.m^{-3}$ exceeds the averaged bubble diameter obtained for the lower particle density somewhat. Furthermore, it can be seen in Figure 3.23b, that the number of bubbles

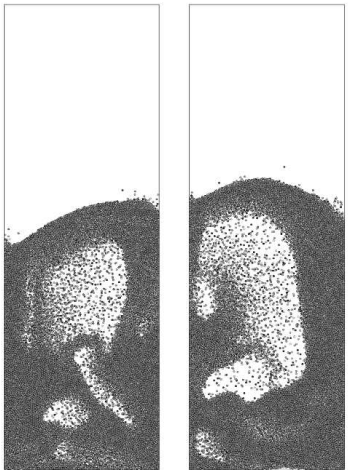

(a) (b)

Figure 3.20: Influence of the particle density (Archimedes Number), snapshots of the DPM simulations. Superficial gas velocity: 2.5 u_0/u_{mf}, number of particles ~36,500 particles, and packed bed aspect ratio of 1. (a) ρ_p = ~800 $kg.m^{-3}$, u_0 = 0.66 $m.s^{-1}$ (b) ρ_p = 1000 $kg.m^{-3}$, u_0 = 0.81 $m.s^{-1}$.

is comparable. The influence of the particle density on the bubble rise velocity is presented in Figure 3.23c. It can be seen that the bubble rise velocity is hardly influenced by the particle density. Finally the visual bubble flow rate as function of the height (normalized with the diameter) is given in Figure 3.23e and as function of the lateral position in the fluidized bed at 0.05 m above the distributor in Figure 3.23d. It can be seen that the visual bubble flow rate in the simulation with the particle density of 1000 $kg.m^{-3}$, is slightly higher compared to the visual bubble flow obtained for a particle density of ~800 $kg.m^{-3}$. This can be attributed to the occurrence of larger diameter bubbles in the simulation with the higher particle density.

In Table 3.15 the influence of the effective coefficient of restitution on the contributions to the energy balance is presented. It can be seen that the energy levels for the simulations with the higher particle density is much higher compared to those obtained for the lower particle density.

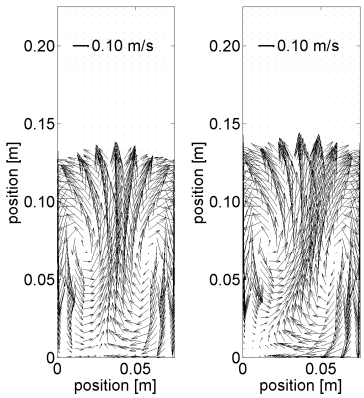

Figure 3.21: Influence of the particle density on the time-averaged solids velocity. Superficial gas velocity: 2.5 u_0/u_{mf}, number of particles ~36,500 particles, and packed bed aspect ratio of 1. (a) ρ_p = ~800 $kg.m^{-3}$, u_0 = 0.66 $m.s^1$ (b) ρ_p = 1000 $kg.m^{-3}$, u_0 = 0.81 $m.s^{-1}$.

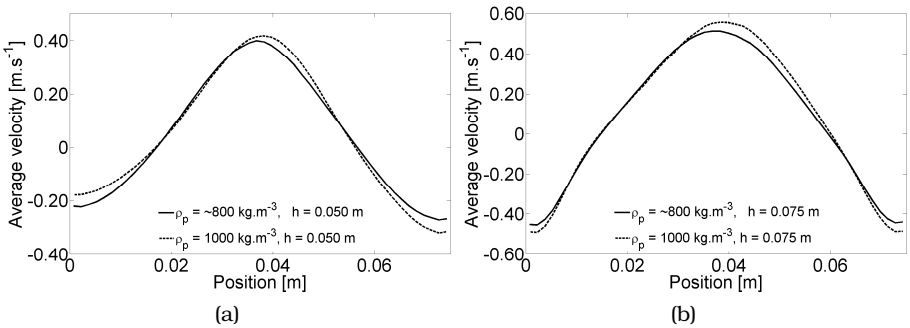

Figure 3.22: Influence of the particle density on the time-averaged axial solids velocity. Superficial gas velocity: 2.5 u_0/u_{mf}, number of particles ~36,500 particles, and packed bed aspect ratio of 1. (a) h = 0.05 m; (b) h = 0.075 m.

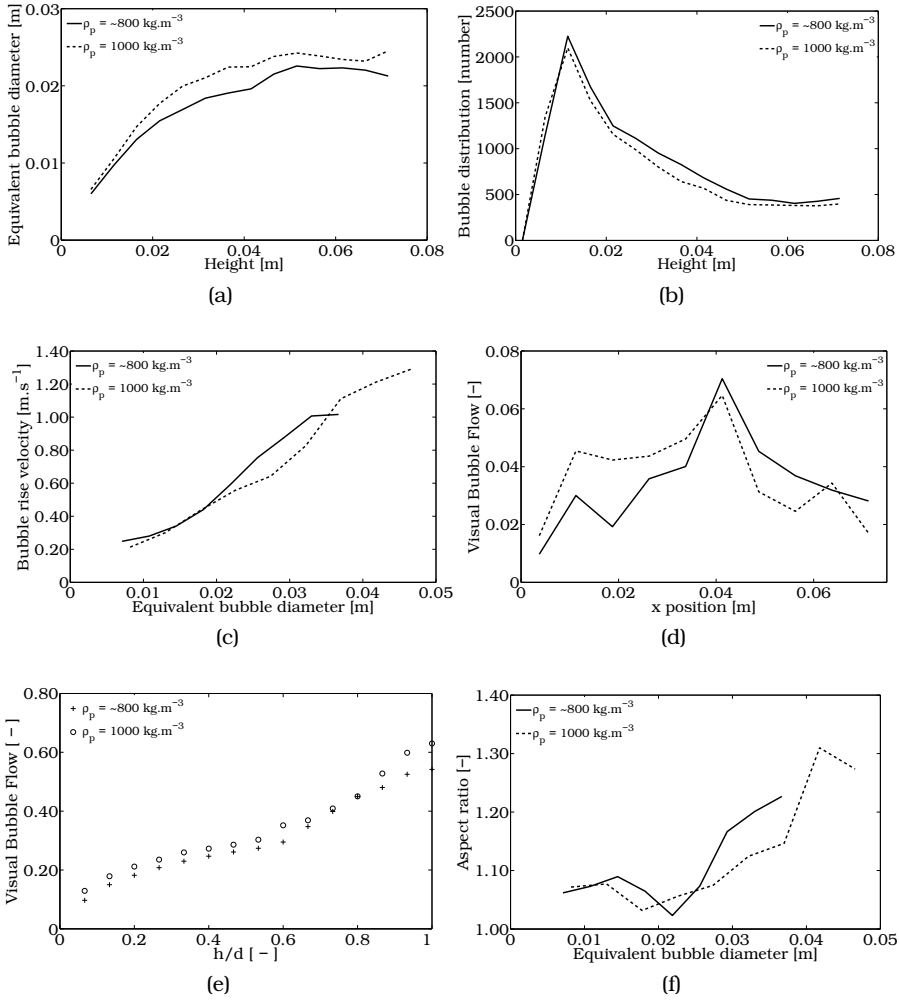

Figure 3.23: Influence of the density the time-averaged bubble properties, (a) Equivalent bubble diameter vs. height above the distributor; (b) Number of bubbles vs. height above the distributor; (c) Averaged bubble rise velocity vs. equivalent bubble diameter; (d) Indicative axial visual bubble flow vs height above the distributor at 0.05 m above the distributor; (e) Visual bubble flow vs. height above the distributor; (f) Bubble aspect ratio vs. equivalent bubble diameter.

Table 3.15: Influence of particle density on the energy levels, where the work terms have been time-averaged over a time span 10-15 s.

Case	E_{kin} $[J]$	E_{rot} $[J]$	E_{pot} $[J]$	W_{drag} $[J.s^{-1}]$	W_{pres} $[J.s^{-1}]$
ρ_p = ~800 kg.m^{-3}	8.236×10^{-4}	5.259×10^{-6}	-8.530×10^{-3}	3.292×10^{-3}	3.230×10^{-3}
ρ_p = 1000 kg.m^{-3}	1.200×10^{-3}	7.582×10^{-6}	-1.180×10^{-2}	9.896×10^{-3}	1.015×10^{-2}
Case	E_{sn} $[J]$	E_{st} $[J]$	W_{dn} $[J.s^{-1}]$	W_{dt} $[J.s^{-1}]$	W_{df} $[J.s^{-1}]$
ρ_p = ~800 kg.m^{-3}	5.850×10^{-6}	8.742×10^{-9}	3.824×10^{-3}	1.684×10^{-5}	5.020×10^{-3}
ρ_p = 1000 kg.m^{-3}	6.559×10^{-6}	2.281×10^{-8}	8.259×10^{-3}	3.999×10^{-5}	1.245×10^{-2}

Influence of the coefficient of normal restitution on TFM simulations

To investigate the influence of the coefficient of normal restitution on the hydrodynamics of a bubbling fluidized bed, several TFM simulations were performed in which only the coefficient of normal restitution coefficient for particle-particle (e_n) and particle-wall ($e_{n,wall}$) were varied. The time-averaged solids velocity is presented in Figure 3.24. It can be seen, two distinct vortices appear in the top half of the fluidized bed. As the normal restitution coefficient decreases, the vortices are elongated, stretching from top to bottom when the normal restitution coefficient is set to 0.90. The qualitative particle behavior agrees with the particle behavior in literature, results reported in chapter 2 and with the results obtained from the DPM simulations. The time-averaged axial solids velocity are presented in Figure 3.25. When comparing Figure 3.25 with Figure 3.11 the time-averaged solids velocities profiles do not correspond with each other. The two peaks which were visible in the DPM simulations, are not present in the TFM simulations. Furthermore, in Figure 3.25a it can be seen that the simulation with an normal restitution coefficient results of 0.99 has the highest solids velocity at 0.05 m above the distributor. This is caused by the fact that the bottom of the two vortices in the fluidized bed are positioned exactly at 0.05 m above the distributor. In addition, the solids velocity near the wall in the TFM simulation is considerable lower than in the DPM simulations. Suggesting that the solids phase in the TFM simulations lose more energy at the wall the the solids phase in the DPM simulations, which would resulting in larger

bubbles and higher solids circulation in the fluidized bed. The influence of the boundary conditions on the TFM simulations will be investigated in the next section were TFM simulations with the free-slip boundary conditions are presented.

The influence of the coefficient of restitution in the normal direction on the bubble properties is presented in Figure 3.26. When these results are compared with Figure 3.12, it can be seen that the bubble growth in the fluidized bed in the TFM is faster than in the DPM simulations, see Figure 3.12a and Figure 3.26a. The number of bubbles in the DPM simulations is larger than in the TFM simulations, see Figure 3.26b and 3.12b. However, the largest difference between the TFM and DPM simulation is the difference in the bubble aspect ratio, which are presented in Figures 3.26f and 3.12f. In the DPM simulations, the small bubbles are elongated, especially at lower coefficients of restitution, and when the bubbles grow the bubbles become more flattened, in the TFM simulations the bubbles aspect ratio is almost constant as function of the equivalent bubble diameter. The difference in bubble shape can cause the bubbles to coalesce faster in the TFM, resulting in a higher solids circulation.

The contributions to the energy balance is presented in Table 3.16. It can be seen that the potential energy remains approximately the same for the different coefficients of restitution. Whereas the work performed due to restitution, drag and pressure and the kinetic energy decrease significantly when the coefficient of restitution increases. When comparing the different contributions of the energy balance to the energy balance in the DPM, see Table 3.9, it can be seen that the magnitude of the different contributions in the energy balance are of the same order.

Influence of the boundary conditions on TFM simulations

To investigate the influence of the boundary conditions in the TFM, the simulations from the previous section, which were performed with partial slip boundary conditions will be compared to simulations in which free-slip boundary conditions were applied to the walls of the fluidized bed. The normal restitution coefficient in the free-slip simulations were

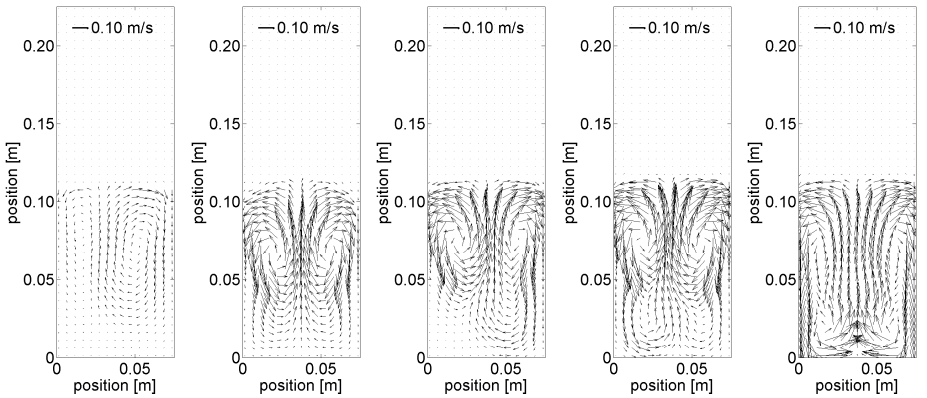

Figure 3.24: Influence of the normal restitution coefficient on the time-averaged solids velocity using TFM simulations. Superficial gas velocity: 2.5 u_0/u_{mf}, and packed bed aspect ratio of 1. $e_n,wall$ is equal to e_n. (a) e_n = 1.00; (b) e_n = 0.99; (c) e_n = 0.97; (d) e_n = 0.94; (e) e_n = 0.90.

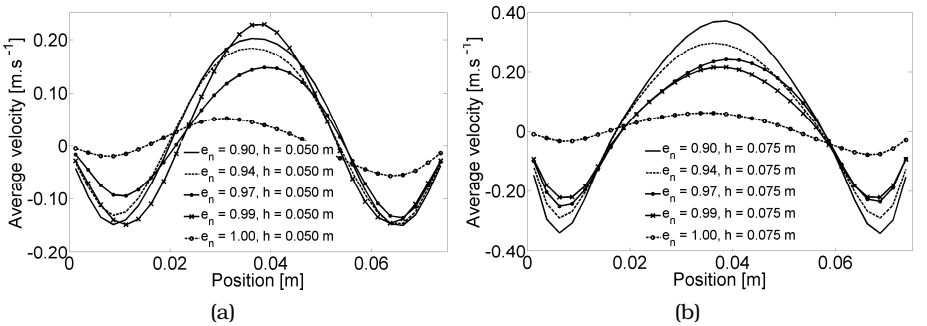

Figure 3.25: Influence of the normal restitution coefficient on the lateral profiles of the time-averaged solids axial velocity using TFM simulations. Superficial gas velocity: 2.5 u_0/u_{mf}, and packed bed aspect ratio of 1. $e_n,wall$ is equal to e_n. (a) h = 0.05 m; (b) h = 0.075 m.

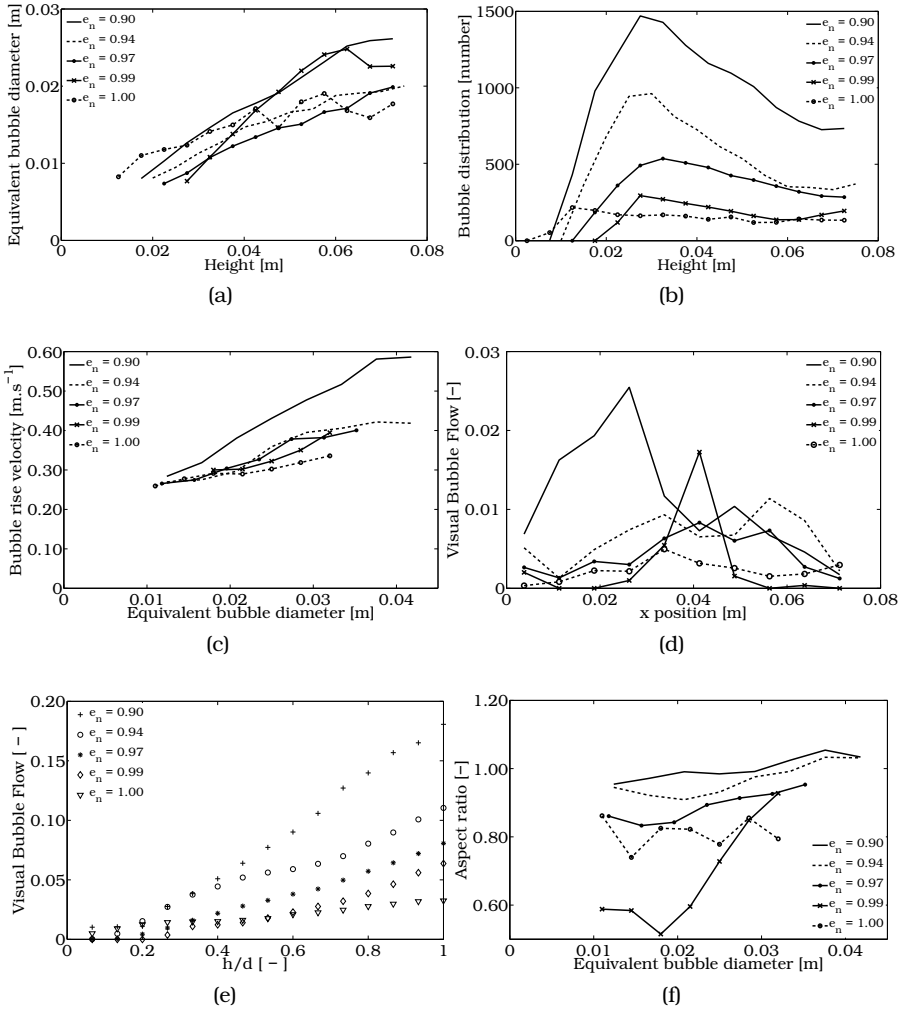

Figure 3.26: Influence of the normal restitution coefficient on the time-averaged bubble properties in the TFM simulations, (a) Equivalent bubble diameter vs. height above the distributor; (b) Number of bubbles vs. height above the distributor; (c) Averaged bubble rise velocity vs. equivalent bubble diameter; (d) Indicative axial visual bubble flow vs height above the distributor at 0.05 m above the distributor; (e) Visual bubble flow vs. height above the distributor; (f) Bubble aspect ratio vs. equivalent bubble diameter.

Table 3.16: Influence of coefficient of restitution in the normal direction on the energy levels where the depth of the bed was assumed to be 0.00628 m, to be able to compare the values with the DPM simulations.

Case	E_{conv} $[J]$	E_{gran} $[J]$	E_{pot} $[J]$	W_{rest} $[J.s^{-1}]$	W_{drag} $[J.s^{-1}]$
e_n = 0.90	4.088×10^{-4}	2.826×10^{-5}	-8.040×10^{-3}	-4.265×10^{-3}	2.224×10^{-3}
e_n = 0.94	3.328×10^{-4}	3.642×10^{-5}	-7.991×10^{-3}	-3.430×10^{-3}	1.682×10^{-3}
e_n = 0.97	2.248×10^{-4}	4.584×10^{-5}	-7.934×10^{-3}	-2.189×10^{-3}	1.066×10^{-3}
e_n = 0.99	1.570×10^{-4}	6.154×10^{-5}	-7.855×10^{-3}	-1.033×10^{-3}	6.324×10^{-4}
e_n = 1.00	1.262×10^{-4}	7.222×10^{-5}	-7.920×10^{-3}	0	5.432×10^{-4}

Case	$W_{drag,gran}$ $[J.s^{-1}]$	W_{pres} $[J.s^{-1}]$
e_n = 0.90	-3.316×10^{-4}	2.367×10^{-3}
e_n = 0.94	-4.044×10^{-4}	1.951×10^{-3}
e_n = 0.97	-4.748×10^{-4}	1.405×10^{-3}
e_n = 0.99	-6.324×10^{-4}	1.055×10^{-3}
e_n = 1.00	-7.348×10^{-4}	5.194×10^{-4}

also varied between 0.90 and 1.00. In Figure 3.27 the lateral profiles of the time-averaged axial solids velocity in the TFM simulations are presented. The lateral profiles of the axial solids velocity of the simulations with free-slip and partial slip differ considerably from each other. In the simulations with partial slip a single peak is visible, where in the simulations with the free-slip boundary conditions two peaks are visible in the time-averaged axial solids velocity profiles. The two peaks in the time-averaged axial solids velocity profiles correspond with the results found in the DPM simulations in which the coefficient of normal restitution was investigated, see Figure 3.11. Not only the shape of the profiles agree, but also there is good agreement in the solid velocities between the DPM simulations and TFM simulations with free-slip boundary conditions.

In Figure 3.28 the bubble aspect ratio as function of the equivalent bubble diameter is presented. The bubble shape in the simulations with partial slip is more spherical than the bubbles in the simulations with free-slip. The spherical bubbles in the partial slip simulations will coalesce faster with neighboring bubbles than the bubbles in the free-slip simulations, rand as a result bubbles which are formed at opposite sides of the bed will reach each other at a lower position above the distribu-

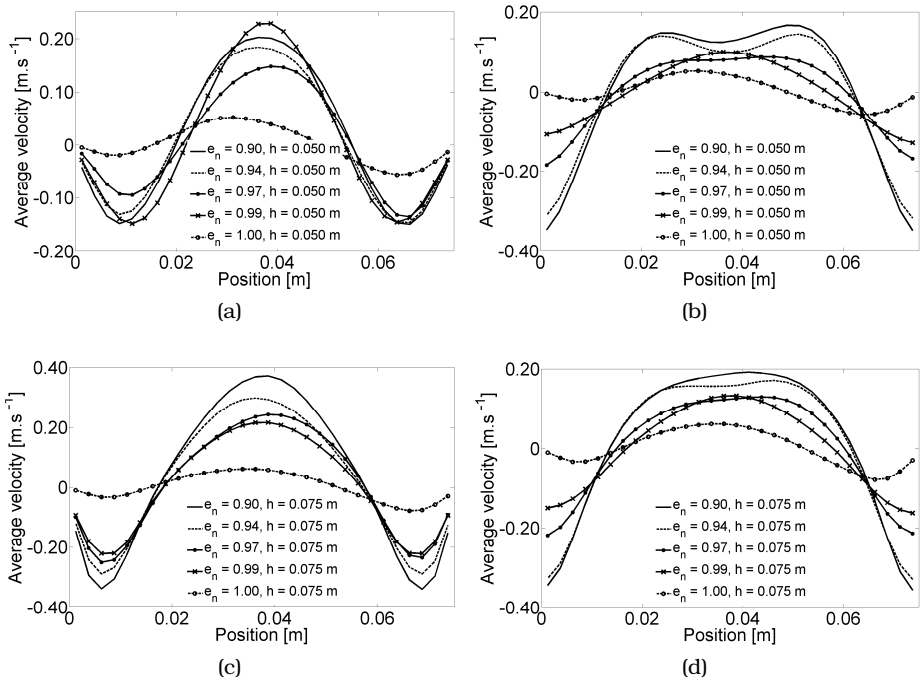

Figure 3.27: Influence of the boundary conditions on the lateral profiles of the time-averaged solids axial velocity using TFM simulations. Superficial gas velocity: 2.5 u_0/u_{mf}, and packed bed aspect ratio of 1. $e_{n,wall}$ is equal to e_n. (a) boundary condition: partial slip, h = 0.05 m; (b) boundary condition: free slip, h = 0.05 m; (c) boundary condition: partial slip, h = 0.075 m; (d) boundary condition: free slip, h = 0.075 m.

tor. When comparing the bubble aspect ratio of the TFM simulation with free-slip with the DPM simulations presented in Figure 3.12f it can be seen that qualitatively the same bubble behavior can be seen.

3.4.3 Comparison with Particle Image Velocimetry and Digital Image Analysis with DPM and TFM

In this section, the results obtained from DPM and TFM simulations will be compared with experimental data obtained with PIV and DIA

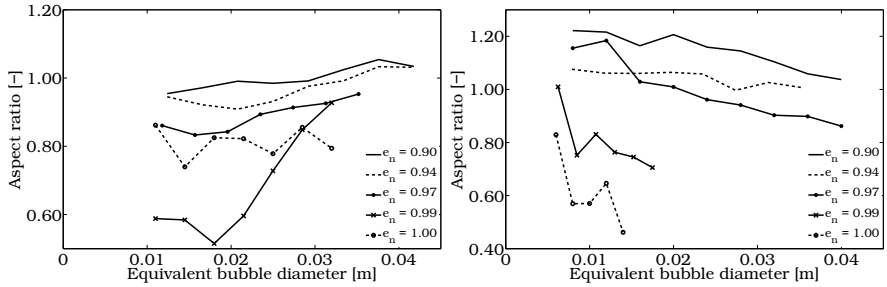

Figure 3.28: Influence of the boundary conditions on the bubble aspect ratio vs. equivalent bubble diameter, (a) boundary condition: partial slip; (b) boundary condition: free slip.

(presented in chapter 2). The settings of the experiments and the CFD models have been summarized in Table 3.17. The fluidized bed in the experiments was filled with glass beads, therefore the collisional properties of glass beads have been used in the simulations. The glass beads in the experiments had a particle size distribution of 0.40-0.60 mm, with a mean diameter of 0.485 mm.

In Figures 3.29 and 3.30 the time-averaged particle velocities for the PIV combined with DIA experiments, DPM and TFM are respectively compared at u_0/u_{mf} = 2.0 and u_0/u_{mf} = 2.5. It can be seen that the shape of the macroscopic circulation patterns for the experiments, the DPM and the TFM are similar at both superficial gas velocities. The particles move from the corners upwards toward the center of the fluidized bed and when they reach the center, move upward. When the particles reach the top, they are transported towards the side wall and subsequently move downwards to the bottom of the fluidized bed. However from the figures it can be observed, quantitative, that the solids phase in the TFM simulations is moving more vigorously through the fluidized bed than the solids in the experiments and the DPM simulations.

In Figures 3.31 and 3.32 the lateral profiles of the time-averaged axial particle velocity are given at two different heights (0.05 and 0.10 m) above the distributor for both superficial gas velocities. It can be seen

Table 3.17: Settings for the experiments, DPM and TFM simulations, for a 15 *cm* wide bubbling fluidized bed.

Parameter	**Exp.**	**DPM**	**TFM**
Width x-direction [m]	0.15	0.15	0.15
Depth y-direction [m]	0.015	0.00291	2.5×10^{-3}
Height z-direction [m]	1.00	0.45	0.30
Grid cells (x,y,z)	-	150,1,450	60,1,120
Packed bed height [m]	0.15	0.15	0.15
# of particles [-]	~650.000	~ 650.000	-
Particle material	Glass	Glass	Glass
Particle diameter [m]	4-6$\times10^{-4}$	4.85×10^{-4}	4.85×10^{-4}
Particle density [kg.m^{-3}]	2500	2500	2500
Min. fluidization velocity [m.s^{-1}]	0.18	0.21	0.21
Superficial gas velocity [m.s^{-1}]	0.36,0.45	0.42,0.53	0.42,0.53
Normal restitution coef. [-]	-	0.97	0.97
Tangential restitution coef. [-]	-	0.33	-
Frictional coefficient [-]	-	0.10	-
Flow solver time step [s]	-	1.0×10^{-4}	1.0×10^{-5}
Simulation time [s]	-	~20	30

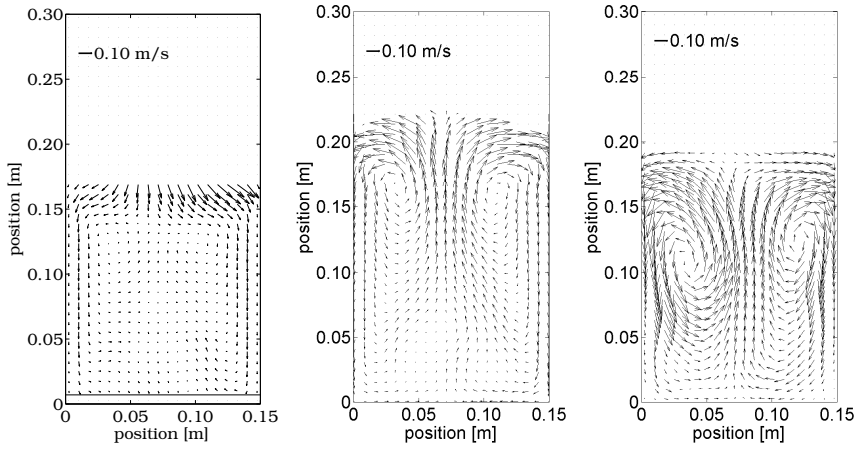

(a) (b) (c)

Figure 3.29: Time-averaged particle velocity for a superficial gas velocity of 2.0 u_0/u_{mf}. (a) PIV-DIA; (b) DPM; (c) TFM.

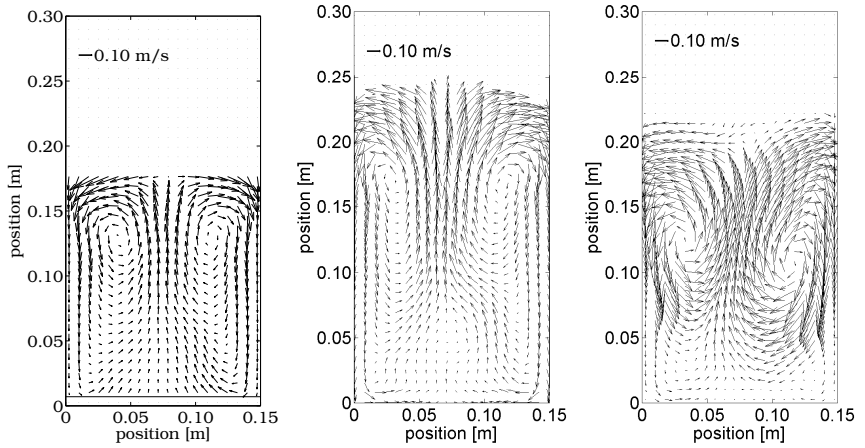

Figure 3.30: Time-averaged particle velocity for a superficial gas velocity of 2.5 u_0/u_{mf}. (a) PIV-DIA; (b) DPM; (c) TFM.

that the TFM over predicts both the ascending and descending particle movement. In addition, the area in which the particles descend, is larger for the TFM simulations than the area in which the particles descend in the experiments and the DPM simulations. Furthermore, the experimental lateral profiles of the time-averaged axial particle velocity is always lower in the ascending and descending motion in comparison with the DPM results. However, the shape of the curves is similar.

In Figures 3.33 and 3.34 the time-averaged bubble properties of the experiments are compared with the DPM and TFM simulations. First, in Figures 3.33a and 3.34a the equivalent bubble diameter versus the height above the distributor is given. It can be seen that the bubbles in the DPM simulation are the largest, followed by the TFM and experimental results. The larger bubbles in the DPM and TFM simulation could be caused by the larger excess flow rate. The theoretical excess flow rate at $2.0u_0/u_{mf}$ in the experiments is $0.65\,(0.36-0.18) = 0.117 m.s^{-1}$ and for the simulations the theoretical excess flow rate is $0.65\,(0.42-0.21) = 0.137 m.s^{-1}$, approximately 15% higher. In Figures 3.33d and 3.34d the

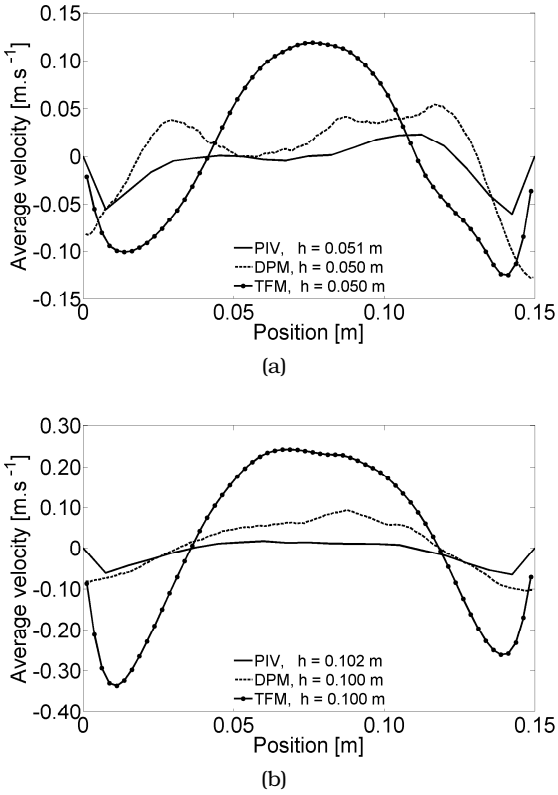

Figure 3.31: Time-averaged axial particle velocity in experiment, DPM and TFM simulation, packed bed aspect ratio = 1, superficial gas velocity of 2.0 u_0/u_{mf}, (a) h = 0.05 m; (b) h = 0.10 m.

visual bubble flow rate is given for both superficial gas velocities. In both figures, the visual bubble flow rate in the DIA experiments reaches a plateau of respectively 0.3 and 0.35. The DPM and the TFM results show that the visual bubble flow rises slower, however in the DPM and in the TFM, the visual bubble flow does not reach a plateau value and keeps increasing to the top of the fluidized bed. This suggests that in the top half of the bed more gas is passing through the fluidized bed as bubbles than in the experiments. In Figures 3.33b and 3.34b the normalized bubble distribution over the height of the fluidized bed is

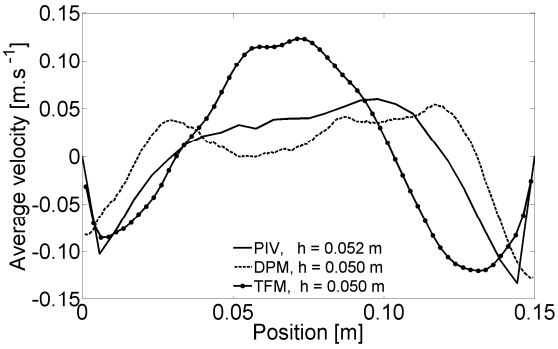

(a)

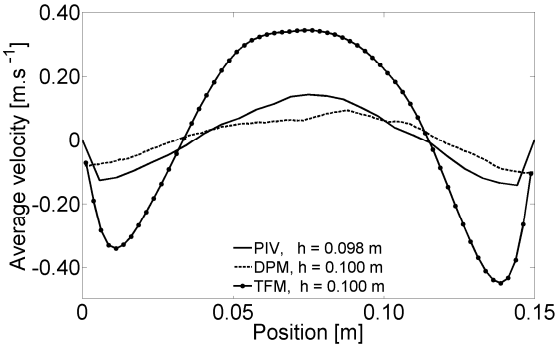

(b)

Figure 3.32: Time-averaged axial particle velocity in experiment, DPM and TFM simulation, packed bed aspect ratio = 1, superficial gas velocity of 2.5 u_0/u_{mf}, (a) h = 0.05 m; (d) h = 0.10 m.

presented. The bubble distribution is normalized by dividing the number of bubbles at a given height by the total number of bubbles. This has been done because the time-span of the experiments and the simulations was not the same. For both superficial gas velocities, the DIA and the DPM results show the same trend, only the bubbles appear slightly higher in the DPM simulations. In the TFM simulations, the bubbles appear at a even higher position above the distributor in the fluidized bed and the peak is not as high as in the experiments and the DPM. In Figures 3.33e and 3.34e the bubble aspect ratio is presented.

From these figures, it becomes clear that the shape of the bubbles in the experiments and the DPM simulations show the same trend, however the bubbles have not exactly the same sphericity. The TFM simulations show somewhat different bubble aspect ratios. This suggests that the collisional model used in the DPM simulations describes the collisions in the experiments accuratly, the collisional properties in the TFM miss the energy dissipation in the due to the friction and due to the energy dissipation due to tangential dashpot, as was discussed in the previous sections about the collisional properties. Finally, in Figures 3.33c and 3.34c the bubble rise velocity is plotted versus the bubble diameter for both superficial gas velocities. Both the TFM and the DPM over predict the rise velocity of a bubble with a given bubble diameter. It appears that the smaller bubbles in the TFM simulations rise faster through the fluidized bed than in the DPM simulations.

There are other reasons why the experimental results differ from the DPM and (especially) the TFM results. In the experiments, glass beads with a particle size ranging from 400 to 600 μm were used, whereas in the simulations a uniform particle size of 485 μm was used. Furthermore, in the simulations the glass beads were assumed to be perfectly round, i.e. a sphericity of 1, which was not the case in the experiments. In the simulations, the collisional properties of the walls were assumed to have the same as the collisional properties of the glass beads, in the experiments, this was probably not the case because the side of the column was made of aluminum. Due to the relatively low superficial gas velocity, the distributor used in the experiments may not have distributed the gas perfectly over the bottom of the fluidized bed. Finally, the fluidized bed could be slightly static which could cause glass beads moving slower across the glass plates at the front and back of the fluidized bed.

3.5 Conclusions

To investigate the influence of the microscopic particle properties on the time-averaged solids phase velocity profiles and time-averaged bubble properties detailed DPM and TFM simulations have been performed.

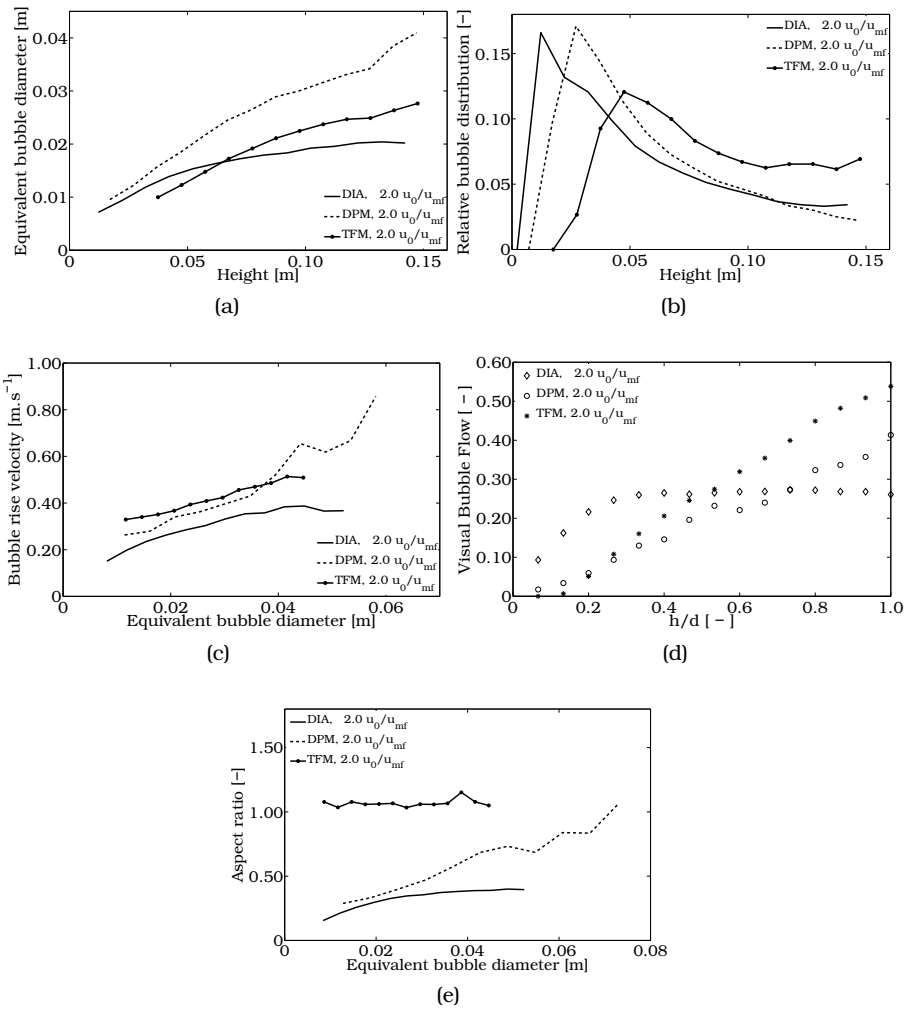

Figure 3.33: Comparison of the time-averaged bubble properties at a superficial gas velocity of 2.0 u_0/u_{mf}, (a) Equivalent bubble diameter vs. height above the distributor; (b) Number of bubbles vs. height above the distributor; (c) Averaged bubble rise velocity vs. equivalent bubble diameter; (d) Visual bubble flow vs. height above the distributor; (e) Bubble aspect ratio vs. equivalent bubble diameter.

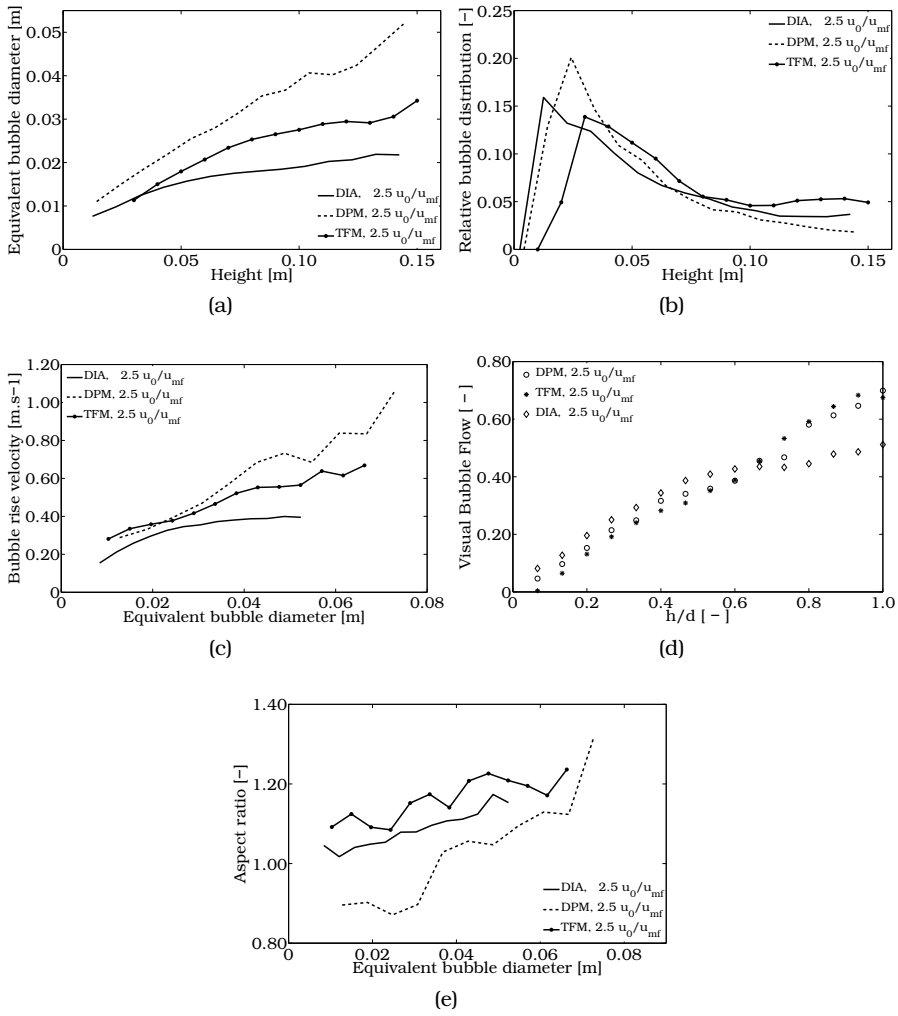

Figure 3.34: Comparison of the time-averaged bubble properties at a superficial gas velocity of 2.5 u_0/u_{mf}, (a) Equivalent bubble diameter vs. height above the distributor; (b) Number of bubbles vs. height above the distributor; (c) Averaged bubble rise velocity vs. equivalent bubble diameter; (d)) Visual bubble flow vs. height above the distributor; (e) Bubble aspect ratio vs. equivalent bubble diameter.

The collision properties of the particles influence the minimum fluidization velocity which especially holds for the friction coefficient. This is caused by the fact that particles loose mechanical energy when they collide with each other which prevails at incipient fluidization condition.

Furthermore it was found that the collision properties have a large influence on the time-averaged solids velocity and time-averaged bubble properties. The time-averaged bubble size and the upward time-averaged solids velocity are larger when more energy is dissipated due to the particle-particle or particle-wall interactions. It has been shown that the energy dissipated in a bubbling fluidized bed due to the tangential dashpot is two orders of magnitude smaller than the energy dissipated by the normal dashpot and the friction between particles and particles and particles and wall. Besides the magnitude of the dissipated energy, the precise origin of the energy dissipation is also important for the shape of the bubbles. When the energy is only dissipated by the normal dashpot, the aspect ratio of the bubbles is higher in comparison to when energy is only dissipated due to friction between particles. Therefore, it is not possible to include the energy dissipated by friction into an effective restitution coefficient. This was shown by independent DPM and TFM simulations.

The influence of the particle density is minor when the ratio between the superficial gas velocity and the minimum fluidization velocity is kept constant. If this ratio is kept the same, the ratio between the force exerted on two different particle types by the gas is the same.

Finally, the DPM and TFM results are compared to PIV-DIA measurements. It was shown that the trends for the emulsion phase and the bubble phase can be predicted with the DPM. Furthermore, it was concluded that the collisional model of the TFM is not very accurate to simulate a bubbling fluidized bed.

CHAPTER 4

Experimental study on the hydrodynamics of 3D bubbling fluidized bed with PEPT

ABSTRACT

In this chapter, the hydrodynamics of a freely bubbling, three dimensional, gas-solid fluidized bed has been experimentally investigated using different bed materials, different bed aspect ratios at different superficial gas velocities by performing Positron Emission Particle Tracking (PEPT) experiments. The fluidized bed was filled with either glass beads with a diameter of 400-600 μm or with linear low density polyethylene (LLDPE) particles with a diameter of 1000-1300 μm, having approximately the approximately the same ratio of Ar/Re_{mf}, ensuring dynamic similarity. Fluidization of both bed materials showed Geldart B type behavior. At lower superficial gas velocities two distinct vortices appear above each other for both types of bed material; when the superficial gas velocity is increased, the lower vortex disappears and the top vortex spans the entire length of the bed. Although qualitatively the same phenomena were observed, the time-averaged solids phase circulation rate in the fluidized bed filled with

LLDPE particles was higher than the time-averaged solids phase velocity in the fluidized bed filled with glass beads, despite the similar ratio Ar/Re_{mf} of these bed materials. When the bed aspect ratio is increased from 1 to 1.5, the vortices become elongated without altering the solids circulation rate. Differences in the particle-particle collisional properties (coefficients of restitution and particle friction coefficients) are believed to be the cause of the observed quantitative differences in the bed hydrodynamics via their influence on the bubble properties.

4.1 Introduction

In chapter 2 and 3 the bubble and solids phase characteristics in pseudo-2D bubbling fluidized beds were studied. However, to obtain quantative information about the solids motion in a full 3-dimensional (3D) bubbling gas-solid fluidized bed Positron Emission Particle Tracking (PEPT) experiments were conducted. PEPT is a measuring technique which has been developed since 1987 at the University of Birmingham. In this measuring technique a single radioactive particle is tracked during its path through the system in order to obtain information on the motion of the particulate phase. The advantage of using the non-intrusive PEPT technique over intrusive techniques (probes) is that the gas and particle flow is not disturbed at exactly the position where the flow is measured. In addition, an advantage of the PEPT technique compared to other (non-intrusive) particle tracking techniques is that there exists an elegant and rather precise technique to determine the particle position during the measurement, where for Radioactive Particle Tracking (RPT) measurements the location of the particle has to be reconstructed. Moreover, no calibration of the detectors is required before each PEPT measurement. A disadvantage of PEPT is, like all other particle tracking techniques, that a single measurement may take a long time in order to obtain statistically reliable results, since the movement of a single "representative" particle or a few particles is followed in time. Another difference between PEPT and RPT is that the half-live of the tracer particle is much lower for PEPT experiments. For both PEPT and RPT measurements the loss of activity of the tracer particle needs to be taken

into account, however, this is more straightforwardly accounted for in the PEPT measurements compared to RPT measurements. The final advantage of PEPT measurements compared to RPT is that in the PEPT measurements the tracer particle is an actual particle from the bulk of the fluidized bed, whereas the tracer particle used in RPT measurements is usually not exactly representative since the particle is prepared such that it resembles the bed particles as close as possible.

In literature, several articles have appeared reporting radioactive and positron emission particle tracking experiments. See for example Moslemian et al. (1992) who published RPT measurements in two fluidized beds (the first was a 0.19 m diameter column and the second bed had an internal diameter of 0.292 m and was equipped with internals) and a bubble column. In addition to the velocity profiles they determined the turbulent parameters, such as the Reynolds stresses and the turbulent dispersion coefficient. Mostoufi and Chaouki (2001) measured the diffusivity of the solids in a bubbling fluidized bed. They showed that the solids diffusivities increased with an increasing superficial gas velocity and that the diffusivities are linearly correlated to the axial solids velocity gradient. Mostoufi and Chaouki (2004) also investigated the existence of clusters in dense fluidized beds, they found that descending clusters were larger than ascending clusters and additionally that the size of the clusters increases with increasing in the superficial gas velocity. Stein et al. (2000) performed PEPT experiments to investigated the solids flow pattern, solid velocity, and solid circulation frequency in two fluidized beds with an inner diameter of 0.07 and 0.141 m. Furthermore Stein et al. (2002) performed an experimental verification of the scaling relationships for bubbling gas-fluidized beds using beds with an inner diameter of 0.07, 0.141 and 0.240 m. Hoomans et al. (2001) used PEPT measurements to validate their Discrete Element Model. They used a pseudo 2D fluidized bed with a width of 0.185 m and a depth of 0.020 m.

Furthermore, several articles have been published which compared the fluidization behavior of fluidized beds filled with glass beads and polyethylene particles. Fan et al. (2008) investigated the emulsion phase

velocity profiles for glass and polyethylene particles in a 0.152 m inner diameter fluidized bed using PEPT. The glass beads had a mean particle size of 352 μm and a minimum fluidization velocity of 0.15 $m.s^{-1}$ and the low density polyethylene particles had a mean particle size of 717 μm and a minimum fluidization velocity of 0.24 $m.s^{-1}$. They performed measurements for both particle types at two excess gas velocities of 0.25 and 0.42 $m.s^{-1}$ and found different solids phase velocity profiles and different bubble behavior for the two bed materials. For the glass beads they found that the particles moved upwards through the center of the fluidized bed and moved downwards near the walls, however when the polyethylene particles were used, they found different segments of upward movement at the wall and downward movement at the center and visa versa, upward motion at the wall and downward motion in the center. In addition Fan et al. (2008) measured the bubble rise velocity using an indirect measuring technique (using the jumps of the tracer particle) and found that the bubble growth for the polyethylene particles levels off at an intermediate section of the fluidized bed. They attributed the difference in bubble diameter to the difference in the Archimedes number of both particle types, this was first suggested by Baeyens and Geldart (1986).

Baeyens and Geldart (1986) stated that particles with a higher Archimedes number are more likely to possess a higher bubble gas through flow, yielding smaller bubbles because less air is available for the formation of bubbles. Furthermore, they found that the bubble size equations suggested by Darton and Werther are suitable for the glass beads, however the equations overpredict the bubble size for the polyethylene particles. However, these findings do not agree with the results reported by Hulme and Kantzas (2004) who used X-ray fluoroscopy to measure the bubble diameter in a fluidized bed filled with polyethylene particles. They found that they could describe the bubble diameter and bubble rise velocity in the fluidized bed by using the equations suggested by Werther (1978) and Kunii and Levenspiel (1991). However, the findings reported by Fan et al. (2008) and Hulme and Kantzas (2004) for the bubble behavior do not agree with the bubble behavior reported

in chapter 2, were the comparison between the glass and LLDPE particles were investigated using Digital Image Analysis. In addition, the difference in solids circulation patterns between the two different bed materials described by Fan et al. (2008) was not found using the novel PIV-DIA measurement described in chapter 2.

To obtain information about larger size fluidized beds, where wall effects are strongly reduced in comparison to small scale fluidized beds experiments, a series of dedicated Positron Emission Particle Tracking (PEPT) experiments have been conducted in a 0.306 m inner diameter fluidized bed. The influence of the superficial gas velocity, packed bed aspect ratio and bed material on the macroscopic circulation patterns was investigated.

First, the experimental set-up and the PEPT measuring technique will be described. Subsequently, the influence of the bed aspect ratio, fluidization velocity and type of bed material on the time-averaged solids velocity profiles are presented and discussed.

4.2 Experimental

The principle of PEPT is based on tracking a radioactively labeled particle, which is moving in a measuring vessel for a certain time, Parker et al. (1997). If two positions of the tracer particle and the difference in time between the two measured positions are known, the velocity between the two points can be calculated, under the assumption that the particle moves in a straight line between the two points. Which is a fair assumption in view of the relatively high temporal resolution. If the measurement is carried out for a sufficiently long period, the time-averaged solids velocity in the fluidized bed can be determined.

In this section the experimental setup will be described. Furthermore, the PEPT equipment, activation of the tracer particle and reconstruction of the particle position will be presented. Subsequently, the experimental settings and the experimental procedure followed in the PEPT experiments will be shortly outlined.

4.2.1 Setup

In Figure 4.1 the flow sheet of the setup is given. Air was used as fluidizing agent, which was supplied via a VACOM side channel blower VC375-1009. To control the air flow a VACON NXL 0016 frequency controller was used. The frequency of the blower could be varied between 10 and 70 Hz. To measure the gas flow rate, a calibrated iM-TM-A gas turbine meter was installed at such a distance behind the side channel blower, that inflow effects could be excluded. To prevent electrostatic build up in the fluidized bed, the air was humidified in a spray column. In the spray column the temperature of the water and the flow of the water could be varied, to achieve the desired air humidity. The humidity of the air was measured in the air chamber using an AFK-G-3T humidity meter (HI). The air was introduced into the air-chamber beneath the fluidized bed. As gas distributor a metal mesh was used with a pore size of 18 μm. The column was constructed of PVC and had an outer diameter of 0.314 m and an inner diameter of 0.306 m. The temperature of the fluidization gas was measured at several different positions, using PT100's (TI). The pressure was measured just before the gas turbine meter and in the air chamber using pressure transmitters, PTX1000 (PI). All the data collected from the pressure, temperature, humidity and gas turbine meter was logged in a data file using a LabVIEW program. In Figure 4.2 a picture of the setup is presented.

To make sure that the tracer particle could not exit the fluidized bed, a 100 μm mesh was placed on top of the column. In addition, a hydraulic lift was installed in order to move the fluidized bed up and down dependent on the section of the bed which was under investigation during a particular experiment. The humidified air was not enough to prevent electrostatics build up at the wall of the column when linear low density polyethylene (LLDPE) was used as bed material, therefore thin aluminum tape was placed on the inside of the PVC column, when the LLDPE particles were used, with which electrostatic effects could be sufficiently mitigated. Finally, to prevent the setup from vibrating during the experiments, stabilizers were used to fix the fluidized bed to its position.

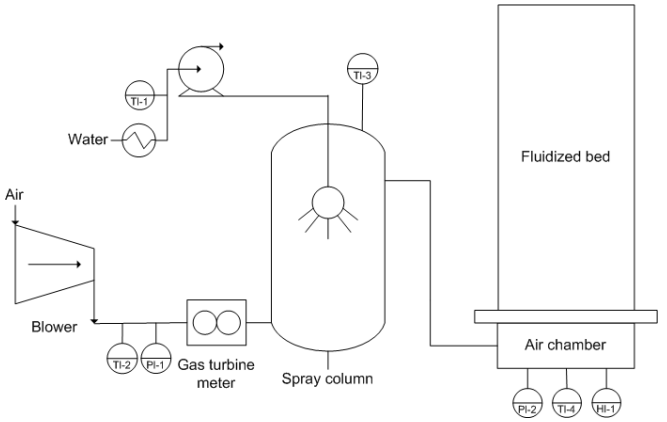

Figure 4.1: Flowsheet of the experimental setup.

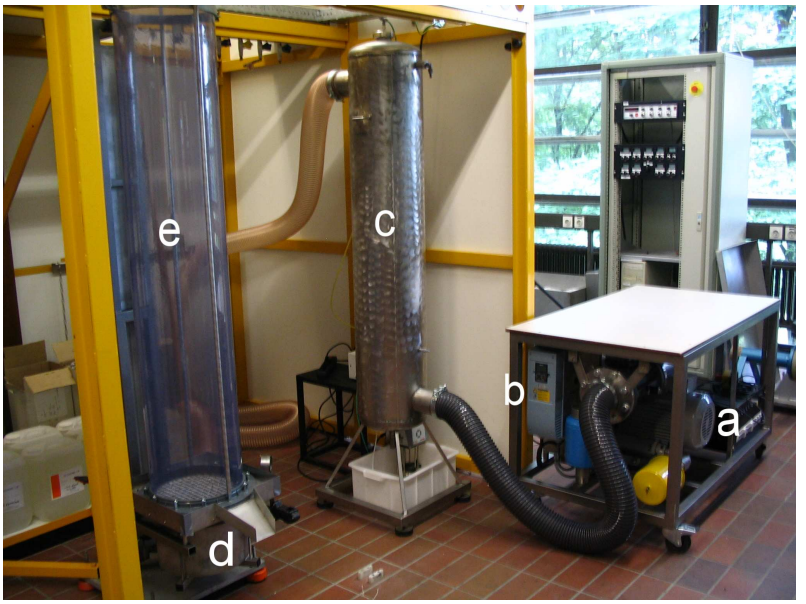

Figure 4.2: The experimental setup (a) side channel blower; (b) frequency controller; (c) spray column; (d) air-chamber; (e) fluidized bed.

Figure 4.3: A typical PEPT measurement, bed filled with glass beads, superficial gas velocity of 1.5 u_0/u_{mf} and packed bed aspect ratio of 1.

4.2.2 Measuring equipment

The PEPT camera at the University of Birmingham is an ADAC Forte (Parker et al. (2002)), and consists of two γ-camera heads. Each camera consists of a single sodium iodide crystal, with a thickness of 16 mm and an area of 590 x 470 mm^2. The sodium iodide crystal is optically coupled to an array of 55 photomultiplier tubes. When a photon hits the crystal, scintillation occurs and is registered by one of the photomultipliers, with which the position of the intersection with the γ-ray can be determined. During the measurements the detectors were 0.44 m apart.

4.2.3 Radioactive tracer particle

To track a particle with the PEPT technique, it is important that the properties of the tracer particle mimics the properties of the bed parti-

cles. The tracer particle which was used during the PEPT experiments was taken from the bed material, and therefore mimics the particles in the emulsion phase exactly.

For PEPT experiments, radioactive tracer particles are used which nuclei contain more protons than needed for its stability, therefore the particles decay by transforming a proton into a neutron under the emission of a positron. When the positron leaves the tracer particle, it rapidly annihilates with an electron, producing a pair of 511 keV γ-rays which are emitted almost exactly back-to-back (Parker et al. (1993)).

The tracer particles used during these measurements were not activated by direct activation, but by an activation technique which has been developed at the University of Birmingham (Fan et al. (2006a)). This technique involves a surface modification via the introduction of metallic ions on the surface of the tracer particle. $^{18}F^-$ anions will absorb/bind with the metallic ions on the solid surface, creating a radioactive charge. The absorption of ^{18}F is achieved by placing the tracer particle in activated water and shake it for a certain time. The oxygen atoms in the water were activated in a ^3He beam which was generated by a cyclotron $\left(^{16}O + {}^3\text{He} \longrightarrow {}^{18}\text{F} + \text{neutron}\right)$. Before performing the experiment the activity of the tracer particle was measured. The strength of the tracer particle varied between the 600 - 1000 μCi. The half-live of the ^{18}F is approximately 110 minutes. For more information om the activation of the particle, the interested reader is referred to Fan et al. (2006a) and Fan et al. (2006b), where a complete description of the developed activation technique at the University of Birmingham is given.

4.2.4 Particle reconstruction

Although in theory, two back-to-back events would be sufficient to determine the particle position, there are two reasons why this is not the case. The first reason is that one or both γ-rays of the pair can have undergone Compton scattering before the γ-ray has reached the detector, and the second reason is that the two detected γ-rays do not originate from the same positron annihilation event, but from two different events.

The location algorithm to determine the position of the tracer particle

uses an iterative approach, in which the position of the tracer particle is first calculated using a predefined number of events. The γ-ray pairs passing the furthest away from the particle position are disregarded and the position of the tracer particle is recalculated. This is repeated until all the corrupted events have been disregarded. In addition, the algorithm takes the decrease of activity of the particle during the measurement into account. For more details on the reconstruction technique, the interested reader is referred to Parker et al. (1993).

The primary output of the PEPT measurements consists of the position of the particle in the x, y and z-position as function of time. At the edges of the detectors, the difference in slope between the back-to-back γ-rays is small. Therefore, the accuracy of the point of intersection in those locations is reduced, and consequently, the extent of noise is increased. In the experiments with a higher aspect ratio, the PEPT detectors could only cover a part of the bed, and the tracer particle sometimes left the field of view of the detectors. In these cases, the velocity of the particle leaving the field of view and the velocity of the particle entering the field of view were disregarded.

Finally, the particle velocity is calculated using the average particle velocity over six subsequent particle locations (because of the high temporal resolution). The velocity is subsequently assigned to the cell containing the average position of the six particle positions, which was sufficient to determine time-averaged solids velocity profiles.

4.2.5 Experimental settings

One measurement was conducted for approximately 2.5 - 3 hours. The superficial gas velocity was varied between the 1.5 and 3.5 u_0/u_{mf} and the aspect ratio has been varied between 1 and 1.5. Two different particles types were used in the experiments, glass beads and linear low density polyethylene (LLDPE), both particle types were also used in chapter 2. The glass beads were purchased from Sigmund and Lindner and the particle size ranged from 400 to 600 μm. The density of the glass particles is 2500 $kg.m^{-3}$ and the minimum fluidization velocity has been experimentally determined to be 0.18 $m.s^{-1}$ via the pressure drop versus

Table 4.1: Experimental settings used in the PEPT experiments.

Parameter	
Bed material	Glass / LLDPE
Material density ρ_s $\left[kg.m^{-3}\right]$	2500 / 800
Minimum fluidization velocity u_{mf} $\left[m.s^{-1}\right]$	0.18 / 0.24
Superficial gas velocity u_0/u_{mf} $[-]$	1.5-3.5
Bed diameter d_{bed} $[m]$	0.30
Packed bed height $[m]$	0.30-0.45
Particle size distribution glass beads $[\mu m]$	400-600
Particle size distribution LLDPE $[\mu m]$	1000-1300

velocity method, see Kunii and Levenspiel (1991). The second particle type is linear low density polyethylene (LLDPE), courteously provided by LyondellBasell. The original LLDPE particles had a broad particle size distribution; therefore, the particles were sieved to obtain a narrow particle size distribution. The particle size for the LLDPE particles after sieving ranged from 1000 to 1300 μm, yielding an experimental minimum fluidization velocity of 0.24 $m.s^{-1}$. According to Glicksman (1984), when keeping the ratio Ar/Re_{mf} the same for both bed materials, the dynamics should remain the same in the fluidized bed. The ratio Ar/Re_{mf} for glass beds is 1.73×10^3 and for the LLDPE particles is 1.76×10^3. The experimental settings have been summarized in Table 4.1.

The humidity of the fluidization agent for the glass beads was set at 80% to prevent electrostatic build-up in the fluidized bed. For the experiments with LLDPE the internal wall of the vessel was partly covered with very thin aluminum tape and the humidity was set to 60-70%. The experiments with an aspect ratio of 1 could be obtained on basis of a single PEPT experiment, however, when the aspect ratio was increased to 1.5, the measurement had to be cnducted in two steps and subsequently combined in a post-processing step. The field of view of the detectors had an overlap of approximately 0.21 m during the two measurements to reduce the error in the measurement at the edge of the detectors.

4.2.6 Experimental procedure

The following steps were used during the start-up of the experiments. First, the tracer particle was prepared. The column was filled with the desired bed material to reach the desired (packed) bed height and subsequently the superficial gas velocity was slowly increased to the desired superficial gas velocity, followed by, starting the PEPT detectors and the introduction of the tracer particle into the fluidized bed. During the introduction of the tracer, the gas flow was turned off. After the tracer particle was introduced in the fluidized bed, the gas flow was again slowly increased until the desired fluidization velocity was reached and finally the PEPT measurement was started. In Figure 4.3 a picture of the bed and PEPT equipment is shown during a measurement is shown.

4.3 Results and discussion

In this section, the results of the PEPT measurements are presented and discussed. First the reproducibility of the PEPT measurements is assessed, followed by a description and discussion of the PEPT results for different superficial gas velocities and for the two types of bed materials. Finally, the influence of the aspect ratio is investigated and discussed.

Reproducibility

To investigate the reproducibility of the PEPT measurements, an experiment at a superficial gas velocity of 2.5 u_0/u_{mf} has been repeated. The fluidized bed was filled with LLDPE particles and the packed bed aspect ratio was 1. The results of the azimuthally and time-averaged axial emulsion phase velocity profiles at three different heights above the distributor are compared in Figure 4.4a. It can be concluded from this figure, that the reproducibility of the PEPT experiments at all three heights above the distributor is quite satisfactory. Besides the reproducibility of the PEPT measurements, it was investigated if the measuring time of the PEPT measurement was sufficiently long to obtain converged time-averaged solids velocities. Therefore, the experimental data of one of the above experiments was reprocessed, where the last 2500 seconds were

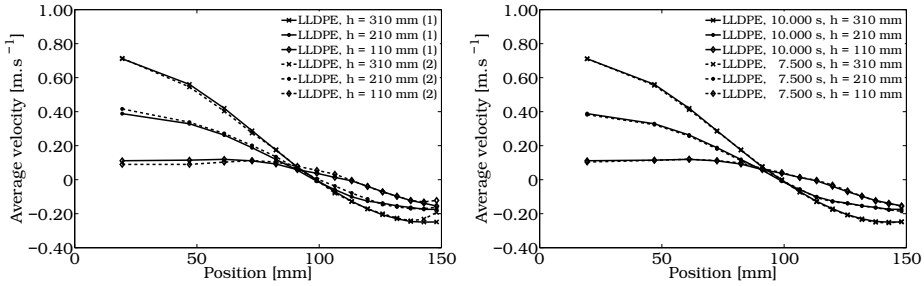

Figure 4.4: (a) Reproducibility of the PEPT experiments, azimuthally and time-averaged lateral profiles of the axial solids velocity at three different heights above the distributor; (b) influence of the measuring time (10.000 and 7.500 s). The superficial gas velocity was 2.5 u_0/u_{mf}, the fluidized was filled with LLDPE particles up to a packed bed height of 0.30 m.

disregarded. Figure 4.4b shows that the measuring time used for the PEPT measurements was indeed sufficiently long to obtain converged time-averaged solids velocity profiles.

Influence of the superficial gas velocity and bed material

Next, the influence of the superficial gas velocity and type of bed material on the azimuthally and time-averaged solids velocity profiles are presented in Figure 4.5 and 4.6.

It can be seen from these figures that at low superficial gas velocities, two distinct vortices appear above each other for both the glass beads and the LLDPE particles. When the superficial gas velocity is increased, the lower vortex decreases in size and at a higher superficial gas velocity, the lower vortex completely disappears while the top vortex spans the entire length of the fluidized bed were the center of the vortex is situated in the top half of the bed. The location of the center of the top vortex is practically the same for both particle types, however the difference in behavior between the glass beads and the LLDPE particles is that in the fluidized bed filled with the LLDPE particles the lower vortex disappears

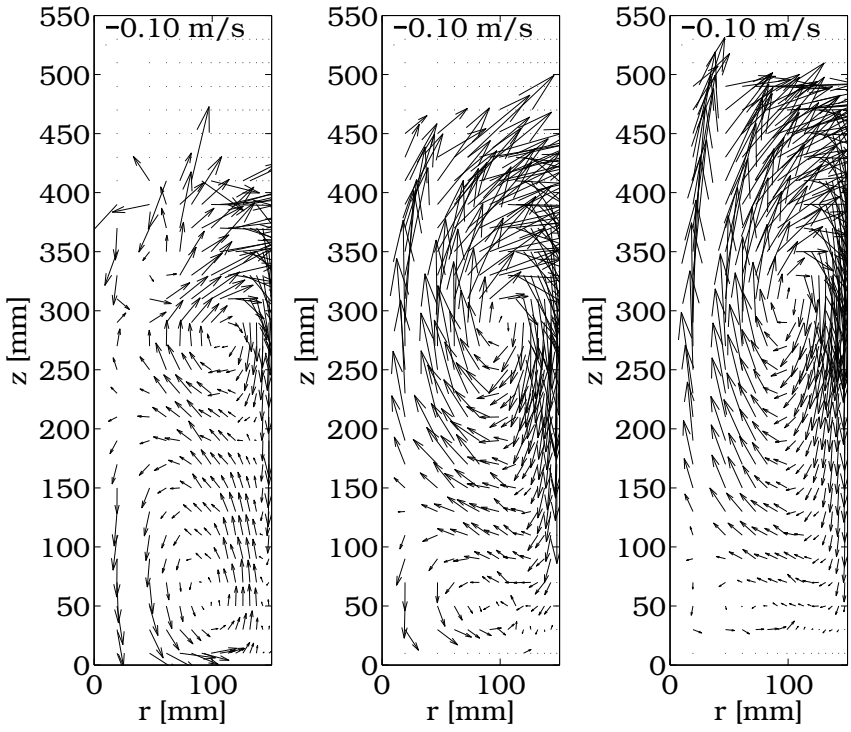

Figure 4.5: Azimuthally and time-averaged solids velocity profiles using glass beads for different superficial gas velocities, packed bed height was 0.30 m, particle size was 400 - 600 μm, superficial gas velocity was (a) 1.5 u_0/u_{mf}; (b) 2.5 u_0/u_{mf}; (c) 3.5 u_0/u_{mf}.

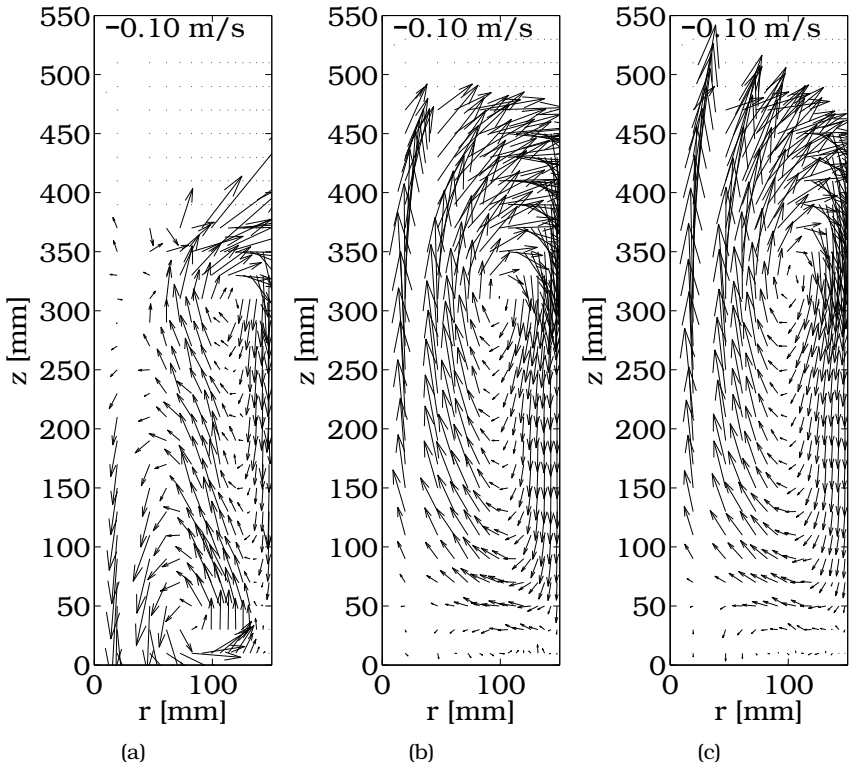

Figure 4.6: Azimuthally and time-averaged solids velocity profiles using LLDPE particles for different superficial gas velocities, packed bed height was 0.30 m, particle size was 1000 - 1300 μm, superficial gas velocity was (a) 1.5 u_0/u_{mf}; (b) 2.5 u_0/u_{mf}; (d) 3.5 u_0/u_{mf}.

already at a lower superficial gas velocity, and that the time-averaged upward velocity in the center of the bed is much higher (see also Figure 4.7)

These particle flow patterns indicate that at low superficial gas velocity the bubbles are formed at the walls of the fluidized bed. The bubbles grow and move toward the center of the fluidized bed due to bubble coalescence. However at 1.5 u_0/u_{mf}, the bubbles which are formed at the bottom do not traverse all the way to the center, creating a downward movement of the particles in the center of the fluidized bed just above the distributor plate. At 2.5 u_0/u_{mf} the bubbles generated at the bottom do on average traverse towards the center of the bed, for the glass beads at 100-150 *mm* above the distributor and for the LLDPE particles at 50 *mm* above the distributor. When the superficial gas velocity is increased, more bubbles are formed and the bubbles are larger, which results in a faster coalesce and thus a larger lateral velocity toward the center of the column, which agrees with the results presented in chapter 2. For 3.5 u_0/u_{mf} this lateral bubble movement is even more pronounced, resulting in a single vortex spanning from the bottom to the top of the fluidized bed. The behavior of the solids and bubble phase displayed in these measurements agrees well with results published in literature, see for example Kunii and Levenspiel (1991) or Stein et al. (2000).

Note that at the top of the column, the velocity vectors are not as smooth as in the rest of the bed, especially at lower superficial gas velocities. This is caused by the fact the particles at the top of the bed display a much more pronounced dynamic behavior, where, particles are continuously ejected from the fluidized bed which would require much longer measurement time to capture the time-averaged profiles accurately.

In Figure 4.7 the lateral profiles of the time-averaged axial solids velocity at three different heights above the distributor are given. On the left hand side of the figure, the results at three different superficial gas velocities for the glass beads are given and on the right hand side, the results for the LLDPE particles are given at the same fluidization velocity. When comparing the time-averaged lateral profiles of the axial solids velocity at the same superficial gas velocity, the shape of the graphs are

quite similar for the glass beads and LLDPE particles, however, the particles in the LLDPE filled fluidized bed have a significant larger upward time-averaged axial solids velocity in the center of the bed (note the difference in scale in the figures).

Furthermore, when the results of the glass beads and LLDPE particles are compared at the same u_0/u_{mf}, it becomes clear that the area in which an overall upward and downward movement of the particles is measured (i.e. the intersection of the curves is located at the same lateral position), is quite similar for both the glass beads and the LLDPE particles. The downward axial velocity of the particles is slightly higher when LLDPE particles are used as bed material compared to the glass beads, however, the upward solids velocity of the LLDPE particles is significantly higher than the upward axial solids velocity of the glass beads. From the continuity equation it can be concluded that the core of the bed filled with LLDPE has to have a lower density than the core of the bed when it was filled with glass beads. The lower density in the fluidized bed filled with LLDPE particles has to be caused by the larger bubbles (bubble hold-up) in the center of the fluidized bed, as shown in chapter 2. Using DIA it was shown that the average bubble size in the fluidized bed filled with LLDPE was indeed larger bubbles than in the fluidized bed filled with glass beads.

Moslemian et al. (1992) used CARPT to investigate the circulation patterns in bubbling fluidized beds and found that for different superficial velocities the transition from up- to down-flow was at approximately the same lateral position in the fluidized bed. In addition, Stein et al. (2000) also used PEPT to investigated the macroscopic circulation patterns in a bubbling fluidized bed, they plotted the up flow and down flow of the particles separately and found that the up flow in a bubbling fluidized bed occurred at $r/R = 0 - 0.27$ and the down flow was mainly achieved at $r/R = 0.7 - 1$. Up- and down-flow was mainly achieved at the intermediate region. Both the findings of Moslemian et al. (1992) and Stein et al. (2000) agree well with the PEPT measurements presented in this chapter. The transition between the up- and down-flow at higher superficial gas velocities (2.5-3.5 u_0/u_{mf}) was found to be between

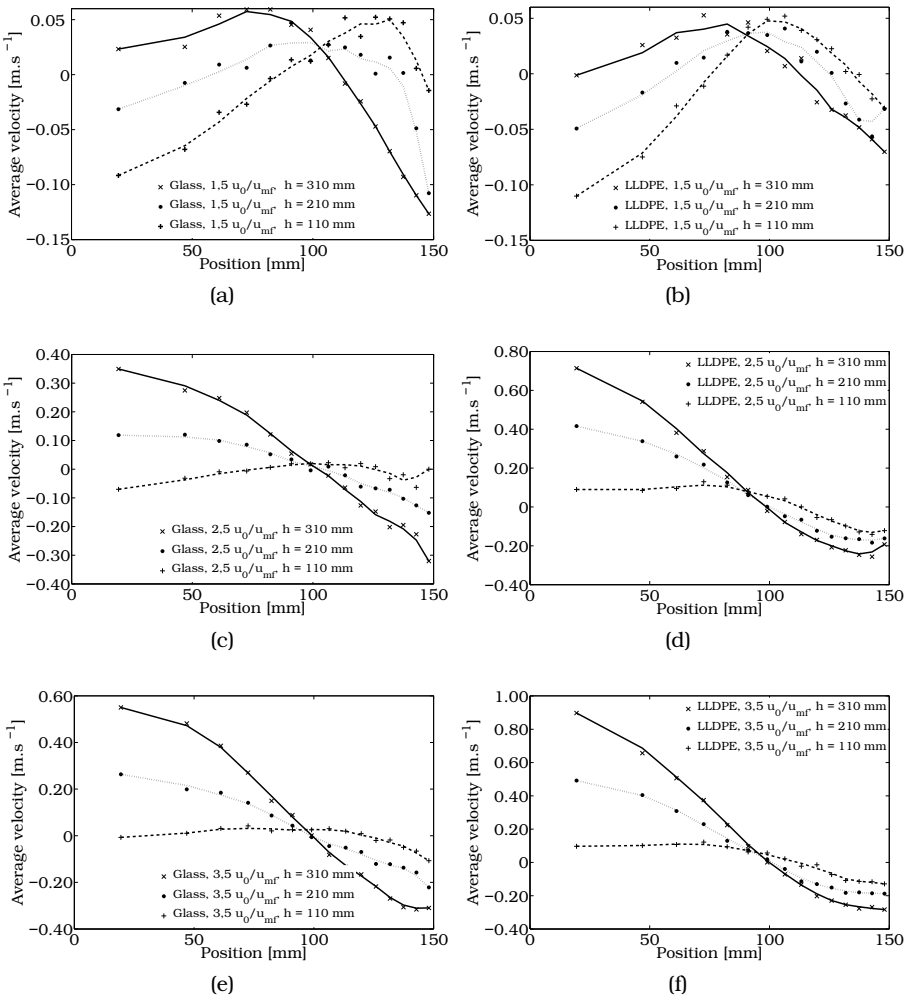

Figure 4.7: Azimuthally and time-averaged lateral profiles of the axial solids velocity at three different heights above the distributor plate, the packed bed height was 0.30 m, the bed was filled with glass beads or LLDPE particles, the superficial gas velocity was (a) 1.5 u_0/u_{mf} glass; (b) 1.5 u_0/u_{mf} LLDPE; (c) 2.5 u_0/u_{mf} glass; (d) 2.5 u_0/u_{mf} LLDPE; (e) 3.5 u_0/u_{mf} glass; (f) 3.5 u_0/u_{mf} LLDPE.

$r/R = 0.6 - 0.66$.

The particularly interesting finding in the chapter is that fluidized beds with particles of the ratio Ar/Re_{mf} exhibit significantly different axial solids velocities in the center of the fluidized bed, which is attributed to different bubble properties caused by differences in the particles collisional properties, see chapter 2 and 3).

Influence of the bed aspect ratio

To investigate the influence of the bed aspect ratio, several additional experiments have been carried out with a packed bed height of 0.45 m, i.e. an bed aspect ratio of 1.5. The superficial gas velocity was varied between 2.5 and 3.5 u_0/u_{mf}. The results of these experiments will be discussed in this paragraph. In Figures 4.8 and 4.9 the azimuthally and time-averaged solids velocities for respectively the glass beads and the LLDPE particles are compared for the two bed aspect ratios.

From these figures it can be observed that for both bed aspect ratios two vortices appear above each other in the fluidized bed, where the lower vortex disappears at increasing superficial gas velocity and that the vortex in the fluidized bed filled with LLDPE particles is much more pronounced than the fluidized bed filled with glass beads. The position of the center of the lower vortex is similar for the bed with a bed aspect ratio of 1.5 as the position of the lower vortex in the fluidized bed with a bed aspect ratio of 1. This indicates that the bubble behavior in the lower part of the fluidized bed for both bed aspect ratios is quite similar, i.e. the bubbles will move with the same lateral velocity to the center of the fluidized bed. The top vortex in the fluidized bed with aspect ratio 1.5 is more stretched and the center of the vortex is situated at a higher position in the fluidized bed.

In Figure 4.10 the azimuthally and time-averaged lateral profiles of the solids phase velocity for the different superficial gas velocities, bed aspect ratios and bed materials are presented. Where on the right hand side of the figure, the results of the glass beads at different aspect ratios are presented and on the right hand side the results of the LLDPE particles. The solid lines indicate the results at bed aspect ratio 1 and the

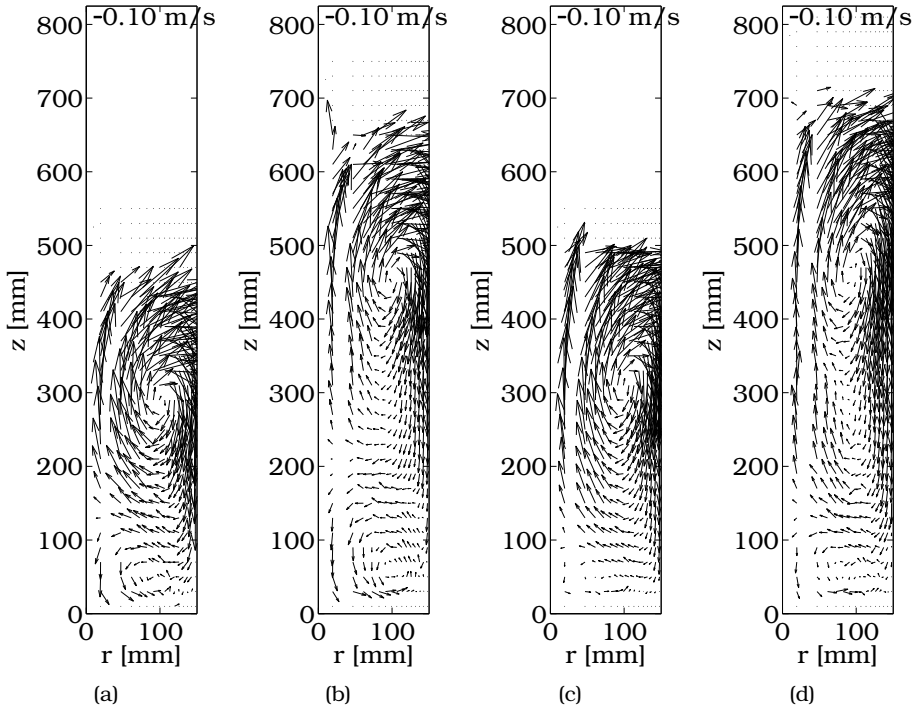

Figure 4.8: Azimuthally and time-averaged solids velocity measured with PEPT, the packed bed height was 0.30 and 0.45 m and the bed material was glass beads, the superficial gas velocity was (a) Aspect ratio 1, 2.5 u_0/u_{mf}; (b) Aspect ratio 1.5, 2.5 u_0/u_{mf}; (c) Aspect ratio 1, 3.5 u_0/u_{mf}; (d) Aspect ratio 1.5, 3.5 u_0/u_{mf};

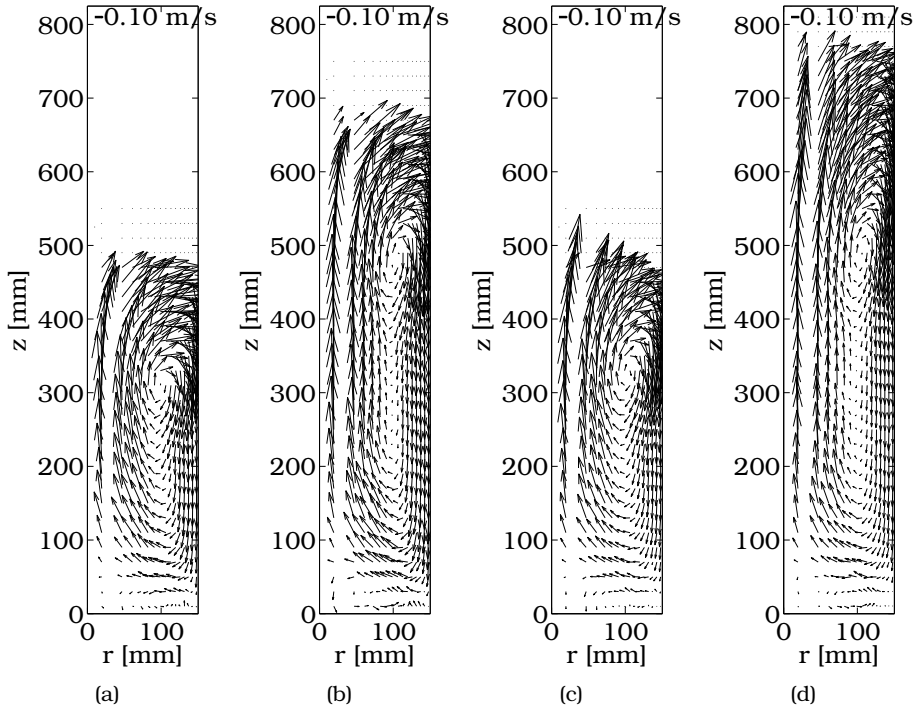

Figure 4.9: Azimuthally and time-averaged solids velocity measured with PEPT, the packed bed height was 0.30 and 0.45 m and the bed material was LLDPE, the superficial gas velocity was (a) Aspect ratio 1, 2.5 u_0/u_{mf}; (b) Aspect ratio 1.5, 2.5 u_0/u_{mf}; (c) Aspect ratio 1, 3.5 u_0/u_{mf}; (d) Aspect ratio 1.5, 3.5 u_0/u_{mf};

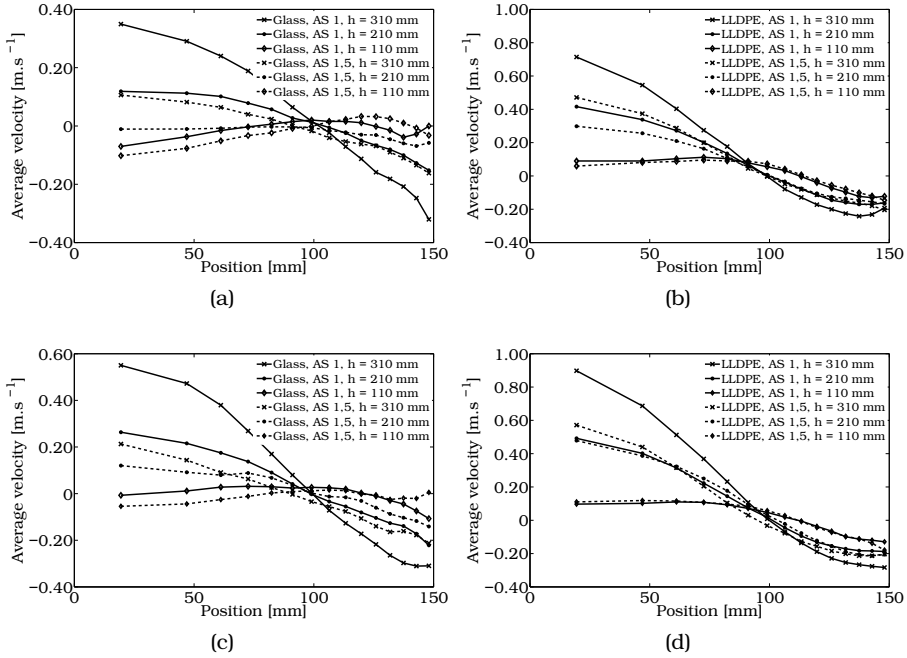

Figure 4.10: Influence of the bed aspect ration on the azimuthally and time-averaged lateral profiles of the axial emulsion phase velocity at three heights above the distributor (a) glass beads at 2.5 u_0/u_{mf}; (b) glass beads at 3.5 u_0/u_{mf}; (c) LLDPE at 2.5 u_0/u_{mf}; (d) LLDPE at 3.5 u_0/u_{mf}.

dashed line indicate the results for the bed aspect ratio of 1.5. The averaged axial velocity is compared at the same three heights (110, 210 and 310 *mm*) above the distributor in Figure 4.10a till Figure 4.10d. It can be observed that the solids velocity at 110 *mm* above the distributor for all bed materials and conditions is basically the same for both bed aspect ratios. At higher positions in the bed, there is a large deviation between the time-averaged solids phase velocities for both bed materials. This does not agree with the finding in chapter 2, where it was shown that the number-averaged solids velocity was not a function of the bed height when comparing at the same distance above the distributor.

The azimuthally and time-averaged lateral profiles of the axial solids

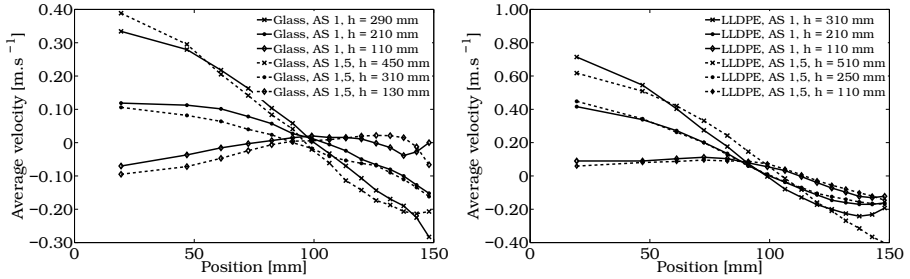

(a) (b)

Figure 4.11: Comparison of the azimuthally and time-averaged lateral profiles of the axial emulsion phase velocity at three different heights above the distributor (a) glass at 2.5 u_0/u_{mf}; (b) LLDPE at 2.5 u_0/u_{mf}.

velocity at approximately the same position (relative to the center) in the vortex are compared in Figure 4.11a and Figure 4.11b. In this figure the average axial velocity at a superficial gas velocity of 2.5 u_0/u_{mf} is compared at the same three position in the vortex. From this figure it becomes clear that the time-averaged solids velocity is almost the same.

4.4 Conclusions

In this chapter the solids motion in a three dimensional fluidized bed with an inner diameter of 0.306 m has been investigated experimentally using PEPT. Azimuthally and time-averaged solids velocity profiles have been obtained for different superficial gas velocities, bed materials and packed bed aspect ratios.

Glass beads (400-600 μm) and LLDPE particles (1000-1300 μm), having more or less the same ratio of Ar/Re_{mf} and showing Geldart B type behavior, have been used.

First, it was shown that the PEPT measuring technique produces well reproducible results and the measuring time was sufficiently long to obtain the converged time-averaged emulsion phase velocity profiles.

At low superficial gas velocities, two distinct vortices are formed above each other in the fluidized bed for both bed materials, however,

when the superficial gas velocity is increased, the lower vortex disappears and the top vortex spans over the entire length of the fluidized bed were the center of the vortex was situated in the top half of the fluidized bed. The lower vortex disappears at a lower superficial gas velocity when the fluidized bed was filled with LLDPE particles, indicating that the bubbles formed at the walls of the fluidized bed traverses faster towards the center than when the fluidized bed was filled with glass beads. Moreover, the average axial solids velocity in the center of the fluidized bed filled with LLDPE is much higher than when the bed was filled with glass beads, which was also found in chapter 2, were the number-averaged solids velocity was measured using Particle Image Velocimetry combined with Digital Image Analysis. This is probably related to the larger average bubble diameter in the fluidized bed filled with LLDPE particles as could be seen in chapter 2, where the averaged bubble size was measured for a fluidized bed filled with glass beads and LLDPE particles with Digital Image Analysis. The difference in bubble properties can only be attributed to differences in the extent and manner of mechanical energy dissipation in the particle-particle interactions (coefficient of restitution and friction coefficient), which is supported by CFD computations, see chapter 3.

A comparison of the time-averaged solids flow behavior in a fluidized bed with a packed bed aspect ratio of 1 and 1.5 showed qualitatively the same behavior.

However, when comparing the time-average axial velocity at the same height in the fluidized beds with different aspect ratios, are not the same. The averaged axial solids velocity in the fluidized bed with an aspect ratio of 1 is higher than the averaged axial solids velocity in the fluidized bed with an aspect ratio of 1.5. When comparing the averaged solids velocities at the same relative position of the center of the vortex, the velocities do agree nicely with each other.

CHAPTER 5

Modeling of large scale fluidized bed reactors with the Discrete Bubble Model

ABSTRACT

To investigate the hydrodynamic behavior of industrial scale bubbling fluidized bed reactors, a 3D Discrete Bubble Model (DBM) has been used. In the DBM, an Euler-Lagrange model, the bubbles are treated as discrete elements and the bubble trajectories are tracked individually, while the emulsion phase is considered as a continuum and is described with the continuity and Navier-Stokes equations. The main advantage of the DBM is that it fully accounts for the two-way coupling, allowing computation of the prevailing macroscopic circulation patterns in large scale gas-fluidized beds. In this chapter, we have examined the effects of bubble-bubble interactions on the macro-scale velocity profiles using the DBM. It has been found that the extent of the macroscopic circulation is significantly increased by the bubble-bubble interaction forces.

5.1 Introduction

To describe the macroscopic circulation patterns in an industrial scale gas-sold fluidized bed reactor, several modeling approaches have been presented in literature. The first approach is an agent-based bubble model of Pannala et al. (2003, 2004). In this model, the bubbles rise through the fluidized bed according to its size and the model accounts for bubble coalescence. A disadvantage of this model is that it disregards the interaction between the bubble phase and the emulsion phase. Therefore it is unable to describe the emulsion phase behavior properly. The second approach is the Euler-Euler approach (continuum models). The main disadvantage of the continuum models is that the closures are not suitable for course grid simulations, therefore filtered Euler-Euler models have been introduced, see for example Igci et al. (2008). In this model, the equations for the drag force and the virtual mass force are filtered, by averaging over a predefined filter length. The influence of the micro structures have to be implemented in the model via constitutive equations, obtained via experiments or sub grid models. The fourth approach was introduced by Bokkers (2005), the Discrete Bubble Model (DBM). In the DBM, an Euler-Lagrange model, bubbles are modeled as discrete elements and are tracked individually with Newton's second law during their path through the emulsion phase. The emulsion phase is considered as a continuum, for which the continuity and Navier-Stokes equations are solved. In addition to bubble coalescence and break-up, also the two-way coupling between the bubbles and the emulsion phase can be fully accounted for.

In this chapter the effect of the wake acceleration due to bubble-bubble interactions will be investigated. When fluidizing a Geldart B type powder, the actual gas velocity exceeds the bubble velocity and correspondingly, a large part of the gas flows from bubble to bubble through the fluidized bed. This results in an increased rise velocity of the bubbles compared to the rise velocity of a single isolated bubble due to an additional apparent force acting on the bubble, referred to as the wake acceleration force. Pannala et al. (2003) and Pannala et al. (2004) used an empirical correlation for the magnitude of the modified bubble rise

velocity, and the bubble velocity was directed toward its closest leading bubble. To incorporate the wake acceleration force into the DBM, the bubble velocity results from a force balance where the momentum exchange with the emulsion phase is fully accounted for. Then the bubble velocity is subsequently adjusted to model the effects caused by the presence of the wake of leading bubbles, using the equations derived by Farrokhalaee (1979) based on potential flow theory. Here, multiple pair-wise interactions between leading and tailing bubbles are considered, where it has been assumed that the potential streams around one bubble are not affected by the presence of other neighboring bubbles.

In this chapter, the governing equations, together with their closures are presented, followed by the numerical implementation. Furthermore, the results of the simulations are presented and discussed. At the end of the chapter, the conclusions will be given.

5.2 Discrete Bubble Model

Although the DBM idealizes the bubbles as discrete perfect spheres in the collision detection algorithm, its strong advantage is that it fully accounts for the two-way coupling, i.e. the bubbles rising through the emulsion phase will affect the dynamics of the emulsion phase and, visa versa, the emulsion phase velocity patterns will be influenced by the drag exerted by the bubbles on the emulsion phase. Because all the bubbles are tracked individually, the DBM requires no a priori assumptions on the encounter frequency, an important factor determining the bubble coalescence rate. A full description of the DBM is given in this section, starting with both phases of the fluidized bed reactor, the emulsion and bubble phase, followed by the bubble-bubble interactions, the boundary conditions and finally the solution strategy.

5.2.1 Emulsion phase dynamics

The emulsion phase consists of a mixture of particles and gas and is regarded as the Eulerian part of the model. Therefore, the hydrodynamics of the emulsion phase are described using the continuity equation

and the volume-averaged Navier-Stokes equation, after Anderson and Jackson (1967).

$$\frac{\partial(\varepsilon_e \rho_e)}{\partial t} + \nabla \cdot (\varepsilon_e \rho_e \vec{u_e}) = 0 \tag{5.1}$$

$$\frac{\partial(\varepsilon_e \rho_e \vec{u_e})}{\partial t} + \nabla \cdot (\varepsilon_e \rho_e \vec{u_e} \vec{u_e}) = -\varepsilon_e \nabla p - \nabla \cdot (\varepsilon_e \tau_e) + \vec{S} + \varepsilon_e \rho_e \vec{g} \tag{5.2}$$

The porosity of the emulsion phase is represented by ε_e, ρ_e is the emulsion phase density and $\vec{g}$ is the gravitational acceleration. The momentum transfer between the bubble and emulsion phase is described by the source term, S, for more information about the source term, see section 5.2.4. It is assumed that the emulsion phase stress tensor, τ_e, obeys the Newtonian form, which is given by

$$\vec{\tau_e} = -\mu_e \left[\nabla \vec{u_e} + (\nabla \vec{u_e})^T - \frac{2}{3} \vec{I} (\nabla \vec{u_e}) \right] \tag{5.3}$$

where μ_e and I are represents respectively the emulsion phase shear viscosity and the unit tensor.

5.2.2 Bubble dynamics

In the DBM, the bubbles (gas phase) are regarded as the Lagrangian part of the CFD code, i.e. all the bubble trajectories are calculated by integrating Newton's second law of motion,

$$m_b \frac{d\vec{v_b}}{dt} = \sum \vec{F} = \vec{F_G} + \vec{F_P} + \vec{F_D} + \vec{F_{VM}} + \vec{F_{BB}} \tag{5.4}$$

where m_b and $\vec{v_b}$ denote the bubble mass and velocity. $\vec{F_G}$, $\vec{F_P}$, $\vec{F_D}$, $\vec{F_{VM}}$ and $\vec{F_{BB}}$ are respectively, the gravitational, pressure, drag, virtual mass (added mass) and bubble-bubble force. Closures for the forces are listed in Table 5.1, with the exception of the bubble-bubble force, which will be discussed in section 5.2.3.

The closure for the drag force, C_D, was determined by Bokkers et al. (2006) to be 2.64, derived from the terminal rise velocity of a single isolated bubble. The virtual mass force closure, C_{VM}, was assumed to be 0.5 (Bokkers et al. (2006)). Furthermore, it has been assumed that

Table 5.1: Forces in the Discrete Bubble Model

Force	**Equation**	**Closure**
Gravitational	$\vec{F}_G = \rho_g V_b \vec{g}$	-
Pressure	$\vec{F}_P = -V_b \nabla P$	-
Drag	$\vec{F}_D = -\frac{1}{2} C_D \rho_e \pi R_b^2 \left\|\vec{v} - \vec{u}\right\| (\vec{v} - \vec{u})$	$C_D = 2.64^{\dagger}$
Virtual mass	$\vec{F}_{VM} = -C_{VM} \rho_e V_b \left(\frac{D_b \vec{v}}{D_b t} - \frac{D_e \vec{u}}{D_e t}\right)$	$C_{VM} = 0.5^{\dagger\dagger}$
Bubble-Bubble	See section 5.2.3	-

† After Odar and Hamilton (1964), †† after Auton (1983)

there is no net gas exchange between the emulsion and bubble phase and that bubbles only grow due to coalescence with other bubbles.

5.2.3 Bubble-bubble interactions

In the DBM, two different types of bubble-bubble interactions are distinguished, namely bubble coalescence and the acceleration of a bubble in the wake of a leading bubble, i.e. the wake acceleration force.

Bubble coalescence

The implementation of bubble coalescence in the DBM is a simplified model which assumes a 100% coalescence efficiency for a bubble-bubble encounter, if the bubble diameter is smaller than a pre-described maximum bubble diameter. When a bubble collides with another bubble and would yield a bubble which is larger than the maximum bubble diameter after coalescence, the bubbles are assumed not to coalesce but collide elastically, approximating the dynamic equilibrium between bubble break-up and bubble coalescence. Bokkers et al. (2006) investigated the influence of the bubble coalescence. They performed two DBM simulations, where in the first simulation, the bubbles were allowed to coalesce and in the second simulation, the bubbles were not allowed to coalesce. In the case with coalescence, the bubbles moved toward the center of the fluidized bed, whereas in the simulation without coalescence the complete fluidized bed was filled with bubbles. In addition, in the case

with coalescence, the time-averaged axial emulsion phase velocity kept increasing in the axial direction until the top of the fluidized bed, where in the case without coalescence, the time-averaged axial emulsion phase velocity reached a constant value.

Wake acceleration force

It is generally accepted that for fluidization of Geldart B type solids, a large part of the gas is flowing from bubble to bubble through the bed. Due to this movement of the gas, an additional force is exerted on the bubbles, here referred to as the wake acceleration force. This force results in a higher bubble velocity and in a possible lateral movement of the bubbles inside a fluidized bed reactor.

To include the wake acceleration force into their simulations, Krishna and van Baten (2001) derived an empirical relation of the influence of the wake acceleration factor. They used the Davies-Taylor relation for a single bubble rising through the fluidized bed, extended with the size factor, SF, suggested by Collins (1967) for gas-liquid systems and the wake acceleration factor, AF.

$$v = 0.71\sqrt{g d_b}\,(SF)\,(AF) \tag{5.5}$$

where

$$SF = \begin{cases} 1 & \text{for } \dfrac{d_b}{D_T} < 0.125 \\ 1.13e^{-\dfrac{d_b}{D_T}} & \text{for } 0.125 < \dfrac{d_b}{D_T} < 0.6 \\ 0.496\sqrt{\dfrac{D_T}{d_b}} & \text{for } \dfrac{d_b}{D_T} > 0.6 \end{cases} \tag{5.6}$$

$$AF = 1.64 + 2.7722\left(u_0 - u_{df}\right) \tag{5.7}$$

The acceleration factor was the best fit for their experimental data set. Krishna and van Baten (2001) found that the bubble rise velocity was increased by 1.5 to 3 times in comparison to a single isolated bubble rising through a fluidized bed, showing the importance of the bubble-bubble interaction.

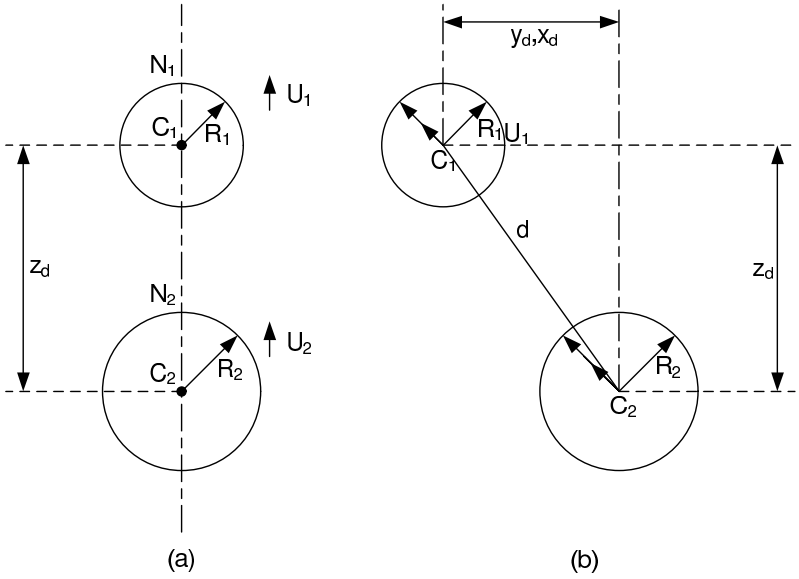

Figure 5.1: Grafical representation of the wake acceleration model, after Clift and Grace (1985), (a) Vertically aligned bubbles (b) non vertically aligned bubbles

Another approach to determine the wake acceleration of bubbles in the fluidized bed was suggested by a.o. Clift and Grace (1970) and Clift and Grace (1971). Clift and Grace investigated the interaction between bubble pairs, vertically and non-vertically aligned and bubbles with different diameters. The basic idea of this approach is that the velocity of the tailing bubble can be approximated by adding the emulsion phase velocity at the top of the tailing bubble, that the emulsion would have if the tailing bubble were absent, see Figure 5.1. The emulsion phase velocity can be calculated by the potential flow around a bubble. Based on the model suggested by Clift and Grace (1971), Farrokhalaee (1979) proposed a simplification of the wake acceleration model. Farrokhalaee stated that the bubble velocity v of the tailing bubble i has a very small effect on the bubble velocity of the leading bubble j and could therefore be neglected. Clift and Grace (1985) investigated which wake accelera-

tion model described the experimental results best by comparing several different wake acceleration models with their experimental data. They concluded that the model suggested by Farrokhalaee was at least as accurate as the more sophisticated models, which did take the influence of the tailing bubble on the leading bubble into account. Therefore, the wake acceleration model suggested by Farrokhalaee has been implemented in the DBM. The rise velocity of the bubble including the wake acceleration force, $\vec{v}_i^*$, is calculated using

$$v_i^* = \vec{v}_i + \sum_j^{N_{bub}} c_{i,j,x} v_{j,x} \tag{5.8}$$

where $\vec{v}_i$ is the velocity of the bubble under investigation if it were isolated, $c_{i,j}$ is the interaction coefficient and finally, $\vec{v}_j$ are the velocities of the all leading bubbles. The velocity of the bubble in the y- and z-direction is calculated in the same manner. The interaction coefficients can be calculated by, after Clift and Grace (1985).

$$c_{i,j,z} = \frac{\left[2((z_i - z_j) + R_i)^2 - \left(\sqrt{\Delta x^2 + \Delta y^2}\right)^2\right] R_j^3}{2\left[((z_i - z_j) + R_i)^2 + \left(\sqrt{\Delta x^2 + \Delta y^2}\right)^2\right]^{\frac{5}{2}}} \tag{5.9}$$

$$c_{i,j,x} = \left(\frac{x_i - x_j}{\sqrt{\Delta x^2 + \Delta y^2}}\right) m_{i,j} \tag{5.10}$$

$$c_{i,j,y} = \left(\frac{y_i - y_j}{\sqrt{\Delta x^2 + \Delta y^2}}\right) m_{i,j} \tag{5.11}$$

and

$$m_{i,j} = \frac{3R_j^3 \left((z_i - z_j) + R_i\right)\left(\sqrt{\Delta x^2 + \Delta y^2}\right)}{2\left[((z_i - z_j) + R_i)^2 + \left(\sqrt{\Delta x^2 + \Delta y^2}\right)^2\right]^{\frac{5}{2}}} \tag{5.12}$$

The wake acceleration has not been included in the momentum transfer to the emulsion phase, since the wake acceleration is modeled as a sub-grid phenomenon. Note that here the macroscopic circulation

patterns are of interest, and not the detailed velocity profile in the direct vicinity of a single bubble. Therefore, the wake effect is only incorporated as a bubble repositioning and not accounted for in the bubble force balance. The implementation of the wake acceleration in the DBM has been verified in Appendix 5.1.

5.2.4 Solution method

To solve the pressure and velocity fields for the emulsion phase, the SIMPLE algorithm is used. To evaluate the convective terms in the continuity and momentum equations, a second order accurate Barton scheme is used, whereas the standard second order central discretization is used for the diffusive terms. A first order implicit time integration is used to solve the force balance for every individual bubble in the fluidized bed.

The interaction between the bubble and the emulsion phase is calculated via a two-way coupling method. This means that the bubble phase affects the emulsion phase by the void fraction and the momentum transfer rate from the bubble to the emulsion phase, represented by the source term in the Navier-Stokes equation.

$$\vec{S} = -\frac{1}{V_{cell}} \sum_{\forall i \in cell} \left(\vec{F}_{D,i} + \vec{F}_{VM,i} \right) \tag{5.13}$$

Furthermore, the emulsion phase influences the bubbles via the slip velocity in the drag and virtual mass forces. Because the bubbles can grow larger than the grid size, the volume averaging technique cannot be applied, therefore a normalized polynomial distribution function is used to distribute the momentum over the surrounding cells and the same function is used to map the Eulerian information to the position of the bubble.

$$\begin{aligned} D\left(x_i - x_{i,b}\right) &= \frac{15}{16}\left[\frac{\left(x_i - x_{i,b}\right)^4}{n^5} - 2\frac{\left(x_i - x_{i,b}\right)^2}{n^3} + \frac{1}{n}\right] \\ -n &\leq \left(x_i - x_{i,b}\right) \leq +n \end{aligned} \tag{5.14}$$

Where D is the normalized polynomial distribution function and n is the width of the distribution window. The interested reader is referred

to the article by Deen et al. (2004), for more details on the distribution function.

5.2.5 Boundary conditions

The boundary conditions which are imposed on the walls utilize the flag concept by Kuipers et al. (1993). The boundaries are schematically presented in Figure 2 and the corresponding boundary conditions are given in Table 5.2. The prescribed pressure cells near the top of the column serve as inlet and outlet zones to accommodate for the changes in the emulsion phase volume when the bubbles enter or leave the column (Darmana et al. (2005)). During the initialization step of the simulation the pressure is set to the hydrostatic pressure in the reactor. The bubbles (with a constant predefined bubble diameter) enter the column via nozzles that are equally distributed over the bottom. When the simulation is started, the bubbles start at a randomly determined vertical z-coordinate, below the bottom of the column. This has been implemented in the DBM to prevent the occurrence of an undesired pressure wave in the column. The distance δ_b between the two centers of the two consecutive bubbles entering the fluidized bed at the same nozzle position is set to $2.5 \times R_b$. To calculate the velocity of the bubbles entering the column, the following equation is used

$$v_{z,enter} = \frac{\psi \delta_b A_t}{N_n V_b} \tag{5.15}$$

where ψ represents the visual bubble flow rate, in the DBM simulations a constant value of 0.65 (Hilligardt and Werther (1986)) has been used. A_t is the cross-sectional area, the number of nozzles is represented by N_n and the volume of the bubble is V_b.

When the bubble touches the top boundary of the column, the bubble is marked to be removed from the column. When this happens, the velocity and the inter phase momentum transfer to the emulsion phase are no longer updated and the bubble leaves the column with a constant velocity.

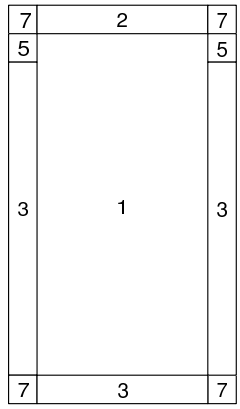

Figure 5.2: Flag matrix, after Kuipers et al. (1993).

Table 5.2: Cell flags and their corresponding boundary conditions

flag	**Boundary condition**
1	Interior cell, no boundary condition
2	Impermeable wall, free slip boundary
3	Impermeable wall, no slip boundary
5	Prescribed pressure cell, free slip boundary
7	Corner cell, no boundary condition

5.3 Results and Discussion

In this section, the results of the DBM are presented and discussed. First the influence of the bubble interaction model in a rectangular column will be presented and discussed. The verification of the implementation of the wake acceleration is presented in Appendix 5.1.

5.3.1 Influence of the wake acceleration model

The influence of the pair-wise bubble-wake interactions has been investigated by considering three cases: (a) case without bubble-wake interactions; (b) case with bubble-wake interactions, but only considering the binary interaction with its nearest leading neighbor; and (c) case

with bubble-wake interactions, accounting for binary interactions with all leading bubbles; in all these cases bubble coalescence was accounted for. The emulsion phase density and viscosity and also the gas phase density were set to values that are commonly encountered in polymerization fluidized bed reactors. Details on the simulation settings can be found in Table 5.3. Time-averaged velocity profiles were computed by averaging over 190 s, starting after 10 s to eliminate start-up effects. It has been verified that with these settings grid and time step independent results are obtained and that the time-averaging period is sufficiently long.

Table 5.3: Settings for DBM simulations for the investigation of the impact of the bubble-bubble interactions on the macroscopic circulation patterns in a bubbling fluidized bed.

Parameter	**Value**
Width x-direction [m]	1
Depth y-direction [m]	1
Height z-direction [m]	3
Grid cells (x,y,z)	20,20,60
Emulsion phase density [$kg.m^{-3}$]	400
Emulsion phase viscosity [$Pa.s$]	0.1
Gas density [$kg.m^{-3}$]	25
Initial bubble diameter [m]	0.08
Maximum bubble diameter [m]	0.40
Superficial gas velocity [$m.s^{-1}$]	0.25
Number of nozzles [-]	49
Time step flow solver [s]	5×10^{-3}
Time step bubbles [s]	5×10^{-4}
Simulation time [s]	200

In Figure 5.3 and Figure 5.4 snapshots of the bubbles and the time-averaged emulsion phase velocity vector plots are given for the three simulated cases. These figures clearly show the very large influence of the bubble-wake interactions on the average bubble size and the extent of solids circulation. When accounting for bubble-wake interactions, the bubble coalescence rate, especially at the bottom of the fluidized bed, is strongly enhanced, resulting in fewer, but larger and faster rising bub-

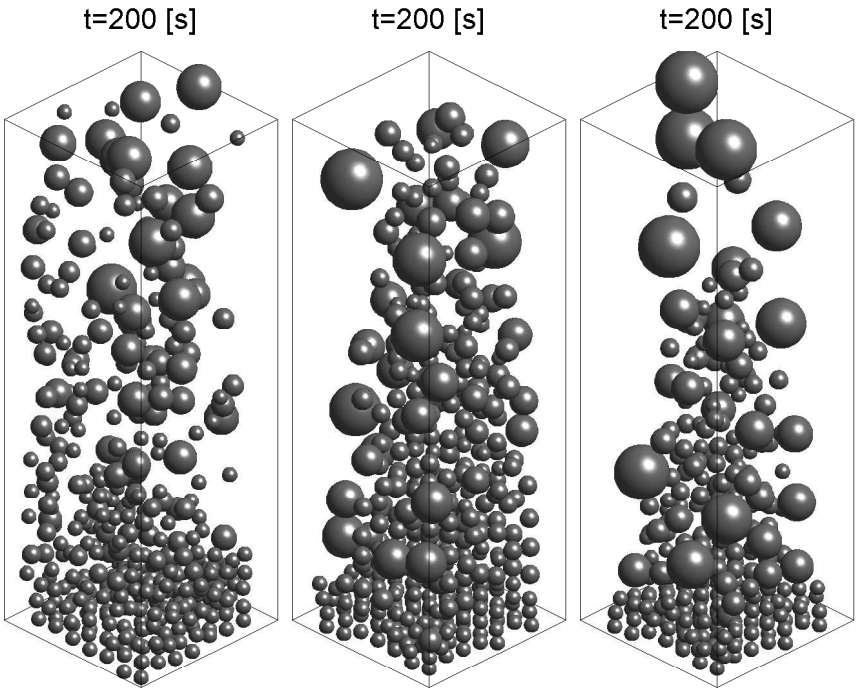

Figure 5.3: Snapshots of the bubbles after 200 s for the three cases: (a) case without bubble-wake interactions; (b) case with single binary bubble-wake interactions; (c) case with multiple binary bubble-wake interactions.

bles through the centre of the fluidized bed (which in its turn enhances the bubble encounter frequency). Also the time-averaged porosity plots (Figure 5.5) clearly show the increased tendency of the bubbles to move towards the center of the fluidized bed.

In Figure 5.6a the laterally averaged bubble diameter as function of the axial position in the fluidized bed is presented. The figure clearly shows, as could also have been observed qualitatively from Figure 5.3, that the wake-acceleration force has a very large influence on the average bubble diameter. From Figure 5.6b, showing the time-averaged

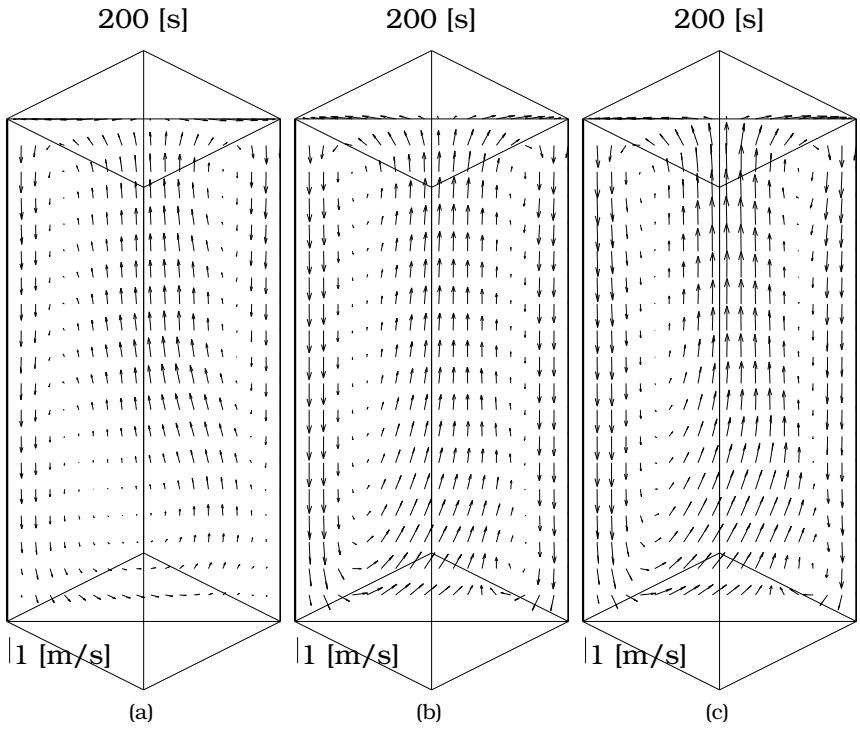

Figure 5.4: Time-averaged emulsion phase vector plots for the three cases: (a) case without bubble-wake interactions; (b) case with single binary bubble-wake interactions; (b) case with multiple binary bubble-wake interactions.

axial emulsion phase velocity profiles at about 2/3 of the bed height, the strongly increased solids circulation (strongly increased down flow near the walls) when accounting for bubble-wake interactions is evident. Because the wake effect is incorporated as a sub-grid phenomenon in the bubble repositioning and not directly in the bubble force balance, the increased average bubble size due to enhanced bubble coalescence as a result of the wake-acceleration force is the reason why the emulsion phase velocity increases as a function of the axial position in the bed. The figures also show that the effects of the bubble-wake inter-

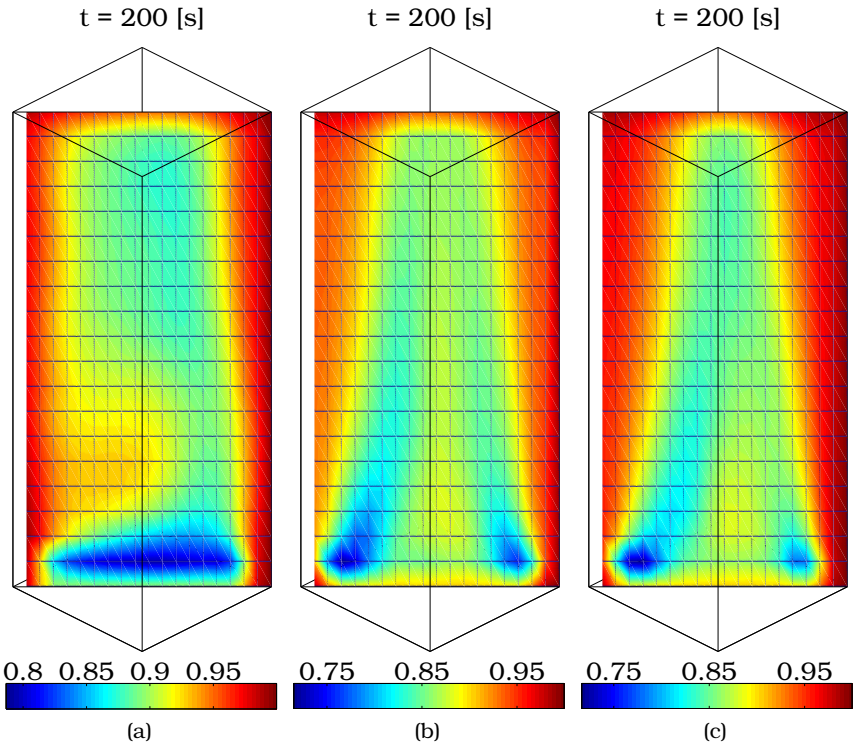

Figure 5.5: Time-averaged porosity plots: (a) case without bubble-wake interactions; (b) case with single binary bubble-wake interactions; (c) case with multiple binary bubble-wake interactions.

actions (increased bubble coalescence and solids circulation) are even more pronounced, when accounting for multiple bubble-wake interactions (case c) relative to single binary bubble-wake interactions (case b). In the case a small bubble is the leading bubble (i.e. the nearest bubble above), while a much larger bubble is very near, only the interaction with the small bubble is considered, while the interaction with the larger bubble is completely ignored, for case b. Therefore, in case c, where the bubble-wake interactions with all leading bubbles is taken into account, the bubble coalescence is strongly enhanced, resulting in

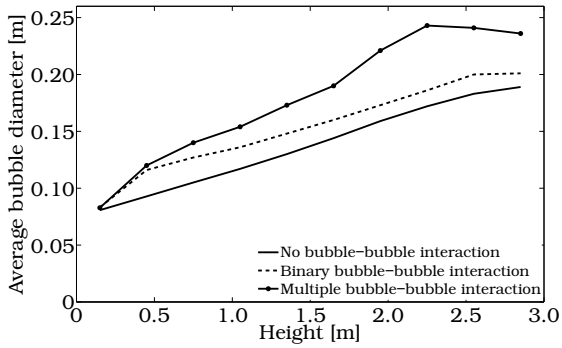

(a)

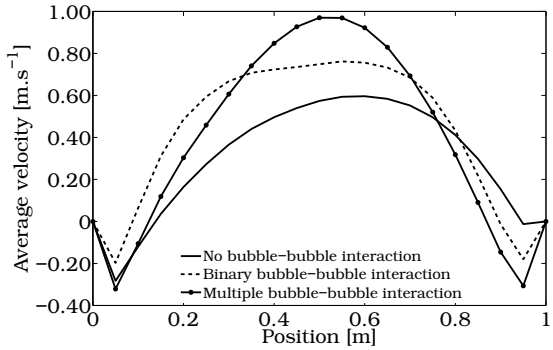

(b)

Figure 5.6: Influence of the bubble-bubble interactions on (a) the axial profile of the laterally averaged bubble diameter; (b) the lateral profile of the axial emulsion phase velocity at 2.1 m above the distributor.

an increased averaged bubble diameter and narrowed bubble size distribution. For case c, the average bubble rise velocity is about 1.6 times higher than the rise velocity of an isolated bubble, which corresponds quite reasonably to the findings of Krishna and van Baten (2001). According to the correlations proposed by Krishna and van Baten, based on experimental results on an air-FCC catalyst (Geldart A) system, the bubble velocity should be increased by a factor of 1.8 compared to the undisturbed bubble rise velocity due to the bubble-bubble interactions.

5.4 Conclusions

The effects of bubble-wake interactions on the macroscopic behavior of freely bubbling fluidized beds have been investigated with the DBM. It has been found that bubble coalescence and macro-scale solids circulation is strongly enhanced when single or multiple binary bubble-wake interactions are accounted for. It has been demonstrated that bubble-wake interactions with all leading bubbles should be taken into consideration (and not just the nearest leading bubble), to avoid missing important bubble-wake interactions in case the nearest leading bubble is a small bubble, while a much larger bubble is very near. Further model development on the bubble-bubble interactions taking multiple leading bubbles into account and more detailed experimental work to validate the DBM is required and ongoing.

Appendix 5.1: Verification of the wake acceleration

To verify the implementation of the wake acceleration model, a DBM simulation with three bubbles, which were not vertically aligned, has been performed in which the flow field was set to zero. In addition, the velocity and position of the three bubbles was determined analytically. The initial position and radius of the three bubbles are given in Table 5.4. To compare the analytical calculations and the DBM results, the

Table 5.4: Settings for the verification of the wake model

Parameter	**Value**
x-position [m]	0.50, 0.50, 0.50
y-position [m]	0.50, 0.54, 0.51
z-position [m]	0.48, 0.37, 0.26
Bubble radius [m]	0.04, 0.04, 0.04
Column dimensions [m]	1.00, 1.00, 1.00
Time-step bubble solver [s]	1.0×10^{-4}

y- and z-positions of the three bubbles are presented in Figure 5.7. For the top bubble only the z-position in Figure 5.7a is given because the y-position did not vary during the simulation except when the top two bubbles merged. It can be seen that after approximately 0.3 s the top and the middle bubble coalesce and the top bubble is repositioned to the center of mass of the two bubbles. In Figures 5.7b and 5.7c the y- and z-position of the middle bubble is given. The bubble positions calculated by the DBM correspond perfectly with the analytically calculated bubble positions. Finally, in Figures 5.7d and 5.7e the y- and z-position of the bottom bubble is given. The y-direction of the bottom bubble is first mainly influenced by the middle bubble. When the top two bubbles are merged, the y-movement of the bubble is influenced by the merged bubble. Again, the movement of the bottom bubble calculated by the DBM could be perfectly reproduced with the analytically calculated bubble positions. Note that when the bubble diameter is the same for all bubbles, and no wake acceleration was implemented, the bubbles would not have merged or been drawn together.

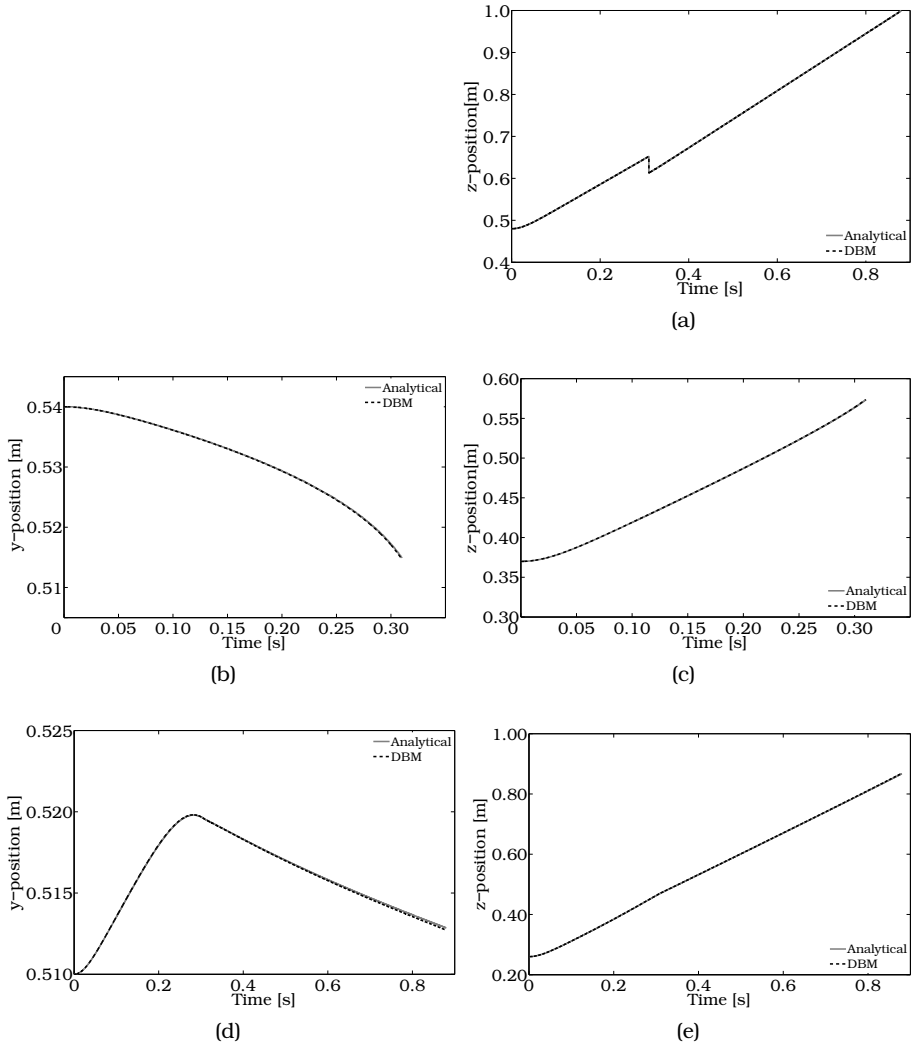

Figure 5.7: Comparison between the computed y- and z-positions of the three bubbles used to verify the wake acceleration model in the DBM, (a) z-position vs. time of the top bubble; (b) y-position vs. time of the middle bubble; (c) z-position vs. time of the middle bubble; (d) y-position vs. time of the bottom bubble; (e) z-position vs. time of the bottom bubble.

Epilogue

In this thesis the hydrodynamics of a bubbling gas-solid fluidized bed have been investigated. The novel approach is that characteristics of the bubble and emulsion phases were investigated simultaneously, which is required because of the influence of the bubble phase on the emulsion phase and vice versa. Using a novel approach (PIV/DIA) to measure non-intrusively both the instantaneous whole-field particle velocity profiles and the bubble properties simultaneously in a pseudo 2D-fluidized bed, filled with either LLDPE particles or glass beads with approximately the same minimum fluidization velocity, it was found that the bubbles grow to a larger size in the fluidized bed with LLPDE particles. However, the averaged bubble rise velocity as function of the equivalent bubble diameter was for both powders approximately the same. In correspondence to the larger bubble size, the time-averaged emulsion phase velocity circulation patterns were more pronounced in the bed containing the polymer particles. Furthermore, the visual bubble flow rate as function of the height was different for both powders, however, in agreement with results found in literature. In the currently applied DIA the porosity is cannot be measured and therefore the solids mass flux cannot be determined. In order to measure the porosity distribution in a pseudo-2D fluidized bed the DIA algorithm needs to be extended. Several authors have already measured the local porosity and therefore mass flux of the solids phase in the pseudo-2D fluidized beds, however these fluidized beds were filled with larger glass beads (particle diameter of 1.5 *mm*).

Subsequently the influence of the microscopic particle properties on the macroscopic circulation patterns and bubble properties was investigated using numerical (CFD) models. It was shown that the particle friction coefficient has a large influence on the hydrodynamics in a fluidized bed. From the minimum fluidization velocity to the size and shape of the bubbles and the axial solids velocity distribution in the lateral direction were studied. The influence of the restitution coefficient in the normal and tangential direction was found to be less pronounced than the influence of the particle friction coefficient. To simulate the LLDPE particles properly, the collisional properties of the LLDPE particles have to be measured. Especially the particle friction coefficient between particles and particles and the wall needs to be determined. In addition, the collisional model in the TFM with the Kinetic Theory of Granular Flow has to be extended in such a way that friction between particles and between particle and wall is taken into account.

To obtain information about the hydrodynamics in a 3D-fluidized bed, dedicated PEPT measurements have been performed. At lower superficial gas velocities, four distinct vortices appeared. When the superficial gas velocity was increased, the lower vortices reduced in size and finally were completely consumed by the top vortices. When LLDPE particles are used, this superficial gas velocity is lower than when glass beads are used. In addition, the time-averaged emulsion phase velocity of the LLDPE particles is higher at the same u_0/u_{mf} compared to the glass beads. When using PEPT, no direct information about the bubble phase is obtained. Some authors have used the upward "jump" of the tracer particle during the PEPT measurements to derive the averaged bubble rise velocity. However this gives no information about the bubble size and bubble frequency during the experiments. Therefore, to measure bubble properties in a 3D-fluidized bed, dedicated tomography experiments should be performed, for example Electrical Capacitance Tomography (ECT) or X-ray tomography.

The hydrodynamic behavior of industrial scale bubbling fluidized bed

reactors was investigated using the Discrete Bubble Model. In the DBM, an Euler-Lagrange model, the effects of bubble-bubble interactions on the macro-scale velocity profiles were investigated. It was found that the extent of the macroscopic circulation and the average bubble diameter as function of the height in the fluidized bed is significantly increased by the bubble-bubble interaction forces. Using dedicated DIA experiments, the bubble-bubble interaction model can be further investigated and validated. When the DBM is extended to cylindrical geometrics, the DBM model can be further validated with the results obtained in the PEPT experiments described in chapter 4 of this thesis. An elegant way to simulate cylindrical fluidized beds with the DBM is via an immersed boundary technique, with which the advantages of using Cartesian grids to solve the Navier-Stokes equations can be preserved.

Nomenclature

Symbols

A_0	Catchment area	m^2
A_b	Bubble aspect ratio	-
AF	Wake acceleration factor	-
A_t	Cross-sectional area of bed	m^2
c'	Particle velocity after collision	$m.s^{-1}$
c	Interaction coefficient	-
C	Constant	-
	Fluctuating component of the particle velocity	$m.s^{-1}$
D	Distribution function	-
D_T	Diameter fluidized bed	m
d	Diameter	m
	Bubble span	m
E	Energy	J
e	Coefficient of restitution	-
F	Force	N
	Constant	$N.m^{-2}$
g	Gravitational acceleration	$m.s^{-2}$
$textrmg_0$	Radial distribution function	-
h	Height	m
I	Image intensity	-
	Unit tensor	-
	Moment of inertia	$kg.m^2$
k	Spring stiffness	$N.m^{-1}$
	Unit vector along the line of centers at collision	-

Symbols

M	Magnification	$m^2.px^{-2}$
m	Mass	kg
N	Number	-
n	Normal unit vector	-
	Width of distribution window	m
P	Pressure	Pa
p	Pressure	Pa
q_s	Pseudo-Fourier fluctuating kinetic energy flux	$kg.m^{-1}.s^1$
$\hat{R}$	Cross-covariance	-
R	Radius	m
r	Position	m
	Constant	-
S	Surface	m^2
	Source term	$kg.m^{-2}.s^{-2}$
S_b	Bubble surface in pseudo 2D bed	m^2
SF	Size factor	-
S_p	Displacement of the particles	m
s	Constant	-
T	Threshold	-
	Torque	$N.m$
t	Time	s
	Depth	m
	Tangential unit vector	-
U	Superficial gas velocity	$m.s^{-1}$
u	Continuum velocity	$m.s^{-1}$
	Bubble rise velocity	$m.s^{-1}$
u^*	Filtered velocity	$m.s^{-1}$
u_0	Superficial gas velocity	$m.s^{-1}$
V	Volume	m^3
v	Velocity	$m.s^{-1}$
v^*	Bubble rise velocity with wake acceleration	$m.s^{-1}$
W	Work	W
x	x-position	m
y	y-position	m
z	z-position	m

Greek symbols

α	Specularity coefficient	-
β	Inter-phase momentum transfer coefficient	$kg.m^{-3}.s^{-1}$
δ	Overlap	m
δ_b	Distance between two consecutive bubbles	m
ε	Porosity	-
ε^*	Averaged emulsion phase fraction	-
γ	Dissipation of granular energy due to inelastic particle-particle collisions	$kg.m^{-1}.s^{-3}$
η	Damping coefficient	$Ns.m^{-1}$
ϕ_I	Internal angle of friction	rad
ϕ_s	Sphericity	-
κ_s	Pseudo-thermal conductivity	$kg.m^{-1}.s^{-1}$
λ_s	Bulk viscosity	$Pa.s$
μ	Coefficient of friction	-
	Shear viscosity	$Pa.s$
ν_b	Observed bubble flow rate	$m^3.s^{-1}$
θ	Granular temperature	$kg.m^2.s^{-2}$
ρ	Density	$kg.m^{-3}$
σ_f	Deviation	-
τ	Stress tensor	Pa
ω	Angular velocity	$rad.s^{-1}$
ψ	Scale factor	-
	Visual bubble flow rate	-
	Constant	-

Subscripts

ab	indices of colliding particle pair
BB	bubble-bubble
b	bubble
bed	bed
c	critical
$cell$	computational cell
$conv$	convection
D	drag

Subscripts

df	dense phase
	energy dissipated by the friction between particles
dn	energy dissipated by the normal dashpot
drag	drag
dt	energy dissipated by the tangential dashpot
e	emulsion
eff	effective
f	image number
	frictional
G	gravitational
g	gas
gran	granular
kc	kinetic and collisional
kin	kinetic
mf	minimum fluidization
n	normal direction
	nozzles
P	pressure
pres	pressure
p	particle
pix	pixel
pot	potential
rest	restitution
rot	rotational
s	solid
sn	potential energy of the normal spring
sph	sphere
st	potential energy of the tangential spring
t	tangential direction
	total
VM	virtual mass
x	x-position
y	y-position
z	z-position

Bibliography

J.A. Almendros-Ibanez, C. Sobrino, S. Sanchez-Delgado, D. San ta na, M. de Vega, and U. Ruiz-Rivas. Through flow velocity crossing the dome of erupting bubbles in 2-D fluidized beds. In *Fluidization XII*, Vancouver, Canada, 2007.

T.B. Anderson and R. Jackson. Fluid mechanical description of fluidized beds. equations of motion. *Industrial & Engineering Chemistry Fundamentals*, 6(4):527–539, 1967.

P.K. Aragwal, A.S. Hull, and K.S. Lim. Digital Image Analysis analysis techniques for the study of bubbling fluidized beds. In J. Chaouki, F Larachi, and M.P. Dudukovic, editors, *Non-invasive monitoring of multiphase flows*, pages 407–454. Elsevier Science B.V., 1997.

T.R. Auton. *The dynamics of bubbles, drops and particles in motion in liquids*. PhD thesis, University of Cambridge, 1983.

J. Baeyens and D. Geldart. Solids mixing. In D. Geldart, editor, *Gas Fluidization Technology*, pages 97–122. John Wiley & Sons Ltd., 1986.

R.B. Bird, W.E. Stewart, and E.N. Lightfoot. In *Transport phenomena*, page 79. John Wiley & Sons Ltd., 1960.

G.A. Bokkers. *Multi-level modelling of the hydrodynamics in gas phase polymerisation reactors*. PhD thesis, University of Twente, 2005.

G.A. Bokkers, M. van Sint Annaland, and J.A.M. Kuipers. Mixing and segregation in a bidisperse gas-solid fluidised bed: a numerical and experimental study. *Powder Technology*, 140:176–186, 2004.

G.A. Bokkers, J.A. Laverman, M. van Sint Annaland, and J.A.M. Kuipers. Modelling of large-scale dense gas-solid bubbling fluidised beds using a novel discrete bubble model. *Chemical Engineering Science*, 61:5590–5602, 2006.

I.D. Burdett. Gas-phase fluidization technology for production of polyolefins. In *Fluidization X*, Beijing, People Republic of China, 2001.

R. Clift and J.R. Grace. Bubble interaction in fluidized beds. *Chemical engineering progress symposium series*, 105(66):14–27, 1970.

R. Clift and J.R. Grace. Coalescence of bubbles in fluidized beds. *AIChE symposium series*, 67(116):23–33, 1971.

R. Clift and J.R. Grace. Continuous bubbling and slugging. In J.F. Davidson adn R. Clift and D. Harrison, editors, *Fluidization*, pages 73–128. Academic Press, Inc, 2nd edition edition, 1985.

R. Collins. The effect of a containing cylindrical boundary on the velocity of a large gas bubble in a liquid. *Journal of Fluid Mechanics*, 28:97–112, 1967.

P.A. Cundall and O.D.L Strack. A discrete numerical model for granular assemblies. *Geotechnique*, 29:47–65, 1979.

D. Darmana, N. G. Deen, and J.A.M. Kuipers. Detailed modeling of hydrodynamics, mass transfer and chemical reactions in a bubble column using a discrete bubble model. *Chemical Engineering Science*, 60: 3383–3404, 2005.

N.G. Deen, M. van Sint Annaland, and J.A.M. Kuipers. Multi-scale modeling of dispersed gas-liquid two-phase flow. *Chemical Engineering Science*, 59:1853–1861, 2004.

W. Dijkhuizen, G.A. Bokkers, N.G. Deen, M. van Sint Annaland, and J.A.M. Kuipers. Extension of PIV for measuring granular temperature field in dense fluidized beds. *AIChE Journal*, 53(1):108–118, 2007.

G.R. Duursma, D.H. Glass, S. Rix, and M.I. Yorquez-Ramirez. PIV investigations of flow structures in the fluidised bed freeboard region. *Powder Technology*, 138:2–11, 2001.

X. Fan, D.J. Parker, and M.D. Smith. Enhancing ^{18}F uptake in a single particle for positron emission particle tracking through modification of solid surface chemistry. *Nuclear Instruments and Methods in Physics Research A*, 558:542–547, 2006a.

X. Fan, D.J. Parker, and M.D. Smith. Labelling a single particle for positron emission particle tracking using direct activation and ion-echange techniques. *Nuclear Instruments and Methods in Physics Research A*, 562:345–350, 2006b.

X. Fan, D.J. Parker, Z. Yang, J.P.K. Seville, and J. Baeyens. The effect of bed materials on the solid/bubble motion in a fluidised bed. *Chemical Engineering Science*, 63:943–950, 2008.

T. Farrokhalaee. *Gas distribution and bubble motion in fluidised beds*. PhD thesis, University of Cambridge, 1979.

D. Geldart. The size and frequency of bubbles in two- and three-dimensional gas-fluidised beds. *Powder Technology*, 4:41, 1970/71.

D. Geldart. Types of gas fluidization. *Powder Technology*, 7:285–292, 1973.

L.R. Glicksman. Scaling relationships for fluidized beds. *Chemical Engineering Science*, 39:1373–1379, 1984.

M.J.V. Goldschmidt. *Hydrodynamic Modelling of Fluidised Bed Spray Granulation*. PhD thesis, University of Twente, 2001.

M.J.V. Goldschmidt, J.A.M. Kuipers, and W.P.M. van Swaaij. Hydrodynamic modelling of dense gas-fluidised beds using the kinetic theory of granular flow: effect of coefficient of restitution on bed dynamics. *Chemical Engineering Science*, 56:571–578, 2001.

M.J.V. Goldschmidt, J.M. Link, S. Mellema, and J.A.M. Kuipers. Digital image analysis measurements of bed expansion and segregation dynamics in dense gas-fluidised beds. *Powder Technology*, 138:135–159, 2003.

M.J.V. Goldschmidt, R. Beetstra, and J.A.M. Kuipers. Hydrodynamic modelling of dense gas-fluidised beds: comparison and validation of 3d discrete and continuum models. *Powder Technology*, 142:23–47, 2004.

K. Hilligardt and J. Werther. Local bubble gas hold-up and expansion of gas/solid fluidized beds. *German Chemical Engineering*, 6:215, 1986.

B.P.B. Hoomans. *Granular dynamics of gas-solid two-phase flows*. PhD thesis, University of Twente, the Netherlands, 1999.

B.P.B. Hoomans, J.A.M. Kuipers, W.J. Briels, and W.P.M. van Swaaij. Discrete particle simulations of bubble and slug formation in two-dimensional gas-fluidised beds: a hard sphere approach. *Chemical Engineering Science*, 51:99–108, 1996.

B.P.B Hoomans, J.A.M. Kuipers, M.A. Mohd Salleh, M. Stein, and J.P.K. Seville. Experimental validation of granular dynamics simulations of gas-fluidised beds with homogenous in-flow conditions using Positron Emission Particle Tracking. *Powder Technology*, 116:166–177, 2001.

I. Hulme and A. Kantzas. Determination of bubble diameter and axial velocity for a polyethylene fluidized bed using x-ray fluoroscopy. *Powder Technology*, 147:20–33, 2004.

Y Igci, A.T. Andrews, S. Sundaresan, S. Pannala, and T. O'Brien. Filtered two-fluid models for fluidized gas-particle suspensions. *AIChE. Journal*, 54(6):1431–1447, 2008.

J.T. Jenkins and C. Zhang. Kinetic theory for identical, frictional, nearly elastic spheres. *Physics of Fluids*, 14:1228–1235, 2002.

P.C. Johnson and R. Jackson. Frictional-collisional constitutive relations for granular materials, with application to plane shearing. *Journal of Fluid Mechanics*, 176:67–93, 1987.

P.C. Johnson, P. Nott, and R. Jackson. Frictional-collisional equations of motion of particulate flows and their application to chutes. *Journal of Fluid Mechanics*, 210:501–535, 1990.

A.H. Kharaz, D.A. Gorham, and A.D. Salman. Accurate measurement of particle impact parameters. *Measurement Science and Technology*, 10:31–35, 1999.

Y.V. Kissin. Polymers of higher olefins. In *Kirk-Othmer Encyclopedia of Chemical Technology*. John Wiley and Sons, Inc, 2005.

R. Krishna and J.M. van Baten. Using CFD for scaling up gas-solid bubbling fluidised bed reactors with Geldart a powders. *Chemical Engineering Science*, 82:247–257, 2001.

J.A.M. Kuipers, K. J. van Duin, F.P.H. van Beckum, and W.P.M. van Swaaij. Computer simulation of the hydrodynamics of a two dimensional gas-fluidized bed. *Computational Chemical Engineering*, 17:839–858, 1993.

D. Kunii and O. Levenspiel. *Fluidization engineering*. Butterworth-Heinemann, 2nd edition, 1991.

C.N. Lim, M.A. Gilbertson, and A.J.L. Harrison. Bubble distribution and behavior in bubbling fluidised beds. *Chemical Engineering Science*, 62: 56–69, 2007.

K.S. Lim, P.K. Agarwal, and B.K. O'Niell. Measurement and modelling of bubble parameters in a two-dimensional gas-fluidized bed using image analysis. *Powder Technology*, 60:159–171, 1990.

H. Lindborg, M. Lysbert, and H.A. Jakobson. Practical validation of the two-fluid model applied to dense gas-solid flows in fluidized beds. *Chemical Engineering Science*, 62:5854–5869, 2007.

J. Link, C. Zeilstra, N.G. Deen, and J.A.M. Kuipers. Validation of a Discrete Particle Model in a 2D spout-fluid bed using non-intrusive optical measuring techniques. *The Canadian Journal of Chemical Engineering*, 82:30–36, 2004.

B. Liu, X Zhang, L. Wang, and H. Hong. Fluidization of non-spherical particles: Sphericity, zingg factor and other fluidization parameters. *Particuology*, 6:125–129, 2008.

H. Lu, S. Wang, Y. Zhao, L. Yang, D. Gidaspow, and J. Ding. Prediction of particle motion in a two-dimensional bubbling fluidized bed using discrete hard-sphere model. *Chemical Engineering Science*, 60:3217–3231, 2005.

D. Moslemian, N. Devanthan, and M.P. Dudukovic. Radioactive particle tracking technique for investigation of phase recirculation and turbulence in multiphase systems. *Review of Scientific Instruments*, 63(10): 4361–4372, 1992.

N. Mostoufi and J. Chaouki. Local solid mixing in gas-solid fluidized beds. *Powder Technology*, 114:23–31, 2001.

N. Mostoufi and J. Chaouki. Flow structure of the solids in gas-solid fluidized beds. *Chemical Engineering Science*, 59:4217–4227, 2004.

R.F. Mudde, H.B.M. Schulte, and H.E.A. van den Akker. Analysis of a bubbling 2-D gas-fluidized bed using image processing. *Powder Technology*, 81:149–159, 1994.

C.R. Muller, J.F. Davidson, J.S. Dennis, and A.N. Hayhurst. A study of the motion and eruption of a bubble at the surface of a two-dimensional fluidized bed using particle image velocimetry (PIV). *Industrial & Engineering Chemistry Research*, 46(5):1642–1652, 2007.

J.J. Nieuwland, M. van Sint Annaland, J.A.M. Kuipers, and W.P.M. van Swaaij. Hydrodynamic modeling of gas/particle flow in riser reactors. *AIChE Journal*, 42:1569–1582, 1996.

F. Odar and W.S. Hamilton. Forces on a sphere accelerating in a viscous liquid. *Journal of Fluid Mechanics*, 18:302–314, 1964.

D. Pallares, F. Johnsson, and B. Leckner. A novel technique for particle tracking in cold 2-dimensional fluidised beds- simulating fuel dispersion. *Chemical Engineering Science*, 61:2710–2720, 2006.

S. Pannala, C.S. Daw, and J.S. Halow. Simulations of reacting fluidized beds using an agent-based bubble model. *International Journal of Chemical Reactor Engineering*, 1(A20):1–18, 2003.

S. Pannala, C.S. Daw, and J.S. Halow. Dynamic interacting bubble simulation (DIBS): An agent-based bubble model for reacting fluidized beds. *Chaos*, 14(2):487–498, 2004.

D.J. Parker, C.J. Broadbent, P. Fowles, M.R. Hawkesworth, and P.A. McNeil. Positron emission particle tracking - a technique for studying flow within engineering equipment. *Nuclear Instruments and Methods in Physics Research A*, 326:592–607, 1993.

D.J. Parker, D.A. Allen, D.M. Benton, P. Fowles, P.A. McNiel, Min Tan, and T.D. Beynon. Developments in particle tracking using the Birmingham POSITRON CAMERA. *Nuclear Instruments and Methods in Physics Research A*, 392:421–426, 1997.

D.J. Parker, R.N. Forster, P. Fowles, and P.S. Takhar. Positron emission particle tracking using the new Birmingham positron camera. *Nuclear Instruments and Methods in Physics Research A*, 477:540–545, 2002.

J.A. Pita and S. Sundaresan. Gas solid flow in vertical tubes. *AIChE Journal*, 37(7):1009–1018, 1991.

S.B. Savage. Analyses of slow high-concentration flows of granular materials. *Journal of Fluid Mechanics*, 377:1–26, 1998.

L. Shen, F. Johnsson, and B. Leckner. Digital image analysis of hydrodynamics two-dimensional bubbling fluidized beds. *Chemical Engineering Science*, 48:2607–2617, 2004.

J.L. Sinclair and R. Jackson. Gas-particle flow in a vetical pipe with particle-particle interactions. *AIChE Journal*, 129:72–85, 1989.

A. Srivastava and S. Sundaresan. Analysis of a frictional-kinetic model for gas-particle flow. *Powder Technology*, 129:72–85, 2003.

M. Stein, Y.L. Ding, J.P.K. Seville, and D.J. Parker. Solids motion in bubbling gas fluidized beds. *Chemical Engineering Science*, 55:5291–5300, 2000.

M. Stein, Y.L. Ding, J.P.K. Seville, and D.J. Parker. Experimental verification of the scaling relationships for bubbling gas-fluidised beds using PEPT technique. *Chemical Engineering Science*, 57:3649–3658, 2002.

F. Taghipour, N. Ellis, and C. Wong. Experimental and computational study of gas-solid fluidized bed hydrodynamics. *Chemical Engineering Science*, 60:6857–6867, 2005.

R.P. Utikar and V.V. Randade. Single jet fluidized beds: experiments and CFD simulations with glass and polypropylene particles. *Chemical Engineering Science*, 62:167–183, 2007.

M.S. van Buijtenen, M. Boerner, N.G. Deen, S. Heinrich, S. Antonyuk, and J.A.M. Kuipers. An experimental study of the effect of collision properties on spout fluidized bed dynamics. In *9th International Symposium on Agglomeration*, Sheffield, United Kingdom, 2009.

M.A. van der Hoef, R. Beetstra, and J.A.M. Kuipers. Lattice boltzmann simulations of low-reynolds-number flow past mono- and bidisperse arrays of spheres: results for the permeability and drag force. *Journal of Fluid Mechanics*, 528:233–254, 2005.

M.A. van der Hoef, M. Ye, M. van Sint Annaland, A.T. Andrews, S. Sundaresan, and J.A.M. Kuipers. Multi-scale modeling of gas-fluidized beds. *Adv. Chem. Eng.*, 31:65–149, 2006.

J. Werther. Effect of gas distributor on the hydrodynamics of gas fluidized beds. *German Chemical Engineering*, 1:166, 1978.

J. Westerweel. Fundamentals of digital particle image velocimetry. *Measurement Science and Technology*, 8:1379–1392, 1997.

K.S. Whiteley, T.G. Heggs, R. L. Mawer H. Koch, and W. Immel. Polyolefins. In D. Geldart, editor, *Ullmann's Encyclopedia of Industrial Chemistry*. John Wiley & Sons Ltd., 2000.

W-C Yang. Modification and re-interpretation of Geldart's classification of powders. *Powder Technology*, 171:69–74, 2007.

List of Publications

1. Deshmukh, S.A.R.K., Laverman, J.A., Van Sint Annaland, M. and Kuipers, J.A.M. (2005). 'Development of a Membrane-Assisted Fluidized Bed Reactor. 1. Gas Phase Back-Mixing and Bubble-to-Emulsion Phase Mass Transfer Using Tracer Injection and Ultrasound Experiments', Ind. Eng. Chem. Res.; 2005; 44(16); 5955-5965.

2. Deshmukh, S.A.R.K., Laverman, J.A., Van Sint Annaland, M. and Kuipers, J.A.M. (2005). 'Development of a Membrane-Assisted Fluidized Bed Reactor. 2. Experimental Demonstration and Modeling for the Partial Oxidation of Methanol', Ind. Eng. Chem. Res.; 2005; 44(16); 5966-5976.

3. G.A. Bokkers, J.A. Laverman, M. van Sint Annaland and J.A.M. Kuipers (2006). 'Modelling of large-scale dense gas-solid bubbling fluidised beds using a novel Discrete Bubble Model', Chemical Engineering Science, Volume 61, Issue 17, September 2006, Pages 5590-5602.

4. J.A. Laverman, M. van Sint Annaland and J.A.M. Kuipers (2006).'Hydrodynamics of bubbling gas-solid fluidised beds using the discrete bubble model', 19th International Symposium on Chemical Reaction Engineering, September 3-6, 2006, Potsdam,Germany.

5. J.A. Laverman, M. van Sint Annaland and J.A.M. Kuipers (2006). 'Hydrodynamics of Bubbling Gas-Solid Fluidised Beds using the

Discrete Bubble Model', Fifth International Conference On Computational Fluid Dynamics in the Process Industries, 13-15 December 2006, Hilton on the Park, Melbourne, Australia.

6. J.A. Laverman, M. van Sint Annaland and J.A.M. Kuipers (2007). 'Influence of Bubble-Bubble interactions on the macroscale circulation patterns in a bubbling gas-solid fluidized bed', The 12th International Conference on Fluidization, May 13-17, 2007, Vancouver, Canada.

7. J.A. Laverman, M. van Sint Annaland and J.A.M. Kuipers (2007). 'Experimental study on solids mixing and bubble behavior in a pseudo-2D, freely bubbling, gas-solid fluidized bed using PIV and DIA', 6th International Conference on Multiphase Flow, ICMF 2007, July 9 - 13, 2007, paper no. 307, Leipzig, Germany.

8. J.A. Laverman, I. Roghair, M. van Sint Annaland and J.A.M. Kuipers (2008). 'Experimental Study on Solids Circulation Patterns and Bubble Behavior Using Particle Image Velocimetry Combined with Digital Image Analysis', 6th International Conference on Computational Fluid Dynamics in the Oil & Gas, Metallurgical and Process Industries Trondheim, Norway 10-12 June 2008

9. J.A. Laverman, I. Roghair, M. van Sint Annaland and J.A.M. Kuipers (2008). 'Investigation into the hydrodynamics of gas-solid fluidized beds using particle image velocimetry coupled with digital image analysis', Canadian Journal of Chemical Engineering, Volume 86, Issue 3, June 2008, Pages 523-535.

10. J.A. Laverman, M. van Sint Annaland and J.A.M. Kuipers (2008). 'Macroscopic circulation patterns in gas-solid bubbling fluidized beds', International Conference on the Reaction Engineering of Polyolefins, Montreal, Canada, 22-27 June 2008.

Levensloop

Jan Albert Laverman is op 13 juli 1976 geboren te Beetgum. In Beetgumermolen heeft hij de lagere school "Mooitaki" doorlopen. Vervolgens is naar "de Ulbe van Houten" gegaan waar hij de M.A.V.O. heeft gevolgt. Daarna is hij naar de "Friesland College" M.L.O. gegaan waar hij de Analytische Chemie afdeling heeft doorlopen. Toen is hij naar de "Noordelijke Hogeschool Leeuwarden" gegaan waar hij de richtingen Chemische Technologie en Technische Bedrijfskunde heeft gedaan. Tussen de Chemische Technologie en Technische Bedrijfskunde heeft hij nog een half jaar gewerkt bij DSM-StamiCarbon op de afdeling Technology.

In september 2001 is hij begonnen met de verkorte opleiding Chemische Technologie aan de Universiteit Twente. In april 2004 is hij afgestudeerd binnen de toenmalige werkeenheid Fundamentele Aspecten van de Proceskunde (FAP) op het onderwerp "Partial oxidation of methanol in a membrane assisted fluidized bed reactor".

In juni 2004 trad hij in dienst van de werkeenheid FAP om als promovendus een onderzoek te verrichten op het gebied van hydrodynamica in meer fasen reactoren. De resultaten van dit onderzoek staan beschreven in dit proefschrift.

Sinds april 2009 is hij in dienst bij N.V. Nederlandse Gasunie te Groningen.

Dankwoord

Aan alle goede dingen komt een einde, zo ook mijn promotieonderzoek. Hoewel er maar één naam op dit boekje staat, hebben vele mensen een bijdrage aan mijn promotieonderzoek geleverd. Via dit dankwoord wil ik deze mensen dan ook bedanken.

Allereerst gaat mijn dank uit naar mijn twee promotoren, Hans Kuipers en Martin van Sint Annaland. Hans, als eerste wil ik je bedanken voor de mogelijkheid om in jouw groep mijn promotie te doen. Ondanks je drukke dubbelfunctie als wetenschappelijk directeur van IMPACT en hoogleraar van de vakgroep had je altijd tijd voor de maandelijkse besprekingen. In deze besprekingen werden alle aspecten van mijn project besproken en kon je de grote lijnen van mijn onderzoek bewaken. Je nam de juiste beslissingen op de kritische momenten tijdens mijn promotie. Martin, onze samenwerking heb ik altijd erg op prijs gesteld. Het was altijd plezierig met jou over vakinhoudelijke aspecten te discusseren. Jouw aanstekelijke enthousiasme en kritische houding hebben er voor gezorgd dat mijn onderzoek naar een hoger niveau werd getild. De correcties van mijn artikelen en hoofdstukken worden zeer gewaardeerd, dankzij jou heb ik geen artikel over papegaaien gepubliceerd.

Tijdens mijn promotieonderzoek heb ik het voorrecht gehad om een paar studenten te begeleiden. Jeroen Stroomer heeft een literatuuronderzoek uitgevoerd naar de macroscopische circulatiepatronen in een gas-vast wervelbed. Naast Jeroen heb ik twee afstudeerstudenten mogen begeleiden, Ivo -fluidized beds are sexy- Roghair en Marc ten Bulte. Ivo Roghair's bijdrage aan het DIA algoritme en de nieuwe meettech-

niek waar PIV met DIA gecombineerd werd, waren essentieel voor de ontwikkeling van de nieuwe meetmethode. Marc ten Bulte heeft met zijn uiterst nauwkeurige manier van werken en zijn vastberadenheid de lastige experimenten met LLDPE deeltjes tot een uitstekend einde weten te brengen.

I am grateful to professor Johnathan Seville and professor David Parker for offering me the opportunity to perform the Positron Emission Particle Tracking experiments at the University of Birmingham. Also their hospitality and support during the experiments, described in chapter 4 are appreciated greatly. Furthermore, I would like to thank dr. Fan for activating the tracer particles and for his help during the experiments and also I am grateful to dr. Ingram for the stimulating discussions during the experiments.

Dit project is gefinancieerd door het Dutch Polymer Institute (DPI). De sponsormeetings van het DPI in Amsterdam en Sorrento waren erg leerzaam. Vooral de interactie tussen de promovendi en industrie waren erg motiverend. Een speciaal woord van dank gaat uit naar Gerben Meier, Jochem Pater en Michiel Bergstra voor hun interesse en feedback tijdens mijn onderzoek.

Het experimentele deel van dit proefstuk is mede mogelijk gemaakt door de uitstekende technische ondersteuning van de technici binnen de vakgroep. Als eerste wil Gerrit Schorfhaar bedanken voor het onderhouden en optimaliseren van het pseudo 2D ervelbed. Wim Leppink en Robert Meijer bedankt voor het bouwen van het wervelbed voor de Positron Emission Particle Tracking experimenten. Daarnaast wil ik Wim eveneens bedanken voor zijn technische ondersteuning in Engeland. Daarom nog eenmaal, Wim ... succes! Nicole Haitjema wil ik graag bedanken voor de perfecte administratieve ondersteuning, dankzij jou liep alles op rolletjes.

Het numerieke deel van dit proefstuk is alleen mogelijk met goed werkende rekenclusters. Dit was binnen de vakgroep perfect geregeld dankzij de tomeloze inzet van Robert Brouwer, Dadan Darmana, Christiaan Zeilstra, Wouter Dijkhuizen, Willem Godlieb, Sebastian Kriebitzsch, Ivo Roghair en Tom Kolkman. Daarom wil ik jullie bedanken voor het

bouwen en onderhouden van alle clusters.

De ruim 4,5 jaar die ik binnen de vakgroep heb mogen doorbrengen waren altijd erg plezierig. Dit kwam voornamelijk door de fijne collega's op de kantoortuin en de vele borrels en lezingen. Een speciaal woord van dank gaat dan ook uit naar Renske Beetstra, Sander Noorman plv., Sebastian Kriebitzsch en Jelle de Jong voor het verzorgen van de borrels en eveneens naar Joris Smit, Tymen Tiemersma en Martin Tuinier voor het organiseren van de "Vlugterlectures" waar alle promovendi hun werk konden presenteren en eventuele problemen die ze tijdens hun werk tegenkwamen aan een breed publiek konden voorleggen. Eveneens wil ik Liesbeth Kuipers bedanken voor de organiseren van de jaarlijkse "Waarbeek" uitjes.

Ik wil hier tevens mijn dank alvast uitspreken aan mijn paranimfen, Sebastian Kriebitzsch en Ivo Roghair voor het helpen met de laatste voorbereidingen voor mijn promotie. Daarnaast zullen ze me bijstaan tijdens mijn verdediging en de festiviteiten nadien.

Eveneens wil ik hier mijn ouders bedanken voor hun steun tijdens de promotie. Jullie hebben het voor mij mogelijk gemaakt dat ik me tijdens mijn studie volledig kon richten op studeren. Jacob, Wybe en de familie Klaassen, jullie steun en interresse in mijn promotie heeft altijd een motiverende werking op mij gehad. Ten slotte wil ik Anouk bedanken voor haar steun en geduld tijdens het schrijven van dit proefschrift. Het heeft allemaal iets langer heeft geduurd dan vooraf gedacht, maar vanaf nu kunnen we samen leuke dingen doen.

Hartelijk bedankt!

Jan Albert